A new model for obtaining the flux position in a slip-ring induction machine

Nillesen, M.E.

Award date:
1997

Faculteit der Elektrotechniek
Vakgroep Meet- en Besturingssystemen
Sectie Elektromechanica en Vermogenselektronica

Afstudeerverslag

A NEW MODEL FOR OBTAINING THE FLUX POSITION IN A SLIP-RING INDUCTION MACHINE.

MBS-EMV 97-10 M.E.Nillesen

Hoogleraar : Prof.dr.ir. A.J.A. Vandenput

Mentor(en) : Dr.-Ing. F. Blaschke

Eindhoven,

PREFACE

Since childhood I have been affected with the challenging aspects of electrical engineering. After my secondary school I attended classes at the technical faculty of the *"Hogeschool Gelderland"*. Before this education I had a personal interest in the field of analog electronics, however, after two years of education I became more and more interested in the field of electric drives. After my specialisation in power engineering I decided to get my master degree at the *"Eindhoven University of Technology"*.

In spite of the different approach of electrical engineering at a university, I knew from the beginning that I would specialize myself in the multi-disciplinary field of electric drives. About two years ago I got in touch with prof. Vandenput, the chairman of the section *"Electromechanics and Power Electronics"* at our university. I revealed my personal interests and asked him for a graduation subject in the field of electric drives.

Also thanks to my clear and timely request, prof. Vandenput was able to arrange a graduation subject, concerning a high standing research in cooperation with Dr. Blaschke. I was and still am very honoured with this cooperation, because Dr. Blaschke is a respected person in the field of electric drives.

During his presence at our section I had often interesting discussions with Dr. Blaschke. He taught me how to execute a scientific analysis. His scientific analysis with the help of analog electronics won't slip my mind. Once we had a discussion about the simulation of the machine structure in real-time. I told him, that sometimes it is not so easy to perform a simulation in real-time on a DSP-system. His comment was simple, but powerful: *"Die Maschine kann es, dann soll der viel schnellere Rechner das doch auch können*[1]". In other words, he underlined the strength of analog electronics.

At the beginning of my task I learned a lot from S. Bosga, who was finishing his work for getting his Ph. D.-degree in the field of electric drives. Especially his knowledge about the DSP-system helped me a lot. Later on I tried to disturb him as little as possible, since he was mainly occupied with finishing his thesis. In the meantime he got his Ph. D.-title.

I would like to thank the above mentioned people for their contribution and interest during my graduation. During the absence of Dr. Blaschke and Dr. Bosga, prof. Vandenput was responsible for my graduation (during this period I also asked some support from Dr. Duarte). Prof. Vandenput corrected this final report and also for that I owe him thanks. Finally I would like to thank all the people from the section *"Electromechanics and Power Electronics"*, for their professional contribution, but certainly also for the pleasant work-environment.

Martijn Nillesen

[1]Translation: *"The machine can do it, then the much faster computer has to do it also."*

SUMMARY

A NEW MODEL FOR OBTAINING THE FLUX POSITION IN A SLIP-RING INDUCTION MACHINE.

In the beginning the DC-machine was most popular in the field of electric drives, since the control of this machine with a high performance was very easy. Because the DC-machine is equipped with a commutator, which requires a lot of maintenance, the industry was very interested in control techniques for induction machines. Thanks to developments in the seventies (Field Oriented Control) and in the eighties (Direct Self Control), nowadays the induction machine is applied widely in the field of high performance drives, since its robust construction takes care for low costs and low maintenance.

For Field Oriented Control it is essential to know the position of the magnetic flux. With the help of the U/I-model the flux position can be estimated from the stator voltages and currents. Its performance is outstanding at frequencies above 5 Hz, however beneath 5 Hz the performance decreases and it is even not capable to estimate the flux at standstill. Therefore, further research in the field of electric drives is mainly focussed on the region around frequency zero. Thanks to an invention of Dr. Blaschke within the section "*Electromechanics and Power Electronics*" of Eindhoven University of Technology, a solution is within one's reach.

The purely scientific research within the framework of this invention revealed that a reference model is needed, which estimates the flux position as accurately as possible in the whole frequency range. Therefore a new flux observer, the so-called model C, has been derived in which the magnetizing current is estimated from the stator and the rotor current. This indicates once again the purely scientific character of this model, since the rotor current can only be measured in a slip-ring induction machine. For this new model a lot of machine parameters have to be identified; therefore Dr. Blaschke derived some identification procedures. The first aim of this research was to simulate these techniques.

In order to simulate these techniques in real-time on a multi-DSP-system a machine structure affected with main-flux saturation is needed, because the identification techniques make use of the saturation effect. The already available linear machine structure of the induction machine is extended with main-flux saturation. First the consequences of applying a linear Field Oriented Control to the (non-linear) machine structure have been analysed: in the saturated region deviations in the torque and flux level will occur. After that a non-linear Field Oriented Control with a compensation for the saturation effect has been applied: no deviations occur. Next model C is appropriately connected to the machine structure and the identification techniques are simulated. The simulation results give information about the importance of some identified parameters, because an error can have disastrous effects in the next identification(s).

The simulations are verified on a 30 kW slip-ring induction machine supplied by a current hysteresis control. The early experiments show that iron losses can not be ignored: that is why introducing a variant of model C. This model estimates the rotor flux position with a high accuracy in the whole frequency range in steady state. Nevertheless, for the application as a reference model in a purely scientific research this will satisfy.

The real-time simulation of the identification techniques applied to the saturable machine structure provides a lot of realistic information. Further, the steady-state model takes care for a high accuracy in the whole frequency range as well as in the saturated region.

SAMENVATTING

EEN NIEUW MODEL VOOR FLUX BEPALING IN EEN ASYNCHRONE MACHINE MET SLEEPRINGEN.

In het begin van de elektrische aandrijftechniek werd de gelijkstroommachine vaak toegepast, omdat de realisatie van een hoogwaardige aandrijving daarmee relatief eenvoudig is. Echter een gelijkstroommachine is uitgerust met een commutator, die veel onderhoud vergt en daarom is de industrie erg geïnteresseerd in regeltechnieken voor draaiveldmachines. Dankzij ontwikkelingen in de jaren zeventig (Field Oriented Control) en tachtig (Direct Self Control) wordt de inductiemachine veelvuldig toegepast in hoogwaardige aandrijvingen, omdat haar robuuste constructie zorgt voor lage kosten en onderhoud.

Voor het kunnen toepassen van een veldgeoriënteerde regeling dient de positie van de magnetische flux bekend te zijn. Met behulp van het U/I model wordt deze bepaald vanuit de statorspanningen en -stromen. De nauwkeurigheid is uitstekend voor frequenties boven 5 Hz, echter beneden 5 Hz neemt de nauwkeurigheid af en het is helemaal niet in staat de flux te bepalen in stilstand. Daarom richt verder onderzoek in de elektrische aandrijftechniek zich vooral op het gebied rondom frequentie nul. Dankzij een uitvinding van Dr. Blaschke binnen de sectie "*Elektromechanica en Vermogenselektronica*" van de Technische Universiteit Eindhoven is een oplossing binnen handbereik.

Het zuiver wetenschappelijk onderzoek in het kader van deze uitvinding maakte duidelijk dat een referentiemodel nodig is, dat de fluxpositie bepaalt in het hele frequentiegebied met hoge nauwkeurigheid. Daarom is een nieuw flux-model, het zogenoemde model C, afgeleid waarin de magnetiseringsstroom wordt bepaald vanuit de stator- en rotorstromen. Dit toont nogmaals het zuiver wetenschappelijke karakter van dit model, omdat de rotorstromen alleen gemeten kunnen worden in een asynchrone machine met sleepringen. Een aantal machineparameters zal geïdentificeerd moeten worden; daarom heeft Dr. Blaschke identificatieprocedures afgeleid. Het eerste doel van dit onderzoek bestond uit het simuleren van deze identificatietechnieken.

Teneinde deze technieken te kunnen simuleren in real-time op een DSP-systeem, is een machinestructuur beïnvloed met verzadiging noodzakelijk, omdat de identificatietechnieken juist gebruik maken van de verzadiging. De al aanwezige lineaire machinestructuur is uitgebreid met verzadiging. Eerst zijn de gevolgen van de toepassing van een lineair veldgeoriënteerde regeling op de (niet-lineaire) machinestructuur geanalyseerd: in het verzadigde gebied zijn afwijkingen in koppel en flux waargenomen. Daarna is een niet-lineaire regeling toegepast, waarin geen afwijkingen zijn waargenomen. Vervolgens is model C aangesloten op de machinestructuur en zijn de identificatietechnieken gesimuleerd. De simulatie geeft inzicht op het belang van sommige geïdentificeerde parameters, omdat een kleine fout rampzalige gevolgen in de volgende identificaties kan veroorzaken.

De simulaties zijn geverifieerd op een 30 kW inductiemachine met sleepringen gevoed door een hysterese stroomregeling. De tests in het laboratorium toonden aan, dat ijzerverliezen niet meer verwaarloosd mogen worden: daarom wordt er een variant van model C geïntroduceerd. Dit model bepaalt de fluxpositie met een hoge nauwkeurigheid in het hele frequentiegebied in stationaire toestand. Niettemin zal dit voor de toepassing als referentiemodel in een zuiver wetenschappelijk onderzoek voldoen.

De real-time simulatie van de identificatietechnieken verschaft veel realistische informatie. Verder zorgt het stationaire model voor een hoge nauwkeurigheid in het hele frequentiegebied, ook tijdens verzadiging.

TABLE OF CONTENTS

CHAPTER 1

INTRODUCTION

1.1 Introduction.

In the beginning of AC-machine theory, see for instance Stanley[28], (transient) machine structure (model) descriptions were mainly used for better understanding of the machine's behaviour. In spite of the availability of these rather complete descriptions, it lasted till the seventies before these descriptions were fully used for controlling AC-machines (see Blaschke[3]: Field Oriented Control).

An explanation for the late application of the machine theory to the machine control is not available. One of the reasons could be that the researchers observed the machines only with their electromechanical background in those days. Dr. F. Blaschke, who is the great initiator of Field Oriented Control, was mainly occupied with control techniques. Thanks to his different background he observed the induction machine from the point of view of "*control*".

This new approach yielded the application of Field Oriented Control. This meant a turning-point in the field of electric drives: the DC-machine, very popular in drive systems at that time, had to compete with the induction machine. The induction machine is characterized with a very simple mechanical construction in comparison with a DC-machine. Therefore, the purchase and the maintenance of an induction machine are very favourable. However a disadvantage of the induction machine is that the control techniques have become more complicated.

Before one can apply Field Oriented Control, the position of the flux vector has to be known. There are different methods for obtaining the flux vector: the U/I-model is most popular. This model directly estimates the flux vector from the stator voltages and currents. The performance of this model is excellent at high frequencies, however, at low frequencies it will decrease and at frequency zero the model is even not capable of functioning. Thanks to an invention within our section, see Blaschke[5], the flux position can be estimated in the whole frequency range by means of a slightly adapted U/I-model.

This invention is also the motivation of this research. In order to experimentally verify the (scientific content of the) invention we will need a reference model which estimates the flux position with a high accuracy in the whole frequency range. This new reference model directly estimates the flux from the stator and the rotor current and the rotor position, and therefore it is only applicable to a slip-ring induction machine.

As usual during a scientific analysis we will first simulate this model before applying it in practice. For the simulation of this new flux observer we will need a machine structure affected with saturation, because this will approach the reality better. Such a machine structure is given by Blaschke[7].

Blaschke[7] also shows the influence of the saturation during Field Oriented Control. Further, he describes a new non-linear Field Oriented Control, which takes the saturation effect into account. The effects due to saturation during (linear) Field Oriented Control are also presented by Lorenz[20] and Vas[33]. However, they do not derive a compensation for the saturation effect in the control scheme.

Blaschke[8] describes the new flux observer, which we will use as reference model for further research on the invention mentioned above. The main topic of this report deals with parameter identification techniques for this model. These techniques allow us to estimate the inductances in every operating-point (except no-load). In literature no articles have been found which describe identification techniques estimating the leakage inductance of the stator and the rotor separately. Only Schierling[24] presents some techniques, which identify the necessary parameters for the machine control at startup. However, it is not possible to identify the separate leakage inductances with the help of these techniques. It is known, that the leakage inductances can not be considered constant during saturation. Lipo[19] extensively describes the types of fluxes which are responsible for leakage and since most of these fluxes flow through the machine iron, these fluxes will be influenced during saturation. Keyhani[16] and Lipo[19] simulate machine structures influenced with saturable (leakage) inductances; however, how they obtained the courses of these inductances during saturation is not clearly explained.

This research is based on the structures and techniques presented in Blaschke[7,8]. Preliminary simulations of the identification techniques already showed some possible troubles. This resulted in a new report (Blaschke[9]), which can be considered as an improvement and an extension of Blaschke[8].

This report contains the description and the execution of the analyses, presented in Blaschke[7,8,9]. Only the necessary information of the above mentioned reports is treated. New elements in this report are the descriptions of the used practical techniques and of course the experimental results.

1.2 Assumptions.

As usual during simulation of a physical process we have to make assumptions, because these processes are influenced by the environment. Further, to minimize the complexity of the analytical description of the process, it is also wise to make some assumptions. We hold the view, that it is allowed to make assumptions as long as one is aware of the restrictions of the final simulation and experimental results. For clearness the assumptions are listed below:

- The stator contains several identical sinusoidal windings, which are symmetrically placed along the air gap. The same situation is valid for the rotor, however a winding ratio between the stator and the rotor is present.

- We assume a smooth surface of the rotor and the stator, in other words the air-gap distance can be considered constant. Further, the air-gap width is small in comparison with the total axial length and the bore of the stator; consequently, the air-gap flux will radially cross the air gap.

- Saturation effect of the main flux path is taken into account, but the leakage flux is assumed to be not influenced by saturation. Iron losses, such as hysteresis and eddy currents are neglected.

- Resistance is considered to be time-independent, i.e. temperature-independent.

- During the simulation we considered the inverter as ideal, i.e. no occurrence of high harmonics. In practice we will neglect the presence of high harmonics due to the inverter and the non-sinusoidal distribution of the stator winding along the air gap, in other words we only consider the presence of the fundamental components of voltages and currents.

CHAPTER 2

A NEW MACHINE STRUCTURE FOR THE SATURATED INDUCTION MACHINE

2.1 Introduction.

In the early days of field oriented control, see Blaschke [2], a machine structure was used, which didn't describe the saturation effect. Consequently the field oriented control didn't take the saturation effect into account. The last few years articles arise about methods implementing the saturation effect in the machine structure of the induction machine and in the field oriented control. In most of the articles new techniques are presented which approach the saturation effect of the main flux with the help of transient models (for instance, see Healey[13], Sumner[30] etc.). These models adapt the parameters of the model during operation. A disadvantage of this method is the need for highly sophisticated digital signal processor(s). This chapter can be seen as a novel approach of the saturation effect in the induction machine, without using the method of the transient models.

First of all we will describe the main flux saturation with the help of a simple mathematical description. With this description we are able to derive a new machine structure which does describe the saturation effect. This new structure is based on the machine structure influenced with leakage flux, presented in Blaschke[4]. When we have a machine structure, we are able to derive a new field oriented control. This field oriented control takes into account the saturation effect.

2.2 Theoretical approach of the induction machine affected with main flux saturation.

The aim of this section is to create a simple, practical description of the saturation effect. Our consideration of the saturation effect is basically based on the equations of the machine model, presented in Blaschke[4] (chapter 9). For clearness these equations are shown in figure 2.1. After that the saturation effect has to be implemented in the machine structure which isn't affected with saturation. The machine will be supplied with a current source, so the description of the machine structure is more simplified than that of a machine supplied with a voltage source.

Supplying a machine with a current, the stator equation can be considered as linear. The constant current will create a specific stator flux. However supplying a machine with a voltage, the stator current and thus the stator flux will depend on a first order lag (formed by the stator resistance and inductance). So that will imply a higher order and a more complicated machine structure.

$$0 = r_k.\mathbf{i}_k^r + \dot{\psi}_k^r \qquad (9.4)$$

$$\psi_k^a = \psi_\ell^a + \ell_{\sigma k}.\mathbf{i}_k^a \qquad (9.5)$$

$$\psi_\ell^a = \ell.\mathbf{i}_{\mu\ell}^a \qquad (9.6)$$

$$\mathbf{i}_{\mu\ell}^a = \mathbf{i}_s^a + \mathbf{i}_k^a \qquad (9.7)$$

$$m_{el} = \left[R(\tfrac{\pi}{2}).\psi_\ell^a\right]^T.\mathbf{i}_s^a \qquad (9.8)$$

$$\dot{\rho}^s = \tfrac{1}{\theta}\int (m_{el} - m_{load}).dt \qquad (9.9)$$

$$\rho^s = \int \dot{\rho}^s.dt \qquad (9.10)$$

Figure 2.1: The equations of the current supplied induction machine influenced with leakage flux, presented in Blaschke[4] (chapter 9).

2.2.1. The mathematical description of the saturation effect.

To describe the saturation effect, we have to reconsider equation 9.6, the magnetizing equation:

$$\psi_\ell^a = \ell.\mathbf{i}_{\mu\ell}^a \qquad (2.1)$$

This equation shows, that ψ_ℓ and $\mathbf{i}_{\mu\ell}$, the vector of the air-gap magnetic flux and the vector of its generating magnetizing current, are both parallel oriented and related to each other with a constant factor of ℓ, see figure 2.2.

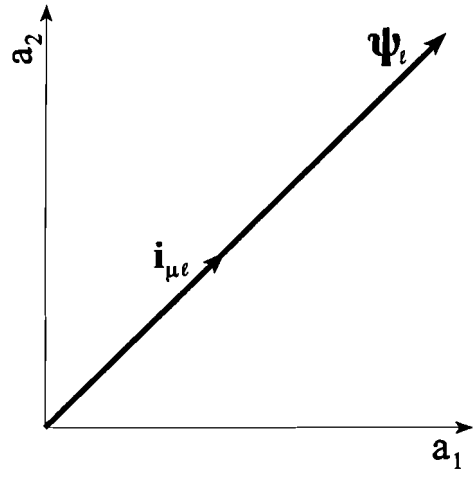

Figure 2.2: The relation between the vectors ψ_ℓ and $\mathbf{i}_{\mu\ell}$.

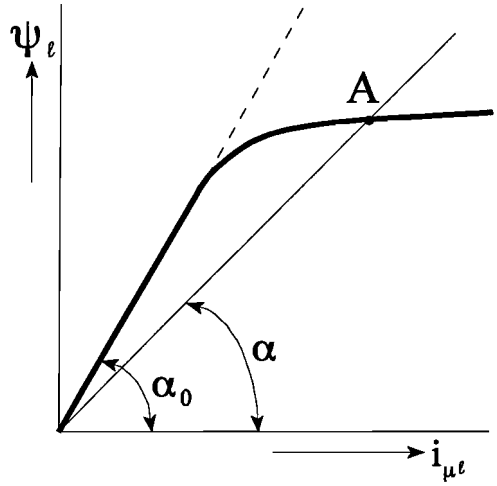

Figure 2.3: The relation between the length of the vectors ψ_ℓ and $\mathbf{i}_{\mu\ell}$ in the linear as well as the saturated range.

The angles of both vectors are the same, so the lengths of the vectors are related to each other with a scalar value:

$$\psi_\ell = \ell . i_{\mu\ell} \tag{2.2}$$

The value ℓ was kept constant in former considerations, but during saturation the relation between ψ_ℓ and $i_{\mu\ell}$ isn't linear anymore. In the linear situation we will change the value ℓ into ℓ_0 and its related angle into α_0 :

$$\ell_0 = \tan\alpha_0 \tag{2.3}$$

In the range from linear to the end of the saturation we can make the following remarks:

1) The vectors $\boldsymbol{\psi}_\ell$ and $\mathbf{i}_{\mu\ell}$ are both oriented parallel, also during saturation;
2) The factor between ψ_ℓ and $i_{\mu\ell}$ is only constant in the unsaturated range; during saturation the factor will become smaller with an increasing ψ_ℓ.

The value ℓ is a function of ψ_ℓ in the range of saturation, so:

$$\ell = \tan\alpha = \ell(\psi_\ell) \tag{2.4}$$

However in the unsaturated range this equation will become:

$$\ell_0 = \tan\alpha_0 = \text{constant} \tag{2.5}$$

In case of saturation the linear relation between ψ_ℓ and $i_{\mu\ell}$ will become a more general one:

$$\psi_\ell = \ell(\psi_\ell) i_{\mu\ell} \tag{2.6}$$

Figure 2.3 shows the curve of the magnetisation. One can recognize, that $\ell = \tan\alpha$ is a function of ψ_ℓ, in accordance with equation 2.4.

Next we will derive the inverse relation of equation 2.6:

$$i_{\mu\ell} = \frac{1}{\ell(\psi_\ell)}\psi_\ell \tag{2.7}$$

and figure 2.4 shows the inverse relation of figure 2.3.

With this method of approach the value $1/\ell(\psi_\ell)$ determines in equation 2.7 the magnetizing current $i_{\mu\ell}$, which is necessary for creating a specific flux ψ_ℓ. We will get a step further with our new method of approach and change therefore the expression $1/\ell(\psi_\ell)$ into the value $S(\psi_\ell)$:

$$S(\psi_\ell) = \frac{1}{\ell(\psi_\ell)} \tag{2.8}$$

Together with equation 2.7:

$$i_{\mu\ell} = S(\psi_\ell)\,\psi_\ell \tag{2.9}$$

with

$$S(\psi_\ell) = \frac{1}{\tan\alpha(\psi_\ell)} \tag{2.10}$$

The newly introduced value $S(\psi_\ell)$ can be explained by the following consideration:

> When a magnetic circuit has a smaller magnetic conductance, the larger is the magnetizing current to create a specific flux. We can consider a small magnetic conductance as a large magnetic resistance. With this method of consideration a larger magnetic resistance needs a large magnetizing current to create a specific flux. In this way we can consider on the basis of equation 2.9 the value $S(\psi_\ell)$ as a measure for the magnetic resistance of a magnetic circuit.

Figure 2.4 makes clear, that the magnetizing current in point A consists of a current $i_{\mu\ell 0}$, which is the part of the magnetizing current in the unsaturated range and an additive current $i_{\mu\ell z}$, which is only of importance during saturation. The total magnetizing current in point A for creating a specific flux equals:

$$i_{\mu\ell} = i_{\mu\ell 0} + i_{\mu\ell z} \tag{2.11}$$

Because the magnetizing current $i_{\mu\ell}$ consists of the sum of two currents, we can with the help of equation 2.9 also divide the value $S(\psi_\ell)$ into the sum of two S-values:

$$S(\psi_\ell) = S_0 + S_z(\psi_\ell) \tag{2.12}$$

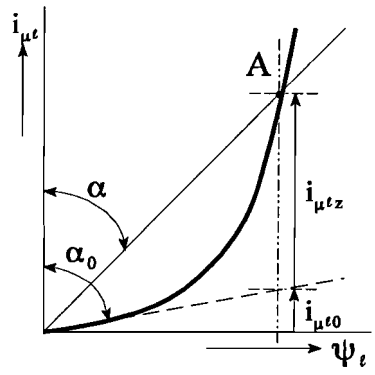

Figure 2.4: The inverse relation between ψ_ℓ and $i_{\mu\ell}$.

Together with equations 2.9 and 2.11 we finally get:

$$i_{\mu\ell} = i_{\mu\ell 0} + i_{\mu\ell z} = [S_0 + S_z(\psi_\ell)]\psi_\ell \tag{2.13}$$

The magnetizing current $i_{\mu\ell}$ can be divided into the following three equations:

$$i_{\mu\ell 0} = S_0 . \psi_\ell \tag{2.14}$$

$$i_{\mu\ell z} = S_z(\psi_\ell) . \psi_\ell \tag{2.15}$$

and

$$i_{\mu r} = i_{\mu \ell 0} + i_{\mu \ell z} \tag{2.16}$$

In which S_0 is a measure for the air-gap magnetic resistance (the magnetic resistance of the iron can be taken zero if no saturation occurs) and $S_z(\psi_\ell)$ a measure for an iron's magnetic resistance, which occurs additively during saturation. The saturation effect can be represented as follows: with increasing flux the iron with its good magnetic conductance progressively becomes overloaded and at the end even a bad magnetic conductor; the iron becomes "porous". The value $S_z(\psi_\ell)$ can also be considered as a measure for the magnetic resistance of a newly originated air way in the iron, which forms itself additively in case of saturation.

The value $S(\psi_\ell)$ as a function of ψ_ℓ can be derived from figure 2.4 and its curve is presented in figure 2.5.

In this section we assumed, that the leakage inductances were not affected during saturation. This assumption is valid for the leakage flux, which arises in the end winding region of the rotor and the stator circuit. This leakage flux flows totally through air, so it won't be saturated. However the leakage flux arising at the rotor's or stator's teeth will rather be affected during saturation, because this magnetic flux flows partly through air but also through iron. We will neglect this influence in the following sections and therefore we consider for the time being ℓ_{ok} and ℓ_{os} constant.

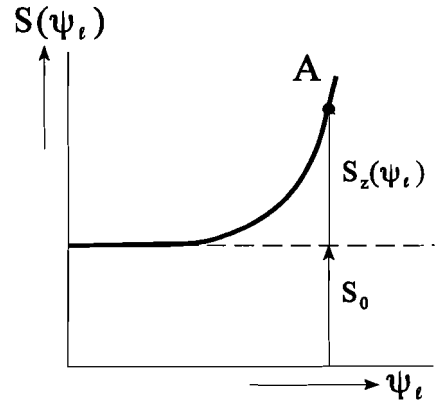

Figure 2.5: The relation between ψ_ℓ and $S(\psi_\ell)$ in the linear and saturated range.

2.2.2 The addition of the saturation effect to the machine structure.

Concluding we can determine, that taking into account the previous considerations equation 2.1 at the beginning of subsection 2.2.1 will change into:

$$\mathbf{i}^a_{\mu\ell} = S(\psi_\ell)\,\boldsymbol{\psi}^a_\ell \tag{2.17}$$

in which

$$S(\psi_\ell) = S_0 + S_z(\psi_\ell) \tag{2.18}$$

When these equations are combined with each other:

$$\mathbf{i}^a_{\mu\ell} = S_0 . \boldsymbol{\psi}^a_\ell + S_z(\psi_\ell) . \boldsymbol{\psi}^a_\ell \tag{2.19}$$

This equation shows very clear, that $\mathbf{i}_{\mu\ell}$ consists of the sum of two vectors, $S_0\,\boldsymbol{\psi}_\ell$ and $S_z(\psi_\ell)\,\boldsymbol{\psi}_\ell$. S_0 is a measure for the air-gap magnetic resistance and $S_z(\psi_\ell)$ is a measure for the magnetic resistance of the "pores" in the iron, which originate during saturation.

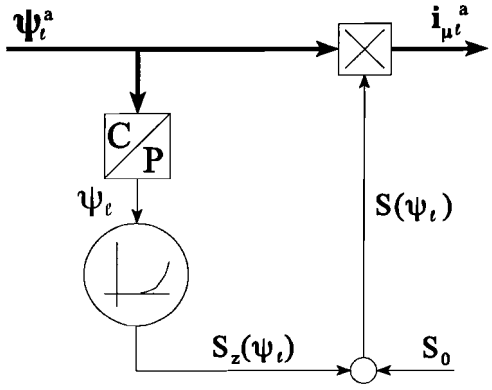

Figure 2.6: The origin of the magnetizing current vector $\mathbf{i}_{\mu\ell}$ with the help of the "multiplicative" method.

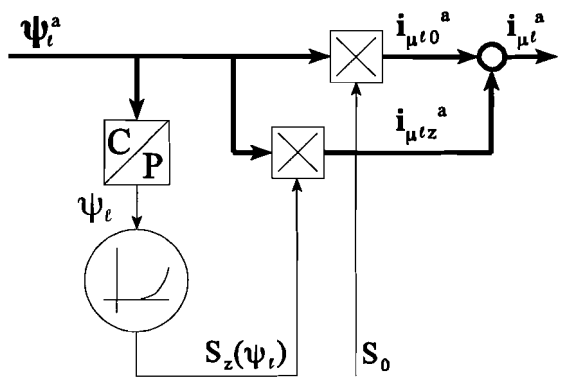

Figure 2.7: The origin of the magnetizing current vector $\mathbf{i}_{\mu\ell}$ with the help of the "additive" method.

The equations 2.17 and 2.18 on the one hand and equation 2.19 on the other hand lead to two equivalent substructures describing the influence of saturation. With the first so-called multiplicative structure (see figure 2.6), the magnetizing current vector $\mathbf{i}_{\mu\ell}$ is created by one mathematical operation, in which the factor $S(\psi_\ell)$ is created by the summation of a constant value S_0 and a ψ_ℓ-dependent factor $S_z(\psi_\ell)$. With the other so-called additive structure (see figure 2.7), the magnetizing current vector $\mathbf{i}_{\mu\ell}$ consists of two current vectors. The vector $\mathbf{i}_{\mu\ell 0}$ creates the flux vector $\boldsymbol{\psi}_\ell$ on the basis of the air-gap magnetic resistance S_0 and the other vector $\mathbf{i}_{\mu\ell z}$ is only of importance during saturation, due to the iron's "porousness".

With the help of these two equivalent relations between $\mathbf{i}_{\mu\ell}$ and $\boldsymbol{\psi}_\ell$, there are two possibilities to describe the influence of saturation. The flux vector $\boldsymbol{\psi}_\ell$ has first to be written in a ψ_k-coordinate system (analogous to Blaschke[4]) , therefore the equations 9.4 to 9.10 (see figure 2.1) and 2.17 to 2.19 have to be transformed to this new coordinate system. The equations 9.9 and 9.10 are scalar equations, which are not influenced by a coordinate transformation. The equations 9.5, 9.7, 9.8, 2.17 and 2.19 are valid for each coordinate system, so they can directly be rewritten in the ψ_k-coordinate system. However equation 9.4 is only valid in the rotor coordinate system and its form will change during the transformation.

Equation 9.4 becomes by transformation:

$$\mathbf{0} = \mathbf{i}_k^\psi . r_k + \dot{\boldsymbol{\psi}}_k^\psi + \dot{\varphi}_k^r . R(\pi/2)\boldsymbol{\psi}_k^\psi \qquad \textbf{(2.20)}$$

and the other vector equations:

$$\boldsymbol{\psi}_k^{\psi} = \boldsymbol{\psi}_\ell^{\psi} + \ell_{\sigma k}.\mathbf{i}_k^{\psi} \tag{2.21}$$

$$\mathbf{i}_{\mu\ell}^{\psi} = S(\psi_\ell).\boldsymbol{\psi}_\ell^{\psi} \tag{2.22}$$

$$\mathbf{i}_{\mu\ell}^{\psi} = \mathbf{i}_s^{\psi} + \mathbf{i}_k^{\psi} \tag{2.23}$$

$$m_{el} = [R(\pi/2)\boldsymbol{\psi}_\ell^{\psi}]^T.\mathbf{i}_s^{\psi} \tag{2.24}$$

and the unchanged scalar equations:

$$\dot{\rho}^s = \tfrac{1}{\theta}\int (m_{el} - m_{load}).dt \tag{2.25}$$

$$\rho^s = \int \dot{\rho}^s.dt \tag{2.26}$$

$$S(\psi_\ell) = S_0 + S_z(\psi_\ell) \tag{2.27}$$

When we substitute the equations 2.22 and 2.23 in equation 2.24:

$$m_{el} = [R(\pi/2)\boldsymbol{\psi}_\ell^{\psi}]^T.[S(\psi_\ell)\boldsymbol{\psi}_\ell^{\psi} - \mathbf{i}_k^{\psi}] \tag{2.28}$$

We simplify this equation with the help of some matrix algebra:

$$m_{el} = [R(\pi/2)\boldsymbol{\psi}_\ell^{\psi}]^T.[-\mathbf{i}_k^{\psi}] \tag{2.29}$$

With respect to equation 2.21 we get:

$$m_{el} = [R(\pi/2).(\boldsymbol{\psi}_k^{\psi} - l_{\sigma k}.\mathbf{i}_k^{\psi})]^T.[-\mathbf{i}_k^{\psi}] \tag{2.30}$$

Finally we can simplify this equation to:

$$m_{el} = [R(\pi/2)\boldsymbol{\psi}_k^{\psi}]^T.[-\mathbf{i}_k^{\psi}] \tag{2.31}$$

When we rewrite the vector equations with the help of the vector's coordinates:

$$\mathbf{i}_s^{\psi} = \begin{bmatrix} i_s^b \\ i_s^w \end{bmatrix} \tag{2.32}$$

and

$$\boldsymbol{\psi}_k^{\psi} = \begin{bmatrix} \psi_k \\ 0 \end{bmatrix} \tag{2.33}$$

We will get the following scalar equations:

$$\dot{\psi}_k = r_k.(-i_k^b) \tag{2.34}$$

$$\dot{\varphi}_k^r = \frac{1}{\psi_k}.r_k.(-i_k^w) \tag{2.35}$$

$$\psi_\ell^b = \psi_k + \ell_{\sigma k}.(-i_k^b) \tag{2.36}$$

$$\psi_\ell^w = \ell_{\sigma k}.(-i_k^w) \tag{2.37}$$

$$i_{\mu\ell}^b = S(\psi_\ell)\psi_\ell^b \tag{2.38}$$

$$i_{\mu\ell}^w = S(\psi_\ell)\psi_\ell^w \tag{2.39}$$

The length of the air-gap flux can be calculated with its Cartesian coordinates:

$$\psi_\ell = \sqrt{(\psi_\ell^b)^2 + (\psi_\ell^w)^2} \tag{2.40}$$

Further the magnetizing current equations:

$$-i_k^b = i_s^b - i_{\mu\ell}^b \tag{2.41}$$

and

$$-i_k^w = i_s^w - i_{\mu\ell}^w \tag{2.42}$$

The simple description of the electromagnetic torque:

$$m_{el} = \psi_k.(-i_k^w) \tag{2.43}$$

and finally the equations 2.25 to 2.27:

$$\dot{\rho}^s = \tfrac{1}{\theta}\int (m_{el} - m_{load}).dt \tag{2.44}$$

$$\rho^s = \int \dot{\rho}^s.dt \tag{2.45}$$

$$S(\psi_\ell) = S_0 + S_z(\psi_\ell) \tag{2.46}$$

The only equations, which still remain, provide the conversion of the stator current vector $\mathbf{i}_s$ from the stator coordinate system into the ψ_k-coordinate system:

$$i_s^b = i_s.\cos\varepsilon_s^\psi \tag{2.47}$$

$$i_s^w = i_s.\sin\varepsilon_s^\psi \tag{2.48}$$

$$\varepsilon_s^\psi = \varepsilon_s^s - \varphi_k^s \tag{2.49}$$

$$\varphi_k^s = \varphi_k^r + \rho^s \tag{2.50}$$

Figure 2.8a shows the block structure of the equations above. Figure 2.8b shows the structure for the situation when the Cartesian coordinates of the stator current are available. It's obvious that these structures are totally equivalent, so we will apply the most ideal structure in the next sections.

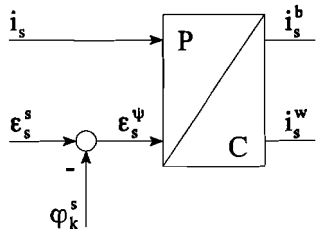

Figure 2.8a: Transformation of the polar input values into the field oriented coordinates.

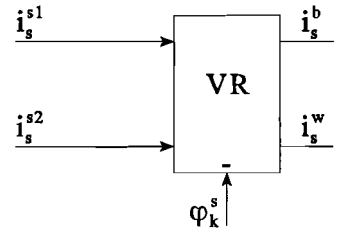

Figure 2.8b: Transformation of the Cartesian input values into the field oriented coordinates.

Figure 2.9 presents the structure of the induction machine affected with main flux saturation. The equations 2.34 to 2.50 describe the machine structure. This structure is valid for every situation (with the assumption: leakage flux won't be saturated). However in the next subsection we want to derive equivalent structures which can be added additionally to the machine structure already affected with rotor leakage inductance, presented in Blaschke[4]. The stator leakage flux isn't of importance, because we will supply the machine with a current source.

2.2.3 The different machine structures with respect to saturation.

When we look at figure 2.9, we see that with the help of the air-gap flux the magnetizing current vector is formed. The first coordinate of this vector $i_{\mu\ell}^b$ influences the current loop of i_s^b and the second coordinate $i_{\mu\ell}^w$ influences the second current loop of i_s^w. We will analyse these two current loops further.

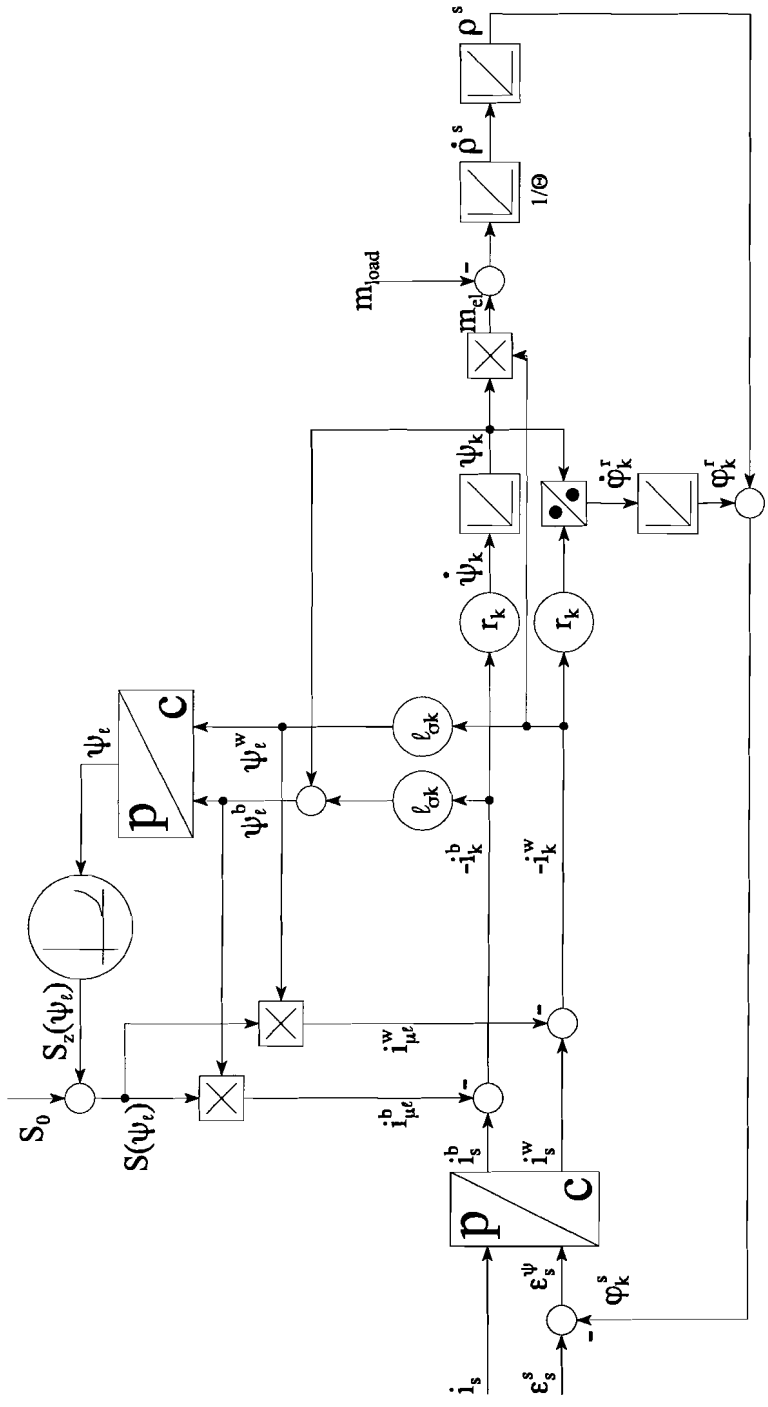

Figure 2.9: A machine structure of the induction machine affected with saturation.

Figure 2.9 shows that $i_{\mu\ell}^{b}$ consists of the summation of four elements:

$$i_{\mu\ell}^{b} = S_0.\psi_k + S_z(\psi_t).\psi_k + S_0.\ell_{\sigma k}.(-i_k^b) + S_z(\psi_t).\ell_{\sigma k}.(-i_k^b) \qquad \textbf{(2.51)}$$

Figure 2.10a shows extensively the formation of the first coordinate of the air-gap magnetizing current vector. Analogous we will find for $i_{\mu\ell}^{w}$:

$$i_{\mu\ell}^{w} = S_0.\ell_{\sigma k}.(-i_k^w) + S_z(\psi_t).\ell_{\sigma k}.(-i_k^w) \qquad \textbf{(2.52)}$$

The relation between i_s^w and $-i_k^w$ is presented in figure 2.10b. We can remark with the help of simple machine theory that during unloaded condition the magnetic flux is just formed by multiplication of the first coordinate of the stator current i_s^b and the main inductance. During ideal unloaded condition, i.e. i_k is equal to zero, the behaviour of the machine is quite simular with a normal inductor.

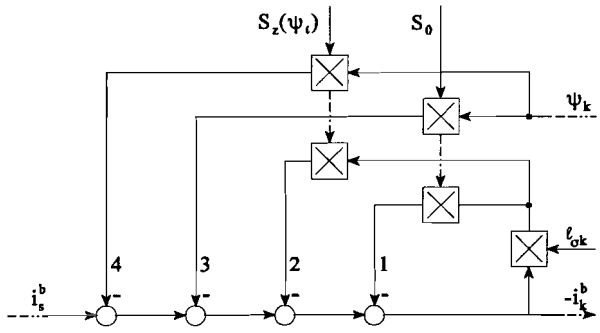

Figure 2.10a: The feedback of the rotor flux and leakage flux on the first current coordinate.

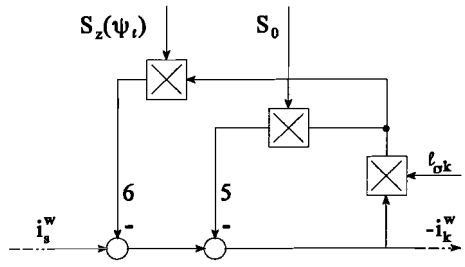

Figure 2.10b: The feedback of the leakage flux on the second current coordinate.

There are six different loops in figure 2.10. First we will distinguish the loops: loops 1, 2, 5, 6 (result of $-i_k^b$ and $-i_k^w$) and loops 3, 4 (result of ψ_k). Also we can distinguish these loops by the different multiplication factors: S_0 (loops 1, 3, 5) and $S_z(\psi_t)$ (loops 2, 4, 6).

The first distinction can be considered as a proportional feedback system as shown in figure 2.11a. However we can convert this system into a feedforward system:

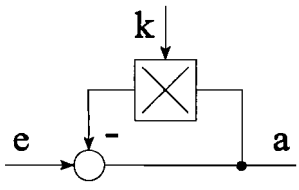

Figure 2.11a: A proportional feedback system.

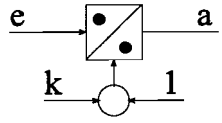

Figure 2.11b: The feedforward equivalent of figure 2.11a.

$$e - k.a = a \tag{2.53}$$

resulting in:

$$a = \frac{e}{1+k} \tag{2.54}$$

which is presented in figure 2.11b.

The second distinction shows the difference between the linear range and the saturated range. In case of linearity (no saturation) the following equation is valid:

$$S_z(\psi_\ell)=0 \tag{2.55}$$

In figure 2.10 only the loops 1, 3 and 5 will remain in case of linearity. We can rewrite loops 1 and 5 with the help of equation 2.54:

$$\frac{1}{1+S_0\ell_{\sigma k}} \tag{2.56}$$

This factor is the amplification between $(i_s^b - S_0\psi_k)$ and $(-i_k^b)$, and (i_s^w) and $(-i_k^w)$. In figure 2.12 is shown the resulting structure of figure 2.10 in case of non-saturation. When we substitute this structure within the machine structure (see figure 2.9) we will become the linear machine structure, presented in Blaschke[4][1]. This machine structure is presented in figure 2.13. The electromagnetic torque is formed by the multiplication of a flux and a current. The main flux is caused by the main inductance in the stator and the rotor current is an effect of an alternating flux (only during asynchronous condition), which induces a voltage in the rotor and thus a current (the rotor is shorted).

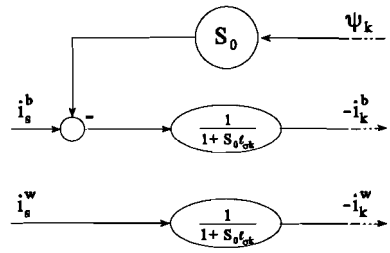

Figure 2.12: Substructure for the non-saturation case.

So far the non-saturation case. We will now derive an additional structure to the machine structure of figure 2.13. In case of saturation equation 2.55 is no longer valid:

$$S_z(\psi_\ell) \neq 0 \tag{2.57}$$

It implies that the loops 2, 4 and 6 of figure 2.10 can't be ignored anymore. The factor $S_z(\psi_\ell)$ influences the magnetizing current, therefore we will take loops 2 and 4 together and name them: $i_{\mu\ell z}{}^b$. We will convert loop 6 directly into an additional magnetizing current: $i_{\mu\ell z}{}^w$. Subtracting these two additional magnetizing currents directly from the stator current (in ψ_k-coordinates) a machine structure remains which is also valid during saturation. Figure 2.14 shows this new "additive" machine structure. The additional structure in comparison with figure 2.13 is bold printed.

[1]The linear factors $\frac{1}{\ell}$ and σ_k in Blaschke[4] are in this report replaced by the factors: S_0 and $S_0\ell_{\sigma k}$.

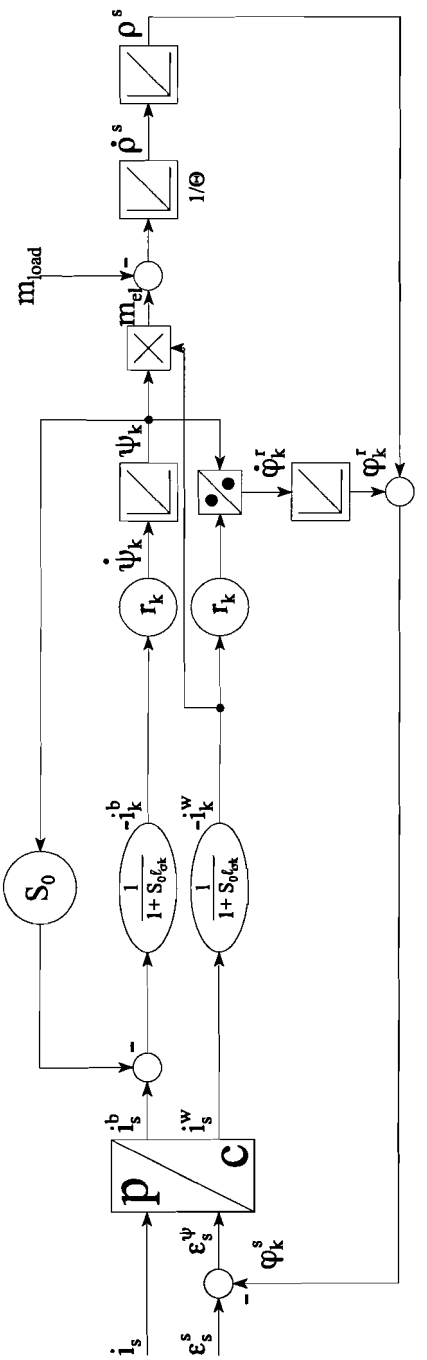

Figure 2.13: The machine structure of the induction machine affected with leakage flux, presented in Blaschke[4].

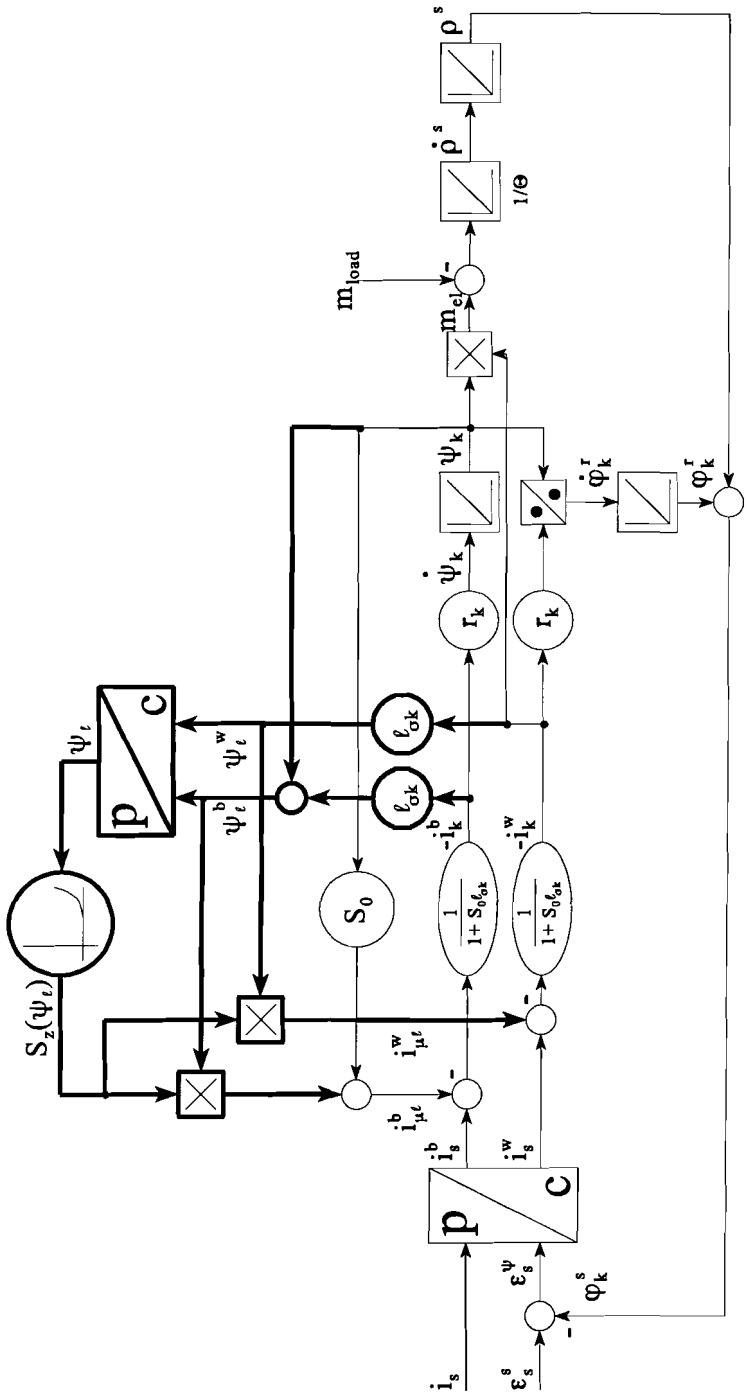

Figure 2.14: The "additive" machine structure of the current fed induction machine affected with saturation.

There is also another method to obtain a machine structure. Looking at the four loops most inside (1, 2, 5 and 6) (figure 2.10), we can rewrite these feedback systems with the help of equation 2.54. The variable feedback gain:

$$\ell_{\sigma k}.[S_0 + S_z(\psi_t)] = \ell_{\sigma k}.S(\psi_t) \qquad \textbf{(2.58)}$$

can be rewritten as a feedforward variable gain:

$$\frac{1}{1+S(\psi_t).\ell_{\sigma k}} \qquad \textbf{(2.59)}$$

Also the feedback gains of the other loops (3 and 4) will be taken together in one variable:

$$S_0 + S_z(\psi_t) = S(\psi_t) \qquad \textbf{(2.60)}$$

Figure 2.15 shows a part of the machine structure which is valid for saturation. Finally this structure is substituted in the machine structure of figure 2.13 (see figure 2.16). In case of linearity (i.e. $S_z(\psi_t) = 0$), this structure will be equal to the machine structure presented in Blaschke[4] (see figure 2.13). The additional structure in comparison with figure 2.13 is bold printed. This second machine structure is called the "multiplicative" structure.

The previous subsections delivered us three equivalent machine structures: figure 2.9, 2.14 and 2.16. The first structure will not be considered for application, because this structure differs to much from the already available structure (see figure 2.13). The choice between the second or third structure is totally voluntary. Finally we have chosen to implement the "multiplicative" machine structure (see figure 2.16), only by reason of the ease of implementation in the already partly available soft- and hardware.

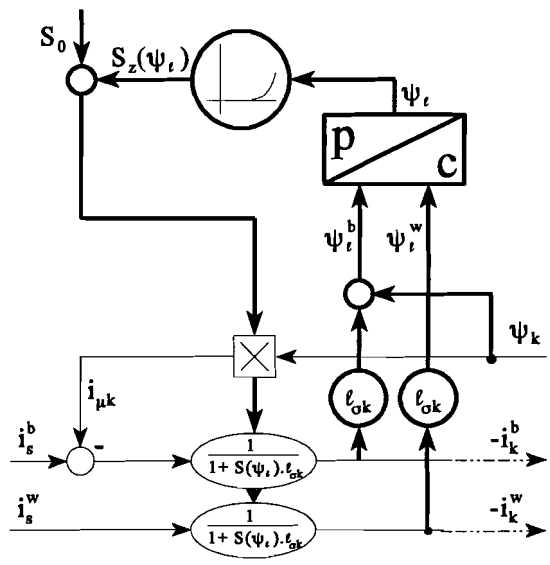

Figure 2.15: Substructure for saturation.

With the help of the new machine structures we are able to derive a field oriented control which takes into account the influence of the saturation effect.

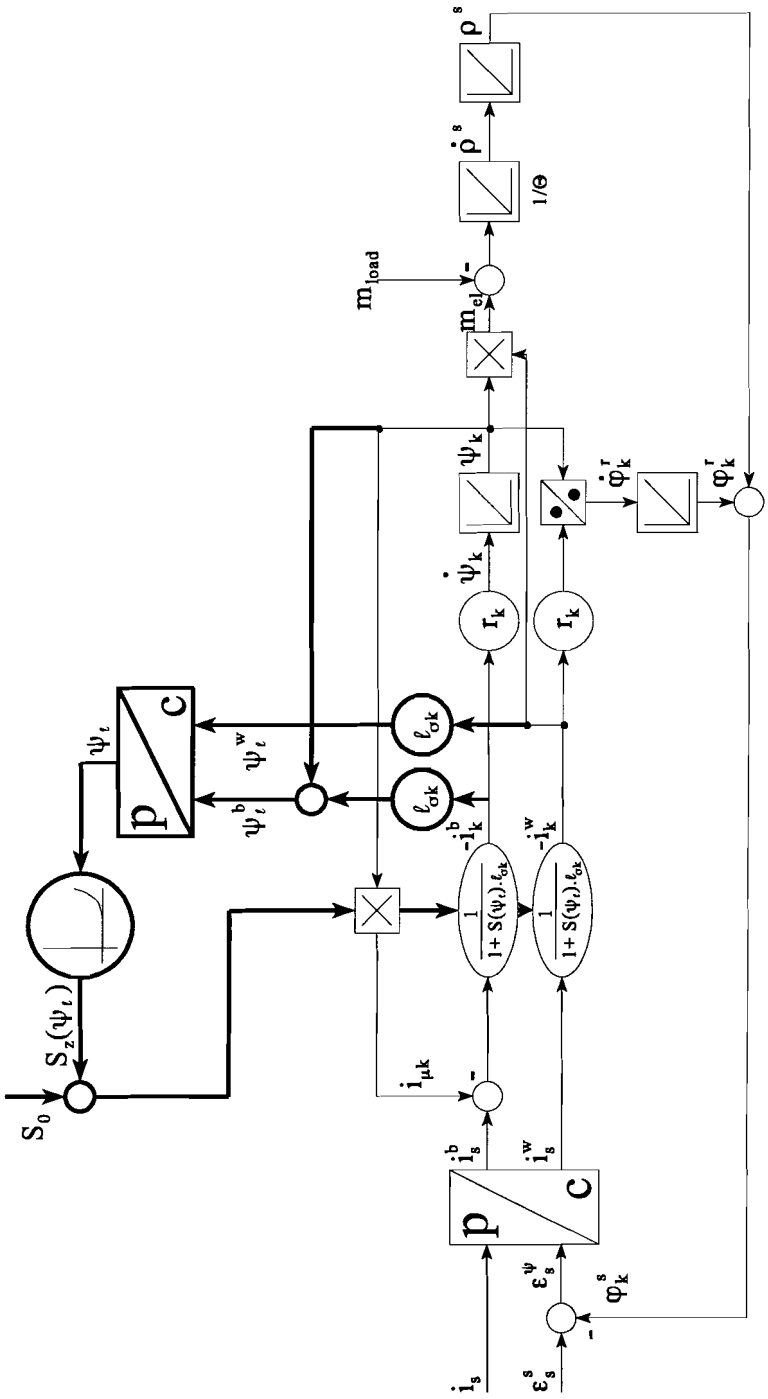

Figure 2.16: The "multiplicative" machine structure of the current fed induction machine affected with saturation.

2.3 A short introduction to Field Oriented Control.

A highly sophisticated control of an induction machine, or more in general an electric machine, implies that the flux level in the machine and the torque can be controlled independently of each other. The torque is of course essential for the desired work (eg. accelerating a train) and the flux level indicates a measure for the efficiency of the machine. Field Oriented Control offers the possibility to exploit the induction machine with a high performance. Therefore since the invention of Field Oriented Control in the seventies, the induction machine is a serious alternative for the those days very popular DC drives. The DC machine itself is very easy to control: the magnetic field (the flux level) can be controlled by changing the stator current and the torque can be controlled by changing the rotor current. However the industry is very interested in new control techniques for the induction machine, because this machine is almost maintenance-free and very robust in comparison with the DC machine. Also the purchase of an induction machine is very favourable with respect to a DC machine.

A view at the structure of the induction machine (see figure 2.16) shows that the flux level and the torque depend on the input values: the current and it's angle or frequency. A Field Oriented Control transforms the desired values of the flux and the torque into the values of the machine's terminal quantities: current (i_s^*) or voltage (u_s^*) and their respective angles (ε_s^{s*}, α_s^{s*}) or frequencies ($\dot{\varepsilon}_s^{s*}$, $\dot{\alpha}_s^{s*}$).

2.3.1 Derivation of the Field Orientation of the machine structure affected with saturation.

With the help of the equations (2.34 - 2.50), presented in section 2.2, we will derive a mathematical description of the relation between the desired values ψ_k^* and m_{el}^* and the values i_s^* and ε_s^{s*}.

First we will transform the stator current from the field oriented reference frame (ψ_k-coordinate system) into the stator reference frame:

$$\mathbf{i}_s^{s*} = R(\varphi_k^s)\,\mathbf{i}_s^{\psi*} \tag{2.61}$$

Figure 2.17a shows the relation between the field oriented stator current coordinates and the output values, rotor flux and torque (ψ_k and m_{el}) and figure 2.17b shows the origin of the air-gap flux. These substructures are a part of the machine structure, presented in figure 2.16. With the help of these substructures we are able to derive the inverse relation and thus the field oriented control algorithm.

The first coordinate of the field oriented stator current can be found with the help of equations 2.36, 2.38 and 2.41:

$$i_s^{b*} = (1+\hat{S}(\psi_\ell).\hat{\ell}_{\sigma k}).(-i_k^b) + \psi_k.\hat{S}(\psi_\ell) \tag{2.62}$$

with (see also equation 2.34)

$$(-i_k^b) = \frac{\dot{\psi}_k^*}{\hat{r}_k} \tag{2.63}$$

and the second coordinate with the help of equation 2.37, 2.39 and 2.42:

$$i_s^{w*} = (1+\hat{S}(\psi_\ell).\hat{\ell}_{\sigma k}).(-i_k^{w*}) \tag{2.64}$$

the cause of $(-i_k^{w*})$ (see equation 2.43):

$$(-i_k^{w*}) = m_{el}^* . \frac{1}{\psi_k} \tag{2.65}$$

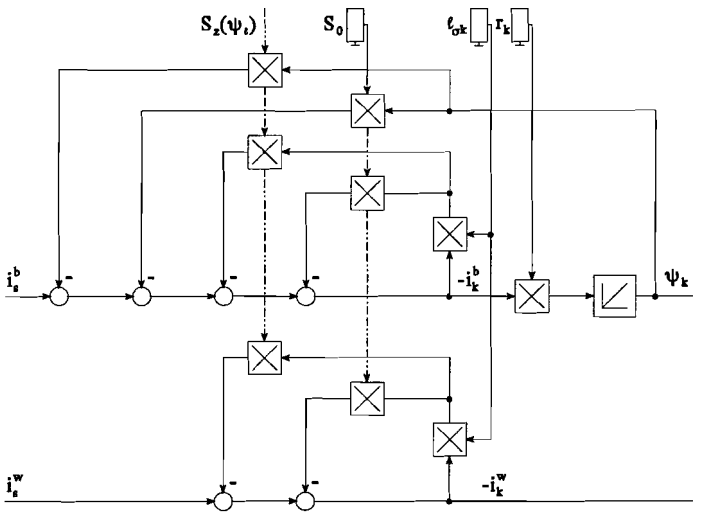

Figure 2.17a: Substructure of the induction machine affected with saturation.

Next we have to estimate the saturation value $S_z(\psi_\ell)$, but this value depends on the air-gap flux. So we have to estimate ψ_ℓ first (see equations 2.36, 2.37 and 2.40):

$$\hat{\psi}_\ell = \sqrt{(\hat{\psi}_\ell^b)^2 + (\hat{\psi}_\ell^w)^2} \tag{2.66}$$

with

$$\hat{\psi}_\ell^b = \psi_k^* + \hat{\ell}_{\sigma k}.(-\hat{i}_k^b) \tag{2.67}$$

and

$$\hat{\psi}_\ell^w = \hat{\ell}_{\sigma k}.(-i_k^{w*}) \tag{2.68}$$

Figure 2.18 shows the field oriented control of the induction machine affected with saturation.

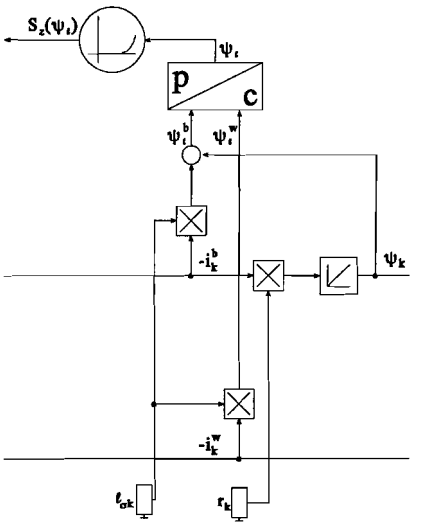

Figure 2.17b: The origin of the saturation value $S_z(\psi_\ell)$ in the machine structure.

The ideal situation:

$$\hat{r}_k = r_k \tag{2.69}$$

$$\hat{S}_0 = S_0 \tag{2.70}$$

$$\hat{S}_z(\psi_r) = S_z(\psi_\ell) \tag{2.71}$$

and

$$\hat{\ell}_{\sigma k} = \ell_{\sigma k} \tag{2.72}$$

provides the condition for an ideal field oriented control: the real values of flux and torque are equal to their desired values:

$$m_{el} = m_{el}^* \tag{2.73}$$

and

$$\psi_k = \psi_k^* \tag{2.74}$$

During the derivation of the field oriented control algorithm we pretended, that the position and the length of the flux vector was available. However, obtaining the flux vector in practice is much more difficult than for instance a current measurement. Therefore a lot of research is done in the field of flux locating. In the next chapter we will discuss the different possibilities locating the flux in an induction machine. Finally we will derive a new model for obtaining the flux position in a slip ring induction machine.

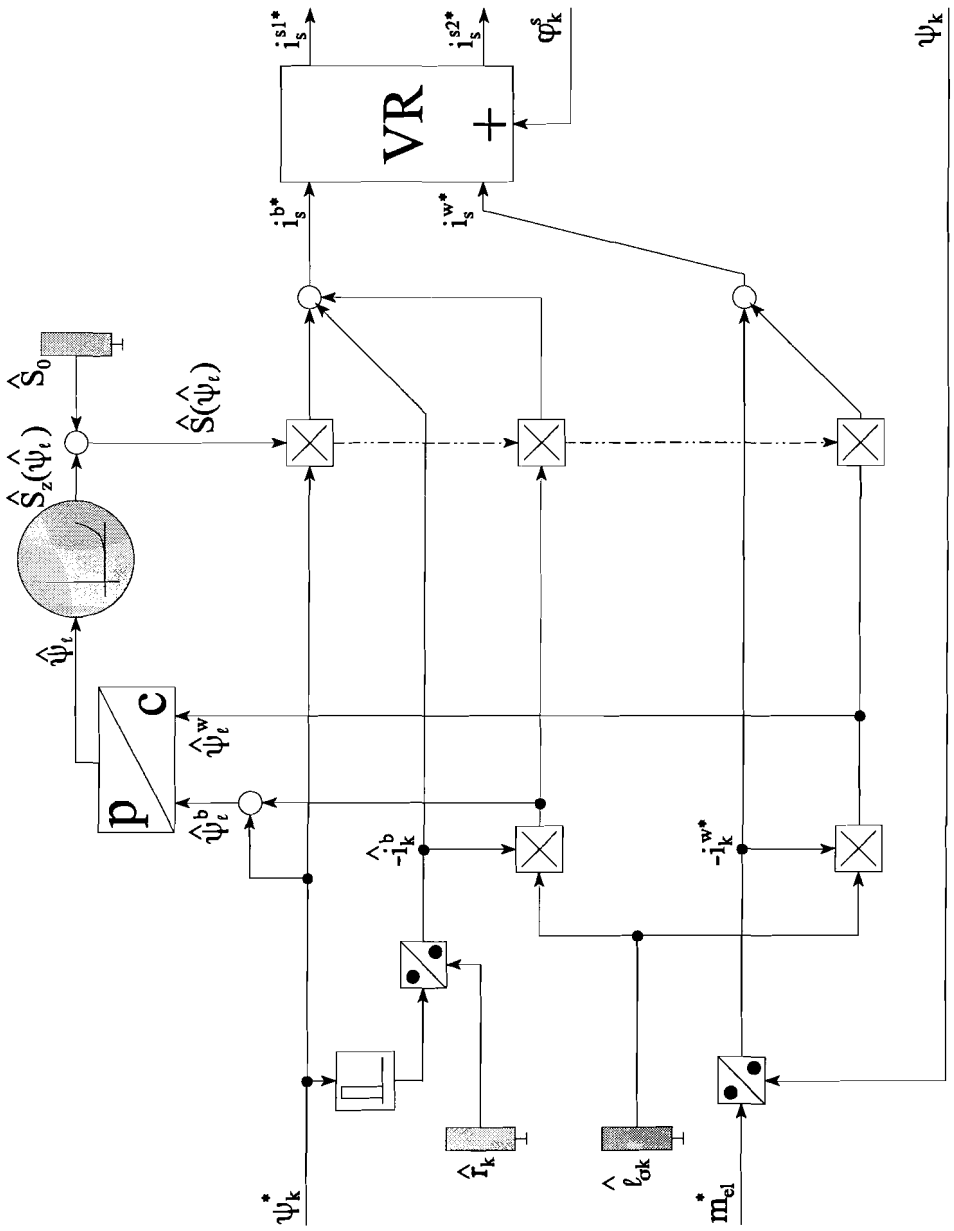

Figure 2.18: Field Oriented Control of the current fed induction machine affected with saturation.

CHAPTER 3

LOCATING THE FLUX POSITION IN AN INDUCTION MACHINE

3.1 Introduction.

For Field Oriented Control it is essential to know the position of the flux in the machine. There are of course different possibilities obtaining the flux vector in an induction machine. The most obvious method is a direct measurement of the flux with the help of Hall-sensors. A great disadvantage of a measurement with these sensors is the lack of robustness, because these sensors are very delicate. Further the positioning of the sensors is precision work. The industry in general wants to develop controlled drive systems which are very robust (i.e. they are insensitive for disturbances).

Another method for flux locating is the U/I-model. This model estimates the flux vector with the help of the stator equation:

$$\mathbf{u}_s^s = r_s.\mathbf{i}_s^s + \dot{\boldsymbol{\psi}}_s^s \qquad (3.1)$$

First the ohmic voltage drop over the stator resistance is subtracted from the stator voltage; after integration the stator flux will remain. For this model we need to measure the stator voltage and current. Further we need to identify the stator resistance. Unfortunately this resistance is not constant due to its non-negligible temperature coefficient. At low frequencies this will result in a certain error and at lower frequencies the integrator will even drift away. However the performance of this model at high frequencies is outstanding. Therefore a lot of research is done in the field of flux locating around frequency zero. In Burgt[12] an adaption of the U/I-model is presented. This variant delivers an improvement of the performance of the U/I-model down to a frequency of 0.05 PU. However, at frequency zero it doesn't still give any satisfaction.

The last years some articles have been published (see: Blaschke[6], Sung-Il Yong[31]), which present new techniques eliminating the "low frequency" problem. Both articles make use of the addition of a current with a higher frequency than that of the stator's main current. At low frequencies Blaschke[6] uses a current injection with a relative low frequency of 0.4 PU. Sung-Il Yong[31], however uses a current with a much higher frequency (10 PU). The amplitude of the injected current is a compromise between the performance of the U/I-model and the torque performance of the machine. A current injection with a large amplitude will result in a relative large torque ripple around the desired value.

The new techniques mentioned above present an estimation of the real flux axis, also at low frequencies. However during a scientific analysis of these techniques we need a reference model, that will give as accurately as possible the real flux axis, especially at low frequencies. Therefore we will derive a new flux locating model (model C). This model is only applicable to a slip ring induction machine; this indicates once again the "scientific" character of this model. In the first instance the industry is not interested in controlled drives with slip ring induction machines, because these machines require more maintenance and the installation is more complicated than drives with squirrel cage induction machines.

3.2 Model C, a new model for flux locating in a slip ring induction machine.

This model will present an estimation of the flux axis with the help of the magnetizing equation 9.6 of figure 2.1:

$$\mathbf{i}^a_{\mu\ell} = \mathbf{i}^a_s + \mathbf{i}^s_k \tag{3.2}$$

The magnetizing current $\mathbf{i}_{\mu\ell}$ is responsible for the air-gap flux $\boldsymbol{\psi}_\ell$ (see equations 2.6 and 2.8):

$$\boldsymbol{\psi}^a_\ell = \frac{1}{S(\psi_\ell)} \cdot \mathbf{i}^a_{\mu\ell} \tag{3.3}$$

However the field oriented control algorithm (see figure 2.18) uses the rotor flux vector $\boldsymbol{\psi}_k$. So we have to build the rotor flux with the help of equation 9.5 (figure 2.1):

$$\boldsymbol{\psi}^a_k = \boldsymbol{\psi}^a_\ell + \ell_{\sigma k} \cdot \mathbf{i}^a_k \tag{3.4}$$

Figure 3.1 shows the vector diagram of the construction of the rotor flux with the help of equation 3.4. Along the air-gap flux vector $\boldsymbol{\psi}_\ell$ we can draw the magnetizing current vector $\mathbf{i}_{\mu\ell}$. However parallel to the rotor flux vector we can imagine also a certain magnetizing current vector. We will call this vector the "fictitious" magnetizing current vector $\mathbf{i}_{\mu k}$. With the help of some goniometry, figure 3.2 originates. This figure plays a very important role in this new model.

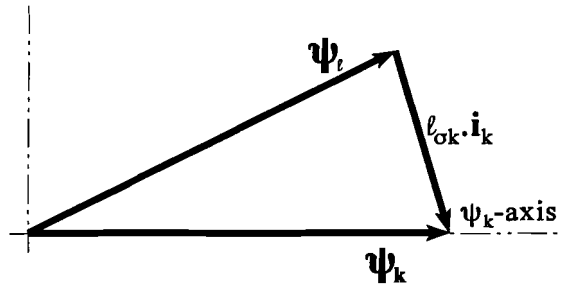

Figure 3.1: Vector diagram of the construction of the rotor flux from the air-gap flux.

From this figure we can obtain the following equations:

$$\boldsymbol{\psi}^s_k = \frac{1}{S(\psi_\ell)} \cdot \mathbf{i}^s_{\mu k} \tag{3.5}$$

$$\mathbf{i}^s_{\mu k} = \mathbf{i}^s_{\mu \ell} + S(\psi_\ell).\ell_{\sigma k}.\mathbf{i}^s_k \qquad (3.6)$$

and together with equation 3.2 we will finally get:

$$\boldsymbol{\psi}^s_k = \frac{1}{S(\psi_\ell)}.[\mathbf{i}^s_s + (1+S(\psi_\ell).\ell_{\sigma k}).\mathbf{i}^s_k] \qquad (3.7)$$

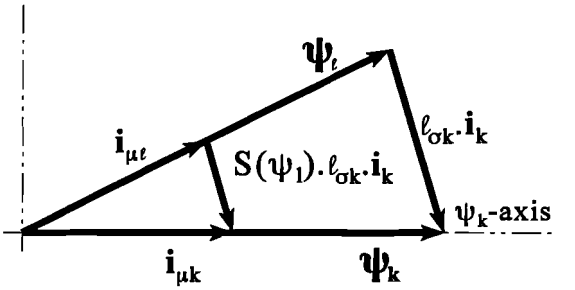

Figure 3.2: Vector diagram of the construction of the rotor flux from the air-gap flux and their magnetizing currents.

During the derivation of the rotor flux from the current vectors $\mathbf{i}_s^s$ and $\mathbf{i}_k^s$, we pretended that the rotor current vector $\mathbf{i}_k^s$ was available. However a measurement of the rotor current will only give us the vector $\mathbf{i}_k^r$, so this vector has to be transformed to the stator coordinate system:

$$\mathbf{i}^s_k = R(\rho^s).\mathbf{i}^r_k \qquad (3.8)$$

The rotor angle ρ^s can be obtained with the help of a resolver, which gives the rotor angle with a high accuracy. However, there will often be an error in the measured angle, because it's possible that the resolver is not correctly mounted onto the shaft. Thus instead of the real rotor angle ρ^s, we will measure the angle with a certain deviation δ, which will be eliminated by a correction angle;

$$\hat{\rho}^{s\,c} = \overset{o}{\rho}{}^s + \hat{\chi}^c \qquad (3.9)$$

Further we will measure the rotor current from the rotor terminals, while all the used equations have been observed from the stator terminals. This will imply, that we have to correct the measured rotor current with a certain ratio factor between the rotor and stator windings:

$$\hat{\mathbf{i}}^{r\,c}_k = \hat{K}^c \,.\, \overset{o}{\mathbf{i}}{}^r_k \qquad (3.10)$$

wherein

$$\hat{K}^c = \frac{w_k}{w_s} \qquad (3.11)$$

describes the relation between the rotor and stator windings. Figure 3.3 finally shows the construction of the rotor current written in the stator coordinate system and corrected with a certain winding relation.

Finally, we have to build the $S(\psi_\ell)$-function. With the help of equations 2.6 and 2.8 we will find:

$$\hat{\psi}^c_\ell = \frac{1}{\hat{S}^c(\hat{\psi}^c_\ell)}.\hat{i}^c_{\mu \ell} \qquad (3.12)$$

This equation is a classical example of an algebraic loop: the output itself depends on values, which are only known when the output is available. These loops can be rewritten into a sort of feedforward system (see for instance figures 2.11a and 2.11b). However for didactical reasons we will ignore these loops, but during the experiments these loops will be rewritten, in such a way there is no algebraic loop anymore. For clearness figure 3.4 shows the origin of $S(\psi_\ell)$ in model C.

Figure 3.5 finally presents model C. This model offers a lot of results, but it does also take a lot of effort:

- This model is only applicable to an induction machine with slip rings.
- At least four current measurements are needed.
- A resolver with a high resolution is necessary.
- Identification of four parameters and one function: $\hat{K}$, $\hat{\chi}$, $\hat{\ell}_{\sigma k}$, $\hat{S}_0$ and $\hat{S}_z(\psi_\ell)$.
- This model can estimate the real flux axis in the whole frequency range, especially at low and very low frequencies, when the classical U/I-model fails as well as during saturation.
- The parameters of this model can be considered as time-independent. A good identification procedure ensures a good functioning of this model.

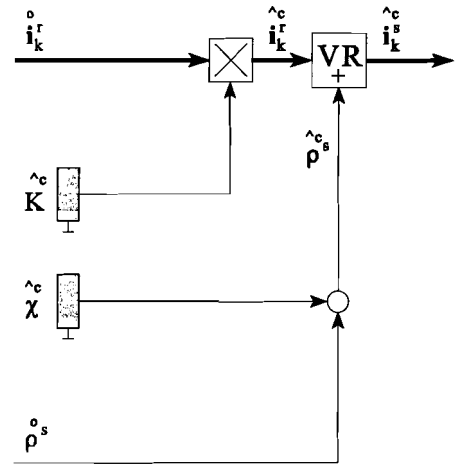

Figure 3.3: The construction of the rotor current vector $\mathbf{i}_k^s$ in model C.

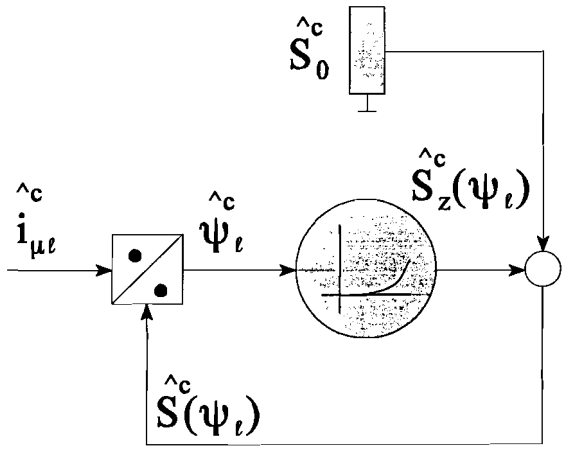

Figure 3.4: The origin of the $S(\psi_\ell)$-function in model C.

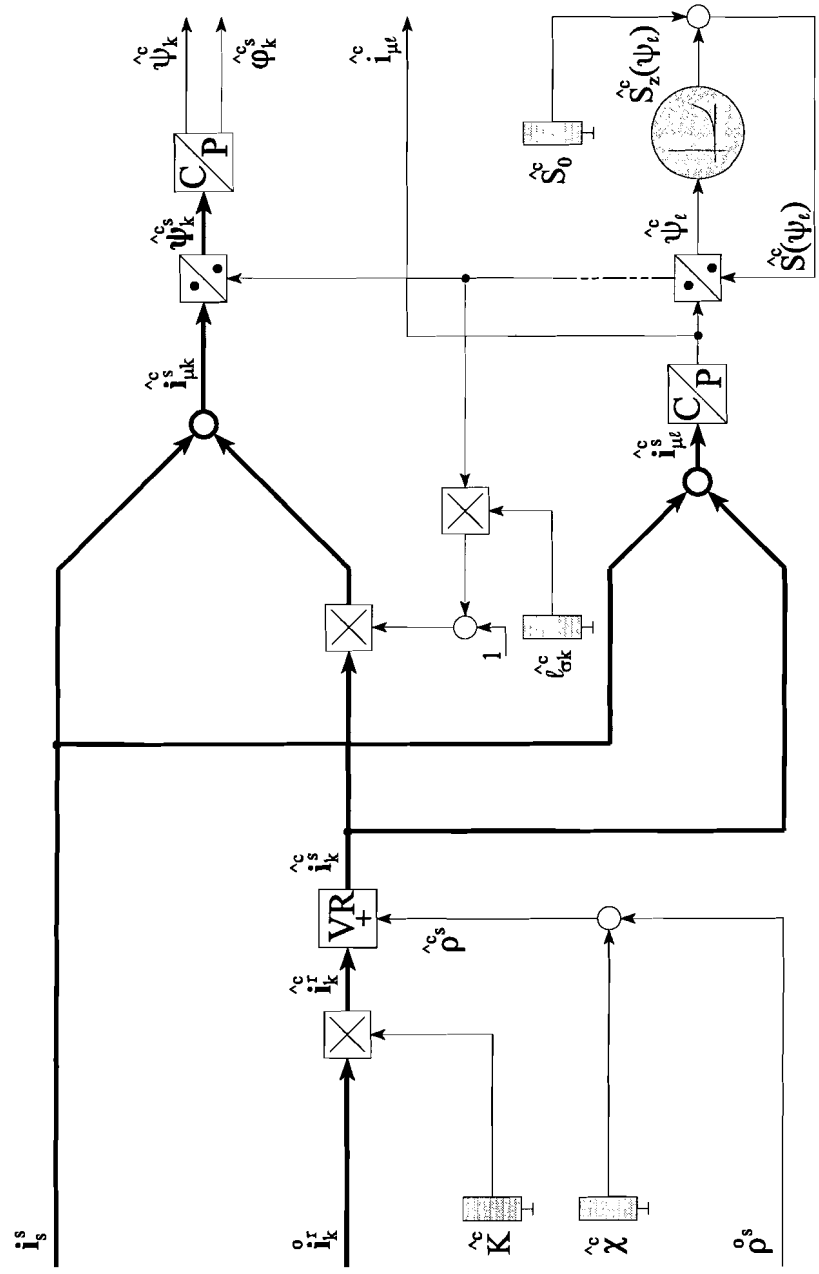

Figure 3.5: Model C, a new model for flux locating in a slip ring induction machine.

3.3 Parameter identification of model C.

This section will present the parameter identification techniques for model C. These techniques make use the characteristics of the induction machine during the steady state. The parameters are identified in a particular sequence. First we will identify the windings ratio factor K. After that we will identify the compensation for the rotor error angle χ. During the identification of the inductances we need the U/I-model. So first we have to identify the stator resistance (we will only use the stator flux of the U/I-model, so we do not need to identify the leakage inductances). Then we are able to identify the stator and rotor leakage inductances and the $S(\psi_\ell)$-values in every working point. Especially the values of the leakage inductances during saturation are very important.

3.3.1 Identification of the winding ratio factor K.

For the theory which is necessary to derive the identification method of the winding ratio, we have to look at the origin of the air-gap flux due to the rotor and stator current distributions along the air-gap circumference. Just like the derivation of the machine structure in chapter 2, we will start from equations presented in Blaschke[4]. For clearness these equations are shown in figure 3.6.

$$v = \frac{w}{2r} \qquad \textbf{(4.10)}$$

$$\mathbf{a}_k^r = v.R(-\pi/2)\mathbf{i}_k^r \qquad \textbf{(4.121)}$$

$$c_I = \frac{\mu_0 . r}{d} \qquad \textbf{(4.62)}$$

$$\boldsymbol{\psi}_\ell^s = c_{III}.\mathbf{b}_\ell^s \qquad \textbf{(4.125)}$$

$$\mathbf{b}_\ell^r = R(-\rho^s)\mathbf{b}_\ell^s \qquad \textbf{(4.71)}$$

$$\boldsymbol{\psi}_\ell^r = c_{III}.\mathbf{b}_\ell^r \qquad \textbf{(4.126)}$$

$$c_{III} = \frac{r.g.w.\pi}{2} \qquad \textbf{(4.72)}$$

$$\mathbf{a}_{\mu\ell}^s = \mathbf{a}_s^s + \mathbf{a}_r^s + \mathbf{a}_k^s \qquad \textbf{(4.127)}$$

$$\mathbf{a}_s^s = v.R(-\pi/2)\mathbf{i}_s^s \qquad \textbf{(4.119)}$$

$$\mathbf{b}_I^s = c_I.R(\pi/2)\mathbf{a}_{\mu\ell}^s \qquad \textbf{(4.129)}$$

Figure 3.6: The equations of the current distributions and induction vectors, presented in Blaschke[4] (chapter 4).

This figure presents a number of new variables, known as:

r	-	radius of the stator bore
g	-	active length of the machine
μ_0	-	permeability constant of air
d	-	air-gap distance
w	-	number of stator and rotor windings

The equations of figure 3.6 are valid for machines with equal number of stator and rotor windings (i.e. $w_s = w_k$). However, in our situation it is not the case. So we have to derive new equations which are valid in the more general situation of unequal stator and rotor windings (i.e. $w_s \neq w_k$).

The variable w will be split into w_s (number of stator windings) and w_k (number of rotor windings). Consequently equations 4.10 and 4.72 of figure 3.6 can be rewritten into the more general equations:

$$v_s = \frac{w_s}{2r} \tag{3.13}$$

$$v_k = \frac{w_k}{2r} \tag{3.14}$$

$$c_{IIIs} = \frac{r.g.w_s.\pi}{2} \tag{3.15}$$

$$c_{IIIk} = \frac{r.g.w_k.\pi}{2} \tag{3.16}$$

Analogous to equation 3.10 we will introduce two vectors which are observed from the rotor terminals: $\overset{o}{\mathbf{i}}{}^r_k$ and $\overset{o}{\boldsymbol{\psi}}{}^r_\ell$.
This will result in the following equations for the more general situation, i.e. $w_s \neq w_k$:

$$\mathbf{a}^s_s = v_s.R(-\pi/2).\mathbf{i}^s_s \tag{3.19}$$

$$\mathbf{a}^r_k = v_k.R(-\pi/2).\overset{o}{\mathbf{i}}{}^r_k \tag{3.20}$$

$$\boldsymbol{\psi}^s_\ell = c_{IIIs}.\mathbf{b}^s_\ell \tag{3.21}$$

$$\overset{o}{\psi}{}^{r}_{\ell} = c_{III k}.\mathbf{b}^{r}_{\ell} \tag{3.22}$$

$$\mathbf{b}^{r}_{\ell} = R(-\rho^{s}).\mathbf{b}^{s}_{\ell} \tag{3.23}$$

Further we need the transformation of the rotor current distribution from the rotor coordinate system into the stator's:

$$\mathbf{a}^{s}_{k} = R(\rho^{s}).\mathbf{a}^{r}_{k} \tag{3.24}$$

In our situation a rotor excitation winding (as in a synchronous machine) does not exist, so equation 4.127 (see figure 3.6) can be reduced to:

$$\mathbf{a}^{s}_{\mu\ell} = \mathbf{a}^{s}_{s} + \mathbf{a}^{s}_{k} \tag{3.25}$$

These equations are taken together in a structure, which is shown in figure 3.7. However we can rewrite the rotor winding constants with the help of the winding ratio factor K:

$$K = \frac{w_k}{w_s} \tag{3.26}$$

Equation 3.14 will change into:

$$v_k = K.v_s \tag{3.27}$$

and equation 3.16:

$$c_{III k} = K.c_{III s} \tag{3.28}$$

This will result in another structure which is presented in figure 3.8. The substructure from A to B represents the situation with equal number of windings. We will now introduce the estimation of the winding ratio factor K. Adding this estimation appropriately to this substructure, a substructure with equal number of windings will remain in case of a right identification of K. Further we can shift the linear mathematical operations together into one mathematical operation with a multiplying factor:

$$S = \frac{1}{v_s.c_I.c_{III s}} \tag{3.29}$$

Figure 3.9 shows the more simplified structure of figure 3.8 with a compensation for the winding ratio. With the help of this fundamental theory of the origin of the air-gap flux due to rotor and stator current distributions along the air-gap circumference, we are now able to derive a method for the identification of the winding ratio factor K.

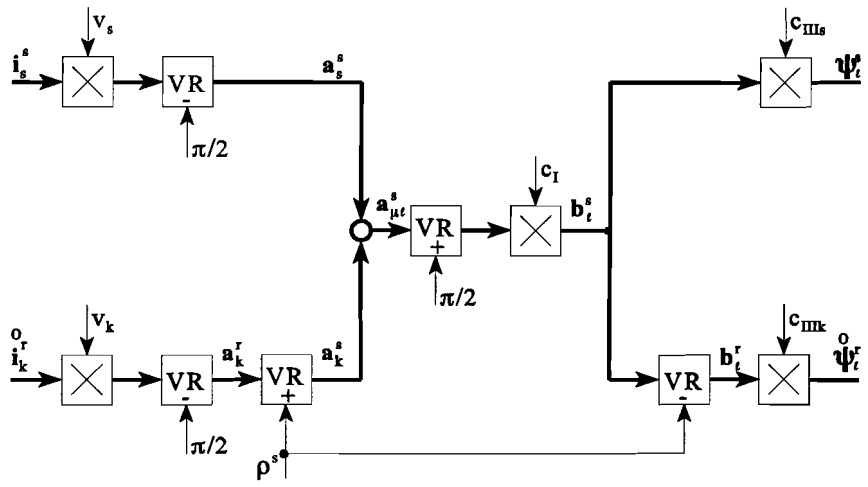

Figure 3.7: Structure diagram of the origin of the air-gap flux.

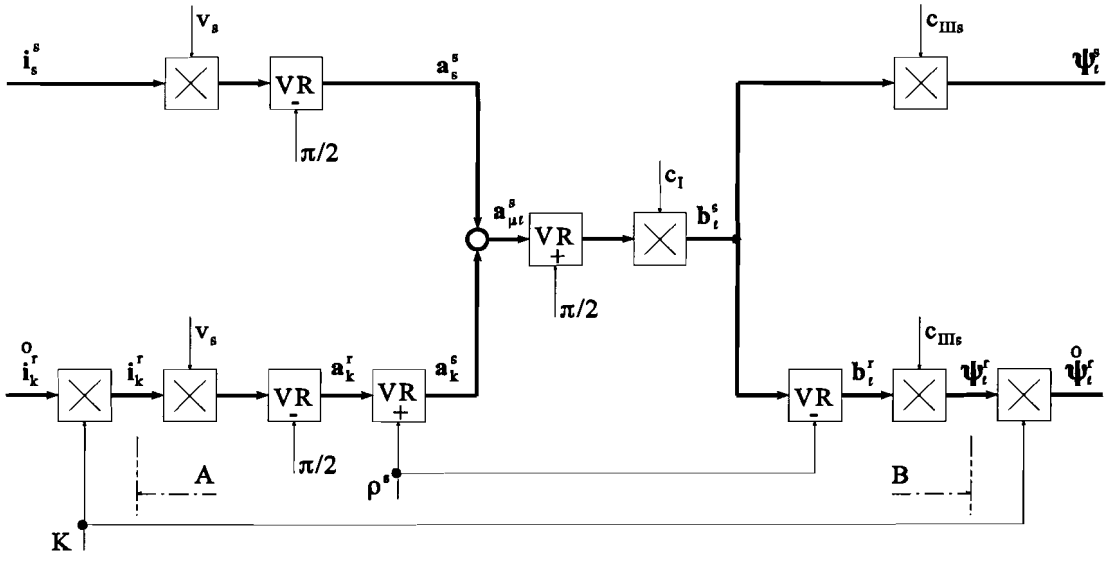

Figure 3.8: Structure diagram of the origin of the air-gap flux with the help of the winding ratio factor K.

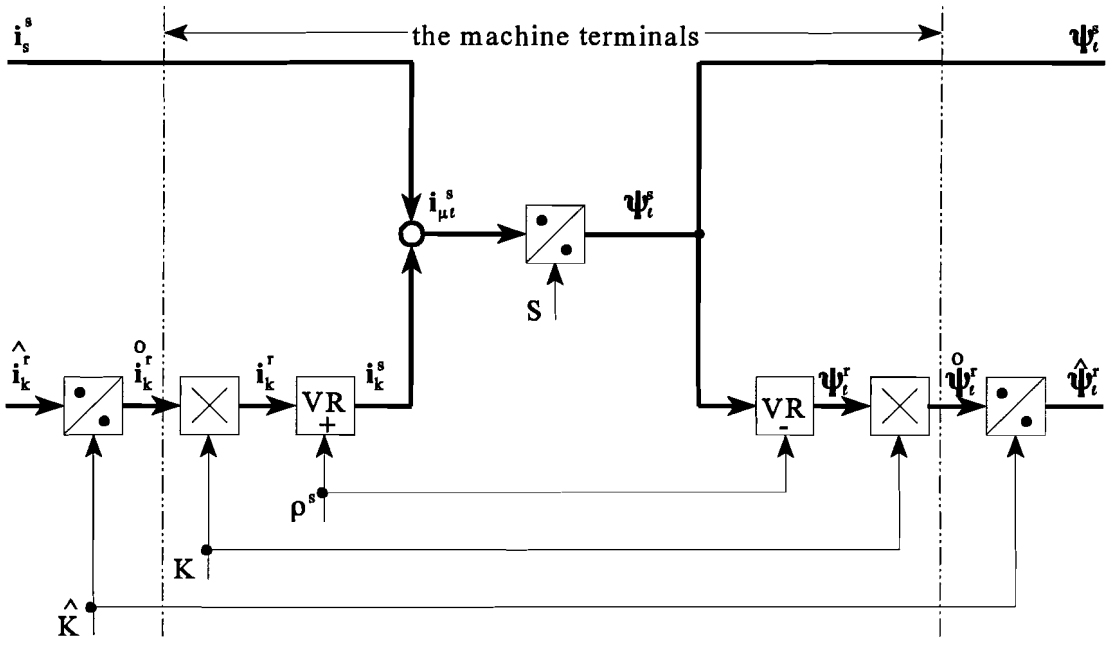

Figure 3.9: A simplified structure diagram of the origin of the air-gap flux with a compensation for the winding ratio factor K.

During the K-identification the induction machine will not be applied as a machine (i.e. $m_{el} = 0$), but as a sort of flux transformer. This implies that we have to ensure ourselves that one side of the machine is current free (i.e. open rotor or stator). The factor K can be found with the help of two measurements (see figure 3.9):

- First the stator will be supplied with a certain current, which will create a specific flux:

$$i_s = i^* \tag{3.30}$$

- After that the rotor will be supplied with the same current provided with a compensation for the winding ratio factor K:

$$\overset{o}{i}_k = \frac{1}{\hat{K}} . \hat{i}_k = \frac{1}{\hat{K}} . i^* \tag{3.31}$$

These measurements will be indicated by the indexes 1 (stator supplied) and 2 (rotor supplied). When during the two measurements equal magnetizing currents arise, the identification is finished. Unfortunately we are not able to measure the magnetizing current directly from the terminals of the machine. However we are able to measure the air-gap flux with the help of the U/I-model. This model estimates (after compensation of the ohmic voltage drop) the stator or rotor flux:

$$\underline{\psi}_s^s = \underline{\psi}_\ell^s + \ell_{\sigma s}.\underline{i}_s^s \tag{3.32}$$

$$\underline{\psi}_k^r = \underline{\psi}_\ell^r + \ell_{\sigma k}.\underline{i}_k^r \tag{3.33}$$

On the condition that i_s or i_k equals zero during the measurement, we can directly measure the air-gap flux with the help of the U/I-model. Also the compensation for the ohmic voltage drop is not needed, because the current in the involved windings equals zero during the measurements.

The only possibility to force the rotor or stator current to zero is the application of a so-called "cross measurement". This means, that we will observe the air-gap flux from the rotor terminals during the first measurement and during the second measurement we will observe the flux from the stator.

First we will supply the stator with a certain current, see equation 3.30. This will result in the following equations (see figure 3.9):

$$\underline{i}_{\mu\ell 1}^s = \underline{i}^* \tag{3.34}$$

$$\underline{\psi}_{\ell 1}^r = \frac{1}{S_1}.R(-\rho^s).\underline{i}_{\mu\ell 1}^s \tag{3.35}$$

$$\hat{\underline{\psi}}_{\ell 1}^r = \frac{K}{\hat{K}}.\underline{\psi}_{\ell 1}^r \tag{3.36}$$

Supplying the rotor with the same, but compensated current (see equation 3.31):

$$\underline{i}_{\mu\ell 2}^s = \frac{K}{\hat{K}}.R(\rho^s).\underline{i}^* \tag{3.37}$$

, we will observe the following air-gap flux from the terminals of the stator:

$$\underline{\psi}_{\ell 2}^s = \frac{1}{S_2}.\underline{i}_{\mu\ell 2}^s \tag{3.38}$$

The equations 3.34 - 3.38 are also valid for the lengths of the vectors, so it is allowed to replace the vectors with their lengths. This will finally result in:

$$\hat{\psi}_{\ell 1} = \frac{K}{\hat{K}}.\frac{1}{S_1}.i^* \tag{3.39}$$

for the first measurement and the second measurement yields:

$$\hat{\psi}_{r2} = \frac{1}{S_2} \cdot \frac{K}{\hat{K}} \cdot i^* \tag{3.40}$$

At first sight one could conclude that the flux of the first measurement equals the flux of the second measurement independent of the factor $K/\hat{K}$. However, this is only the case during linearity:

$$S_1 = S_2 = S_0 \tag{3.41}$$

and this will result in:

$$\hat{\psi}_{r2} = \hat{\psi}_{r1} \tag{3.42}$$

independent of the factor $K/\hat{K}$. Consequently an identification of the winding ratio factor K is not possible during the linear case. Figure 3.10a shows the magnetizing curve during linearity and figure 3.10b shows the independency of the factor $K/\hat{K}$. ψ_{r1} indicates the magnitude of the flux in the case $\hat{K} = K$.

The saturated range gives us an opportunity to identify the factor K. Figure 3.10c shows the magnetizing curve during saturation. In figure 3.10d is shown the measured air-gap flux as a function of the factor $K/\hat{K}$. We notice that the first air-gap flux acts totally linear, because its magnetizing current remains constant. However this is not the case with the second air-gap flux. At this moment the factor $K/\hat{K}$ changes also the magnetizing current, resulting in a non-linear function for the air-gap flux during saturation. Only for the case:

$$\frac{K}{\hat{K}} = 1 \tag{3.43}$$

the two air-gap fluxes will equal each other. So far, we theoretically showed the identification of the winding ratio factor K. However this identification method will be extended, in such a way that we are able to identify this factor without any iteration. The problem of the previous theory is that the identification factor $\hat{K}$ is present during the two measurements. Figure 3.11 shows the K-identification method in practice. During the first measurement (switch in state 1) the air-gap flux from the rotor will be stored in $\hat{\psi}^*_{r1}$. Just during the second measurement (switch in state 2) we will introduce the identification factor $\hat{K}$. When (during saturation) the two air-gap fluxes equal each other the identification is finished.

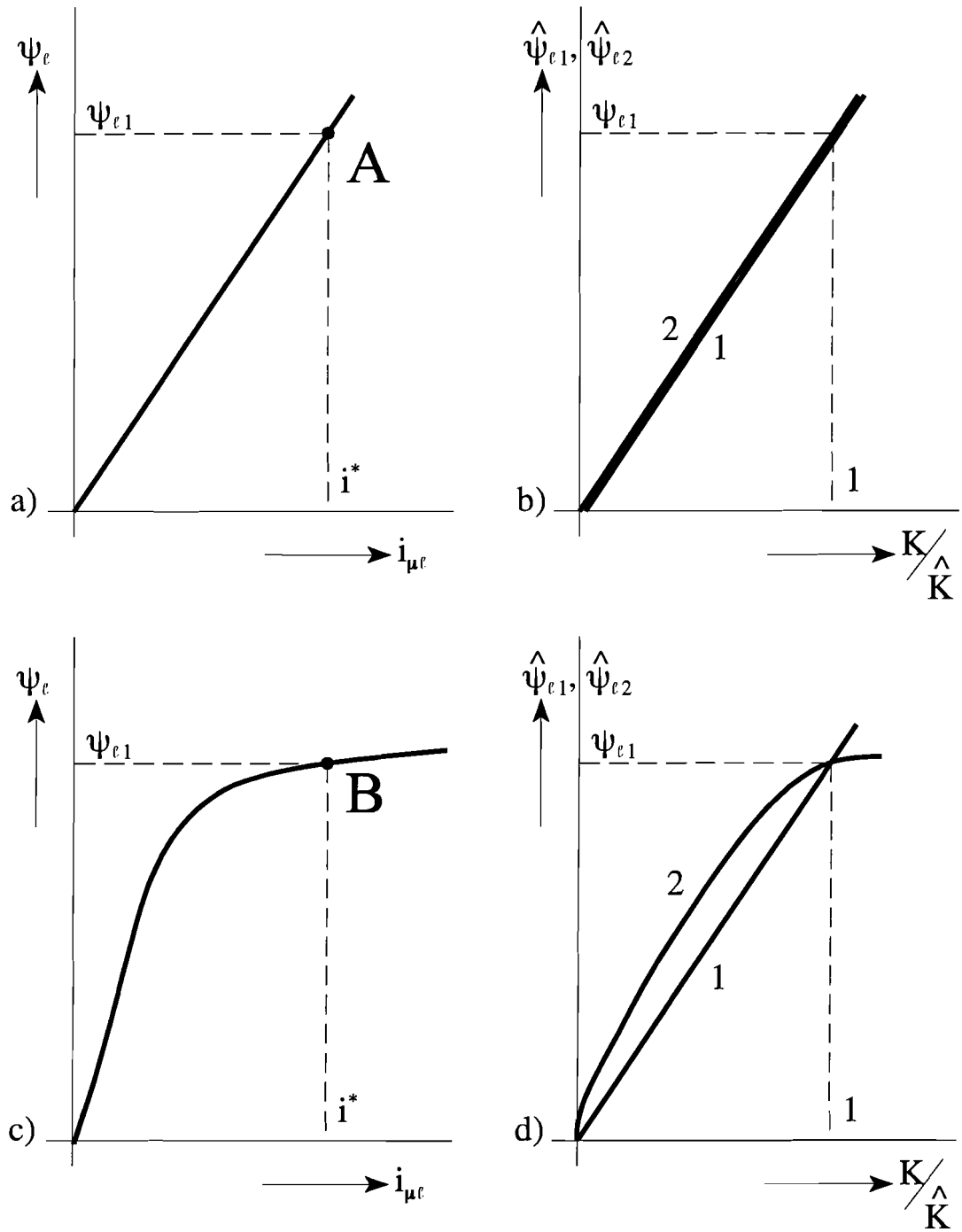

Figure 3.10: Magnetisation curves and the relation of the air-gap fluxes with respect to the factor $K/\hat{K}$:
- a) magnetisation curve during linearity.
- b) relation of the fluxes with respect to the factor $K/\hat{K}$ during linearity.
- c) magnetisation curve during saturation.
- d) relation of the fluxes with respect to the factor $K/\hat{K}$ during saturation.

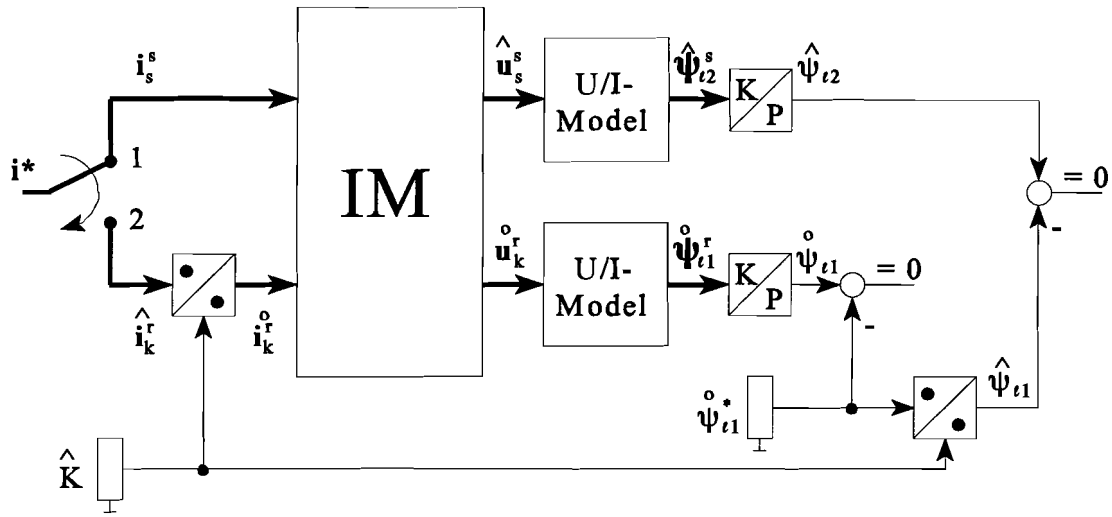

Figure 3.11: The identification of the winding ratio factor in practise.

An issue which is not treated yet, is the method of current supply we will apply. Because we will observe the air-gap flux with the help of the rotor or stator windings, we have to take care for alternating flux seen from the involved windings. There are three possibilities to fulfil this demand:

- By supplying the windings with an alternating current source with a certain frequency at rotor standstill.
- By supplying the windings with a direct current source and the rotor driven by an external speed control with a DC-machine.
- By supplying the windings with an alternating current source with a certain frequency (e.g. the frequency of the mains) and the rotor driven by an external speed control with a DC-machine.

We finally decided to apply a direct current source together with a speed control. Since this identification method only functions during saturation, we have to supply the machine with a current larger than the rated magnetizing current. Normally about 30 percent of the rated machine current is used for the magnetisation, so we have to take care for a current:

$$i^* > i_{\mu fN} = 0.3 \text{ PU} \tag{3.44}$$

The frequency of the alternating air-gap flux is determined by the speed control of the DC-machine. A low frequency could result in an error, since we estimate the air-gap flux with the help of the U/I-model. At high frequency we will have to deal with (more) iron losses due to hysteresis and eddy currents effects. The hysteresis losses in a machine are linear with the frequency, the losses due to eddy currents vary even quadratically. So the choice of the frequency will be a compromise between the behaviour of the U/I-model and the iron losses in the machine.

3.3.2 Identification of the real rotor angle.

The next parameter we have to identify, is the compensation for the deviation in the measured rotor angle. As presented in subsection 3.2 this deviation can originate due to the wrong mounting of the resolver on the shaft. First we will present an identification technique, which we will indicate as a "coarse identification". Although we have to mention, that this name is a little misleading: when we would be able to create an ideal no-load condition (i.e. $m_{el} = 0$), this identification would suffice. Managing an ideal no-load situation is very difficult in practice, so we need to introduce a "fine identification" method. This method makes use of iteration; consequently it is only valid for a starting angle with a small deviation (that is the reason for introducing first the "coarse identification").

During the coarse identification, the induction machine will not be applied as an asynchronous machine, but as a synchronous machine. This means that the rotor will not be shorted, but supplied with a direct current. When we manage to create an ideal no-load situation with an external DC-machine eliminating the losses due to friction (bearing and windage losses), both vectors $\mathbf{i}_s$ and $\mathbf{i}_k$ are only used for magnetisation of the iron. So equation 3.2 equals

$$\mathbf{i}_{\mu t} = \mathbf{i}_s + \mathbf{i}_k \tag{3.45}$$

in case of an ideal no-load condition. Figure 3.12a presents the vector diagram for this situation.

However due to the deviation δ in the measured rotor angle we will observe a wrong vector diagram in model C (see figure 3.12b). With a correct adjustment of the correction angle χ the vector diagram in model C will equal the diagram of the ideal structure. As mentioned before it might be hard to create an ideal no-load condition. Therefore we will introduce an accurate identification method.

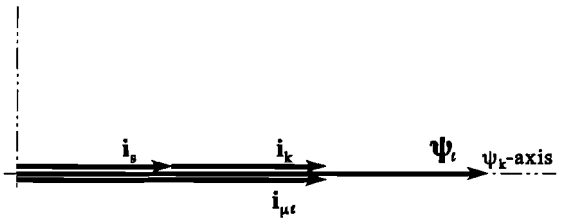

Figure 3.12a: Vector diagram of the induction machine applied as a synchronous machine during the no-load condition.

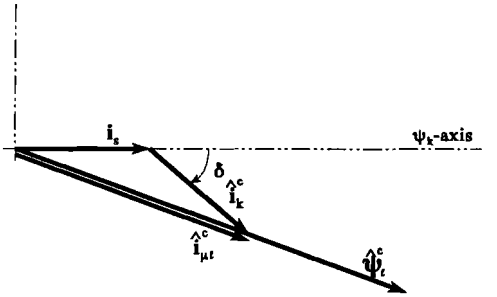

Figure 3.12b: Vector diagram of model C during the no-load condition with a certain deviation in the rotor angle.

The induction machine will be applied in two states during the "fine identification". The first state stands for motor operation (i.e. mechanical energy is powered to the load) and the second state indicates a generator operation (i.e. mechanical energy is absorbed from the load).

First we will examine the steady-state vector diagram of the machine during motor operation. The "fictitious" magnetizing current vector $\mathbf{i}_{\mu k}$ consists of the addition of the stator and rotor current (see also equations 3.6 and 3.7):

$$\mathbf{i}^s_{\mu k} = \mathbf{i}^s_s + [1+S(\psi_r).\ell_{\sigma k}].\mathbf{i}^s_k \qquad \textbf{(3.46)}$$

Further we will introduce a new variable z:

$$z = 1+S(\psi_r).\ell_{\sigma k} \qquad \textbf{(3.47)}$$

From which we can simplify equation 3.46:

$$\mathbf{i}^s_{\mu k} = \mathbf{i}^s_s + z.\mathbf{i}^s_k \qquad \textbf{(3.48)}$$

Figure 3.13a shows the steady-state vector diagram of the induction machine with the help of equation 3.48. We notice that the rotor current is perpendicular to the rotor flux (and thus the "fictitious" magnetizing current $\mathbf{i}_{\mu k}$). The following equations prove the perpendicularity in the induction machine during the steady state(see also equations 2.34 and 2.35):

$$-i^b_k = \frac{1}{r_k}.\dot{\psi}_k \qquad \textbf{(3.49)}$$

and

$$-i^w_k = \frac{1}{r_k}.\psi_k.\dot{\varphi}^r_k \qquad \textbf{(3.50)}$$

During steady state the derivative of the rotor flux equals zero:

$$\dot{\psi}_k = 0 \qquad \textbf{(3.51)}$$

resulting in:

$$i^b_k = 0 \qquad \textbf{(3.52)}$$

Together with equation 3.50 this proves the perpendicularity between the vectors $\mathbf{i}_k$ and $\boldsymbol{\psi}_k$.

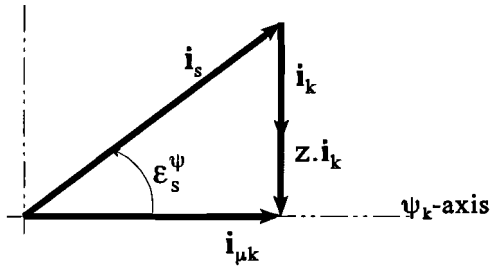

Figure 3.13a: Current vector diagram of the machine during steady state.

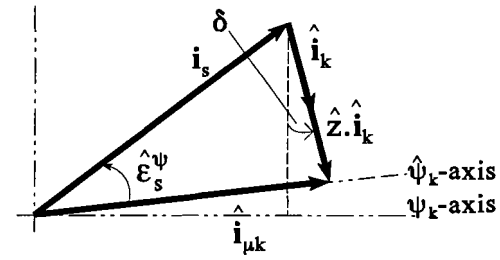

Figure 3.13b: Current vector diagram of model C during steady state.

However the perpendicularity is not necessarily available in model C due to the deviation in the rotor angle (see figure 3.13b). By changing the $\hat{z}$-factor we can take care that the rotor current vector is perpendicular to the **estimated** rotor flux vector (see figure 3.14).

Next we have to examine the situation of figure 3.13a (no error angle available) and the situation (with a certain $\hat{z}$ which ensures perpendicularity with respect to the **estimated** rotor flux axis) in model C with a certain error angle δ (see figure 3.14, with $\hat{z} = \hat{z}_1$). The goniometric relations between these two figures give us:

$$\frac{\hat{z}}{z} = \frac{i_s.\sin(\varepsilon_s^\psi - \delta)}{i_s.\sin\varepsilon_s^\psi} \qquad (3.53)$$

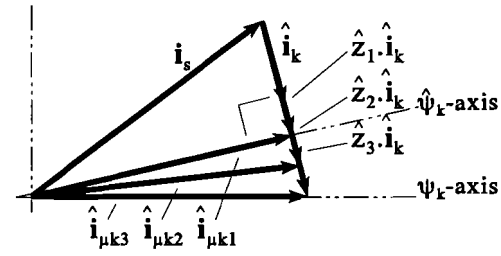

Figure 3.14: Current vector diagram of model C with different $\hat{z}$-factors.

We can rewrite this equation with the help of some goniometry:

$$\frac{\hat{z}}{z} = \frac{\sin\varepsilon_s^\psi.\cos\delta - \cos\varepsilon_s^\psi.\sin\delta}{\sin\varepsilon_s^\psi} \qquad (3.54)$$

However, due to the help of the coarse identification of χ at the beginning of this subsection, the remaining error angle is very small:

$$|\delta| < 3° \qquad (3.55)$$

With this condition we can approximate the goniometric functions sine and cosine with:

$$\cos\delta \approx 1$$
$$\sin\delta \approx \delta \qquad (3.56)$$

From which we can simplify equation 3.54 to:

$$\frac{\hat{z}}{z} \approx 1 - \frac{1}{\tan\varepsilon_s^\psi}.\delta \qquad (3.57)$$

In the situation $\delta=0$, the estimation $\hat{z}$ equals z. However during the identification of the error angle we have to apply the machine in two states: motor operation (index m) and a "symmetrical" generator operation (index g):

$$\begin{aligned} i_{sg} &= i_{sm} \\ \varepsilon_{sg}^{\psi} &= -\varepsilon_{sm}^{\psi} \end{aligned} \tag{3.58}$$

In these two states same magnetizing currents $i_{\mu k}$ and $i_{\mu \ell}$ originate and therefore the rotor leakage inductance and the S-value equal each other:

$$\begin{aligned} S_g &= S_m \\ \ell_{\sigma k_g} &= \ell_{\sigma k_m} \end{aligned} \tag{3.59}$$

and (see equation 3.47)

$$z_g = z_m \tag{3.60}$$

With perpendicularity in the ideal situation ($\delta=0$) one yields:

$$\hat{z}_g = \hat{z}_m \tag{3.61}$$

However this is not the case in model C (see figure 3.15) where there is still a remaining error angle δ, hence:

$$\hat{z}_g \neq \hat{z}_m \tag{3.62}$$

With the help of equation 3.57 the following equations result:

$$\frac{\hat{z}_m}{z} \approx 1 - \frac{1}{\tan \varepsilon_{sm}^{\psi}} . \delta \tag{3.63}$$

and

$$\frac{\hat{z}_g}{z} \approx 1 - \frac{1}{\tan \varepsilon_{sg}^{\psi}} . \delta \tag{3.64}$$

Together with equation 3.58 we can finally rewrite these equations into:

$$\frac{\hat{z}_g}{\hat{z}_m} \approx \frac{1 + \frac{1}{\tan \varepsilon_{sm}^{\psi}} . \delta}{1 - \frac{1}{\tan \varepsilon_{sm}^{\psi}} . \delta} \tag{3.65}$$

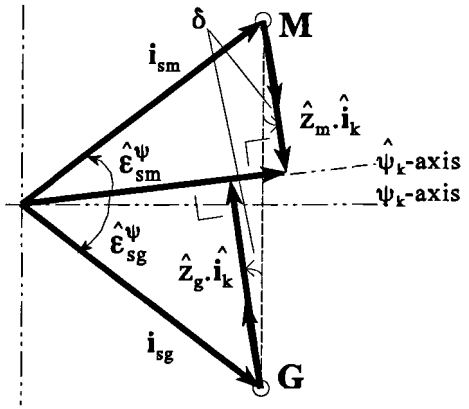

Figure 3.15: Current vector diagram of model C with a certain $\hat{z}$ which ensures perpendicularity in motor or generator operation state.

Next we are able to estimate the error angle from equation 3.65, resulting in:

$$\delta \approx \tan \varepsilon_{sm}^{\psi} . h \tag{3.66}$$

with

$$h = \frac{\frac{\hat{z}_g}{\hat{z}_m} - 1}{\frac{\hat{z}_g}{\hat{z}_m} + 1} \tag{3.67}$$

Creating a symmetrical motor and generator operation is not possible yet, because the **real** load angle ε_s^{ψ} is not available. The only possibility is measuring the load angle of model C influenced with a small deviation δ (see figure 3.16).

$$\varepsilon_{sm}^{\psi} = \hat{\varepsilon}_{sm}^{\psi} + \delta \tag{3.68}$$

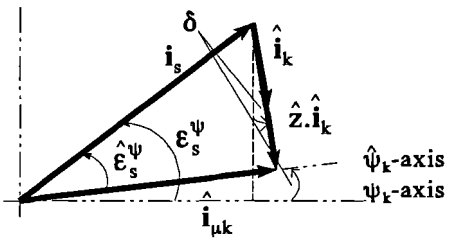

Figure 3.16: The difference between the real load angle and its estimation.

The tangent of this angle can be rewritten into:

$$\tan \varepsilon_{sm}^{\psi} = \frac{\tan \hat{\varepsilon}_{sm}^{\psi} + \tan \delta}{1 - \tan \hat{\varepsilon}_{sm}^{\psi} . \tan \delta} \tag{3.69}$$

Due to the smallness of δ it is allowed to apply the following approximation:

$$\frac{1}{1 - \tan \hat{\varepsilon}_{sm}^{\psi} . \tan \delta} \approx 1 + \tan \hat{\varepsilon}_{sm}^{\psi} . \tan \delta \tag{3.70}$$

and after neglecting the quadratic term of $\tan\delta$ we will find:

$$\tan \varepsilon_{sm}^{\psi} \approx \tan \hat{\varepsilon}_{sm}^{\psi} + (1 + \tan^2 \hat{\varepsilon}_{sm}^{\psi}) . \tan \delta \approx \tan \hat{\varepsilon}_{sm}^{\psi} + (1 + \tan^2 \hat{\varepsilon}_{sm}^{\psi}) . \delta \tag{3.71}$$

Together with equations 3.66 and 3.67 this will result in:

$$\delta = (m + (1 + m^2) . \delta) . h \tag{3.72}$$

with

$$m = \tan \hat{\varepsilon}_{sm}^{\psi} = \frac{\hat{i}_{sm}^{w}}{\hat{i}_{sm}^{b}} \tag{3.73}$$

For the error angle one finally gets:

$$\delta \approx \frac{m . h}{1 - (1 + m^2) . h} \tag{3.74}$$

Applying the induction machine in two symmetrical states will offer us the opportunity to correct the rotor angle $\hat{\hat{\chi}}$ to $\hat{\chi}$ (on the condition that $\delta \approx 0$):

$$\hat{\chi} = \hat{\hat{\chi}} - \delta \tag{3.75}$$

We recommend to execute this accurate identification method a few times, because this will finally ensure a good identification and in the case:

$$\hat{z}_g = \hat{z}_m \tag{3.76}$$

the identification is successful.

3.3.3 Identification of the inductances.

The only remaining parameter identification of model C is the identification of the main and leakage inductances. These parameters are responsible for the unknown parameter z (see equation 3.48) and, in spite of the accurate identification of the rotor angle, perpendicularity is still not achieved in model C during the loaded condition, see figure 3.17a.

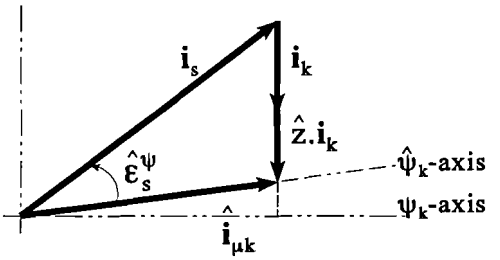

Figure 3.17a: Current vector diagram of model C during steady state.

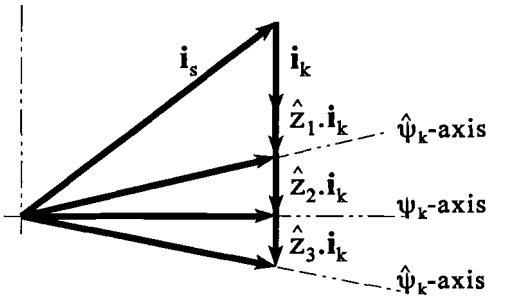

Figure 3.17b: Current vector diagram of model C with different $\hat{z}$-factors.

However by changing the $\hat{z}$-factor we can again ensure perpendicularity between rotor flux and rotor current (analogous to the previous subsection), see figure 3.17b. At this moment we identify the **real** rotor flux-axis, which means also the availability of the field oriented coordinates of the stator current:

$$\mathbf{i}_s^{\psi} = R(-\varphi_k^s).\mathbf{i}_s^s \tag{3.77}$$

As mentioned in the introduction of section 3.3 we will be assisted by the U/I-model (see figure 3.18). This model estimates the stator flux from stator voltages and currents, but first we have to identify the stator resistance. The most simple method is an identification at frequency zero: supplying the stator with direct current implies a non-alternating stator flux; thus, at frequency zero the stator equation (see equation 3.1) can be reduced to:

$$\mathbf{u}_s^s = r_s.\mathbf{i}_s^s \tag{3.78}$$

So we have to change the estimated value of the stator resistance until the ohmic voltage drop equals the stator voltage. For the identification of the S2-factor we refer to Burgt[12]. However this factor will not harm the result, since $\hat{\psi}_s$ equals zero during steady state.

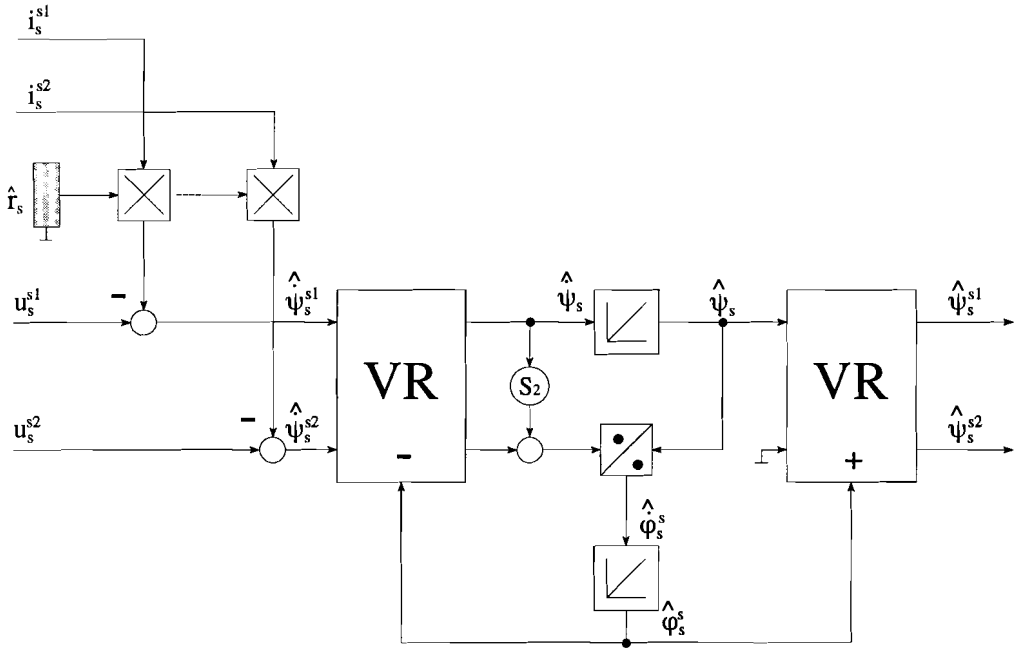

Figure 3.18: The U/I-model as presented in Burgt[12].

The U/I-model presents the stator flux in the stator coordinate system, but with the help of the meanwhile identified **real** flux-axis we can easily transform these coordinates into their field oriented coordinates:

$$\boldsymbol{\psi}_s^{\psi} = R(-\varphi_k^s).\boldsymbol{\psi}_s^s \tag{3.79}$$

So besides the field oriented stator current coordinates, the field oriented coordinates of the stator flux are also available:

$$\hat{i}_s^b = i_s^b \tag{3.80}$$

$$\hat{i}_s^w = i_s^w \tag{3.81}$$

$$\hat{\psi}_s^b = \psi_s^b \tag{3.82}$$

$$\hat{\psi}_s^w = \psi_s^w \tag{3.83}$$

and further we identified the factor which takes care for perpendicularity (see figure 3.17b, with: $\hat{z} = \hat{z}_2$)

$$\hat{z} = z \tag{3.84}$$

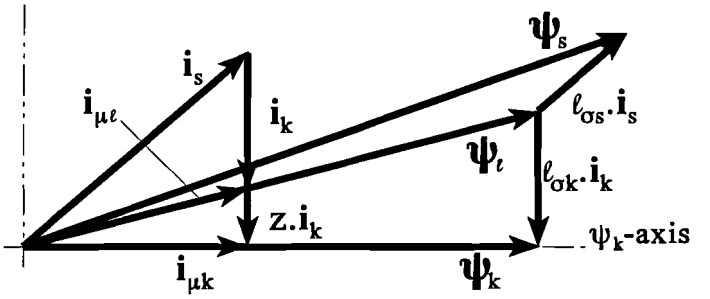

Figure 3.19a: Extensive current and flux vector diagram of the machine during steady state.

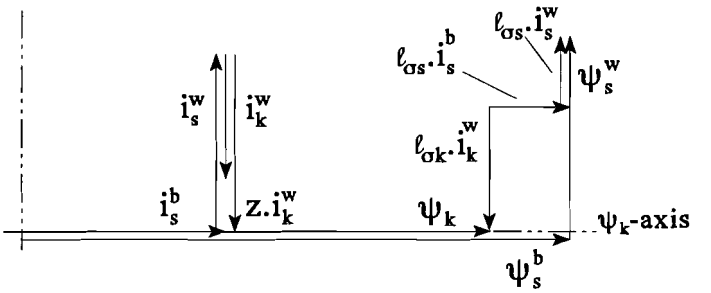

Figure 3.19b: The coordinate diagram of figure 3.19a.

Figure 3.19a shows the extensive current and flux vector diagram of the machine during steady state with a certain load. With the help of this figure we can easily find the relations between the already identified field oriented stator quantities (current and flux) and the inductances. Figure 3.19b presents these relations, from which we can derive the following equations:

$$\psi_s^b = \psi_k + \ell_{\sigma s}.i_s^b \tag{3.85}$$

$$\psi_s^w = \ell_{\sigma s}.i_s^w - \ell_{\sigma k}.i_k^w \tag{3.86}$$

$$i_s^w = -z.i_k^w \tag{3.87}$$

During steady state the following equation is valid:

$$\psi_k = \frac{1}{S}.i_s^b \tag{3.88}$$

Next we will introduce the "fictitious" inductances ℓ_b and ℓ_w :

$$\ell_b = \frac{\psi_s^b}{i_s^b} \tag{3.89}$$

and

$$\ell_w = \frac{\psi_s^w}{i_s^w} \tag{3.90}$$

These two "fictitious" inductances are available in model C (the perpendicularity requirement is fulfilled) by one measurement and they give us information about the relation between the main and leakage inductances:

$$\ell_b = \frac{1}{S} + \ell_{\sigma s} \tag{3.91}$$

$$\ell_w = \ell_{\sigma s} + \ell_{\sigma k} \cdot \frac{1}{1 + S.\ell_{\sigma k}} \tag{3.92}$$

Furthermore we identified the z-factor, which takes care for perpendicularity between rotor flux and current (see equation 3.47):

$$z = 1 + S.\ell_{\sigma k} \tag{3.93}$$

From these 3 equations we can finally derive the formulae of the inductances:

$$\ell_{\sigma s} = \ell_w - (z-1).(\ell_b - \ell_w) \tag{3.94}$$

,

$$\ell_{\sigma k} = \frac{(\ell_b - \ell_{\sigma s}).(\ell_w - \ell_{\sigma s})}{\ell_b - \ell_w} \tag{3.95}$$

and

$$S = \frac{1}{\ell_b - \ell_{\sigma s}} \tag{3.96}$$

The reciprocal value S of the main inductance depends on the air-gap flux during saturation, so we have now to construct the air-gap flux (see also figure 3.19a and b):

$$\psi_\ell^b = \psi_s^b - \ell_{\sigma s}.i_s^b \tag{3.97}$$

,

$$\psi_\ell^w = \psi_s^w - \ell_{\sigma s}.i_s^w \tag{3.98}$$

and the length of the air-gap flux:

$$\psi_\ell = \sqrt{(\psi_\ell^b)^2 + (\psi_\ell^w)^2} \tag{3.99}$$

In chapter 2 we already made a remark, that saturation affects not only the main inductance but also the leakage inductances. This identification method will estimate the inductances of the machine for every load, except the no-load (rotor current equals zero at that moment). This means that we can show the course of the main inductance as well as the leakage inductances during saturation. However the course of the leakage inductances will depend on more variables than the air-gap flux. Furthermore the course will not only depend on the magnitude of fluxes, but also on the layout of the windings inside the machine. So we have to be careful to compare the course of the measured saturable leakage inductances with for instance the course of the leakage inductances of a squirrel cage induction machine, because the rotor winding layout of this machine is rather different in comparison with that of a slip ring induction machine.

CHAPTER 4

EXPERIMENTAL RESULTS

4.1 Introduction.

In the beginning variable speed drives were controlled by analog electronics. In spite of the temperature dependency (analog systems have to warm themselves up before functioning well) these analog controllers were respected in the industry. However since the invention of Field Oriented Control and thus the application of AC-machines in high performance drive systems on a large scale, control strategies have been become more complicated. Therefore the interest of the researchers in the Digital Signal Processor systems was not surprising. A DSP-system offers the possibility to control the machine with a high performance (temperature-independent). Furthermore, a DSP-system is more flexible in comparison with analog electronics (for instance: changes are made in no time; a soldering-bolt is not needed). Nowadays modern control of AC-machines basically consists of a DSP-system and power electronics and is often indicated with the term: "*State of the Art*".

As usual during a scientific research we start with simulation. The machine structure is implemented on the DSP-system[1]. We choose for a simulation on the DSP-system, because this will approach the reality better and further, it makes the next step to practice easier. After that we will simulate the identification techniques, presented in section 3.3. These simulations show us the importance of some parameters, for instance: a small deviation in the rotor angle or winding ratio factor can result in large errors during the final identification of the inductances.

Due to simulation results some theory may be adapted or improved. When the simulation has sufficed we make the step to practice. In general, this means we will replace the simulated machine with the **real** machine.

Although the simulation results were satisfying, in practice we can again encounter some difficulties. At that moment we have to reconsider the theory. By adapting or improving the theory or the experimental setup in our laboratory we will finally get satisfying experimental results. This way from theory to practice is shown in figure 4.1.

[1]See appendix A for a detailed description of the DSP-system.

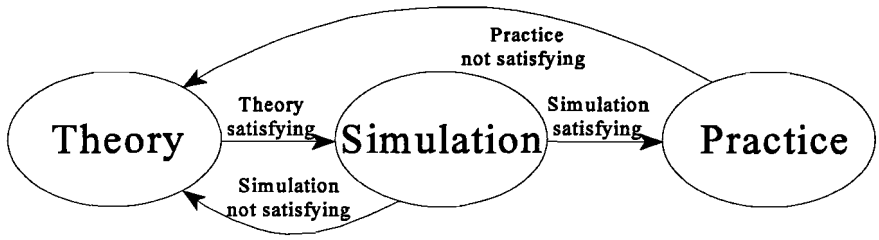

Figure 4.1: The way from theory to practice during a scientific analysis.

4.2 Simulation of the machine structure affected with saturation.

First the machine structure affected with saturation has to be implemented on the DSP-system. This structure is shown in figure 2.16. The difference between this structure and the already available linear structure (see figure 2.13) is the saturable value S. This value depends on a still unknown function of the air-gap flux. So first the air-gap flux has to be constructed. After that we have to approximate the $S_z(\psi_\ell)$ saturation function. Two possibilities are available:

- Using a spreadsheet table and a low order interpolation between two neighbour points.
- Function approximation with the help of the Lagrange[2] polynomial interpolation method.

We decided to apply the Lagrange polynomial approximation:

$$S_z(\psi_\ell) \approx a_0 + a_1.(\psi_\ell - \psi_{\ell sat})^1 + a_2.(\psi_\ell - \psi_{\ell sat})^2 + ... + a_n.(\psi_\ell - \psi_{\ell sat})^n \qquad (4.1)$$

wherein $\psi_{\ell\ sat}$ indicates the border between linearity and saturation. This method has a number of advantages in comparison with a spreadsheet table. From physical consideration we know that the saturation function is a smooth and an increasing function. This means we have to constrain that a_0 and a_1 equal zero (this ensures a smooth transition from linearity to saturation) and further all the other coefficients have to be positive (this ensures that the function only increases). In Matlab, a program has been written which enables us to find the right approximation. With the help of the "Least Square Approximation Method" we are even able to force some undesired (negative) coefficients to zero (see figure 4.2).

[2]Joseph Louis Lagrange (1736-1813): He was an excellent French mathematician and already at an age of 16 years he was appointed to professor in mathematics at the University of Turin. He was the founder of the nowadays indispensable metric system (Système International). Further he studied the differential equations and invented the polynomial interpolation method (source: Asselt[1]).

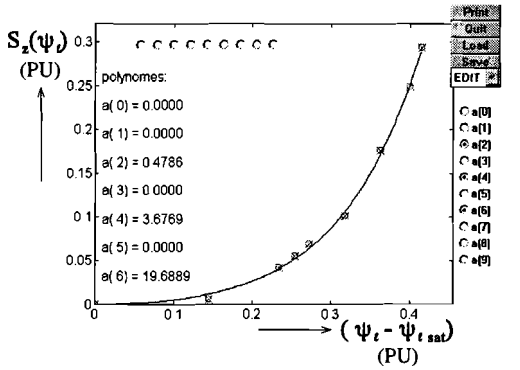

Figure 4.2: Function approximation with the help of the Lagrange polynomial interpolation.

A function approximation method is now available, so now we are able to implement the machine structure on the DSP-system. The parameters of this structure are obtained from a previous identification[3]. At this moment we can control the machine with the stator current vector (scalar control), however showing the influence of the saturation effect is easier with the help of a Field Oriented Control (during the simulation we don't need a flux observer, because we can directly obtain the flux vector from the machine structure). First we will apply a linear Field Oriented Control (see figure 2.18 with $\hat{S}_z(\psi_\ell) = 0$). The steady-state results are shown in figure 4.3. We see that there is a slight deviation between the real and the desired torque. However the rotor flux deviates a lot from the desired value, we do not get what we want.

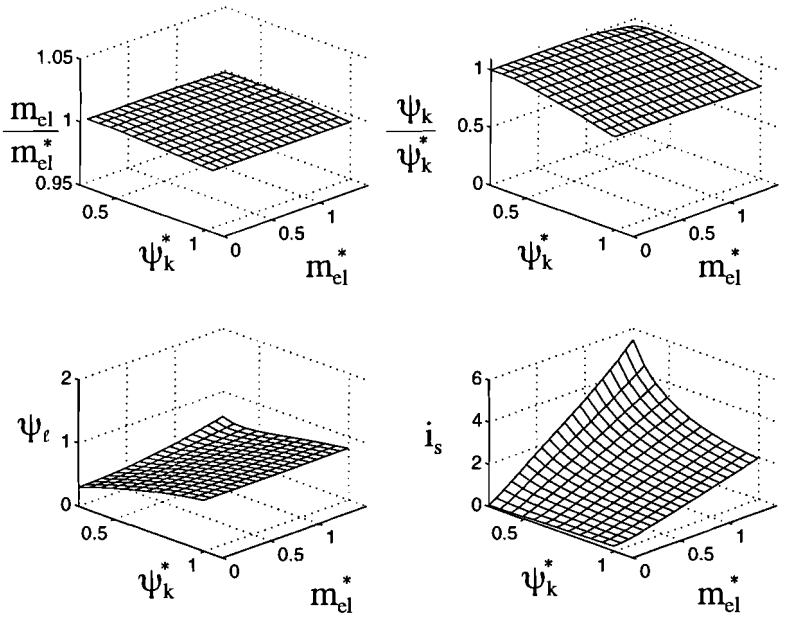

Figure 4.3: Linear Field Oriented Control applied to the machine structure affected with saturation.

[3]See appendix B for the values of the applied parameters during the simulation.

After that we will apply a Field Oriented Control with a compensation for the saturation effect (see figure 2.18 with $\widehat{S}_z(\psi_\ell) \neq 0$). Figure 4.4 presents the steady-state results in case of non-linear Field Oriented Control. We see that this Field Oriented Control is functioning well: we get what we want. When we look at the stator current plot, we see a small increase of the current at the no-load situation in comparison with figure 4.3. During no-load all the current is used for the magnetisation of the iron, thus this explains the linear and non-linear course of the current at no-load with a linear and a non-linear Field Oriented Control, respectively. Further we see an increase of the air-gap flux at high desired rotor flux in comparison with figure 4.3. This is caused by the compensation for the saturation effect.

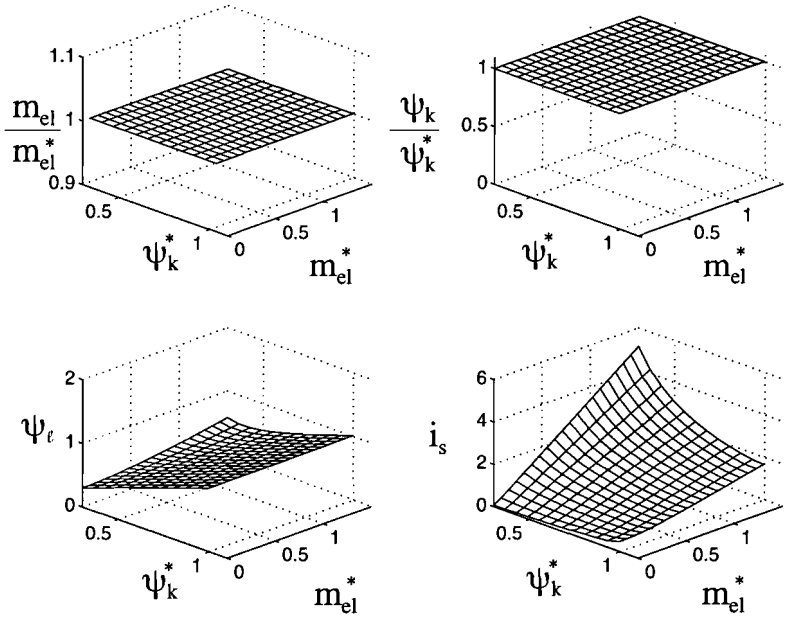

Figure 4.4: Non-linear Field Oriented Control applied to the machine structure affected with saturation.

Figure 4.5 and 4.6 show the step response in the rotor flux with a linear and a non-linear Field Oriented Control (with $m_{el} = 0.5$ pu), respectively. We see again that the command value of the rotor flux is not reached in case of a linear control.

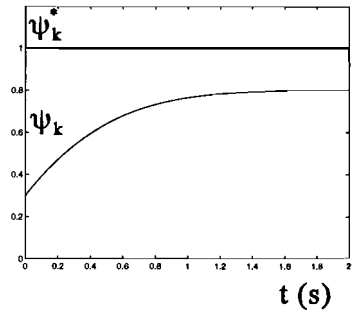

Figure 4.5: Rotor flux (pu) step response with a linear Field Oriented Control.

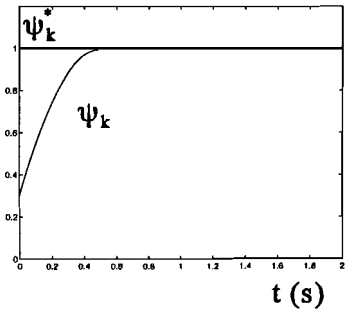

Figure 4.6: Rotor flux (pu) step response with a non-linear Field Oriented Control.

4.3 Simulation of the parameter identification techniques.

In this section we will simulate the parameter identification procedures, presented in section 3.3. These simulation results will give us information about difficulties, which we can expect in practice. For instance: the effect of previous wrong identified parameters in the next identifications; especially the identification of the inductances depends on two previous identified parameters: χ and K.

However, before we can start simulating the identification techniques, first we have to adapt our machine structure. As mentioned in section 3.2, in practice we observe the rotor quantities from the rotor terminals , while all other quantities of our machine structure are observed from the stator terminals. This means we have to adapt the rotor current i_k with a specific winding ratio factor (see also equation 3.10):

$$\overset{o}{i}_k = \frac{1}{K}.i_k \tag{4.2}$$

wherein $\overset{o}{i}_k$ indicates the rotor current of the machine structure seen from the rotor terminals. We arbitrarily choose for the winding ratio factor K:

$$K = 0.833 \tag{4.3}$$

This factor has to be identified. Further, only the field oriented coordinates of the stator and the rotor current are available in the machine structure, while in a **real** machine we measure the above mentioned quantities with respect to stator and rotor axis, respectively:

$$\mathbf{i}_s^s = R(\varphi_k^s).\mathbf{i}_s^\psi \tag{4.4}$$

and

$$\mathbf{i}_k^r = R(\varphi_k^r).\mathbf{i}_k^\psi \tag{4.5}$$

Model C also uses the rotor angle with respect to the stator axis, which we can directly obtain from the machine structure. However, in practice (see also section 3.2) a deviation in the measured rotor position can occur. So, now we will introduce a deviation in the measured rotor angle ρ^s:

$$\overset{o}{\rho}^s = \rho^s - \chi \tag{4.6}$$

We arbitrarily choose for χ:

$$\chi = 2 \text{ rad} \tag{4.7}$$

, which has to be identified. At this moment we can connect model C to the adapted machine structure. For clearness a block diagram of the simulation is shown in figure 4.7.

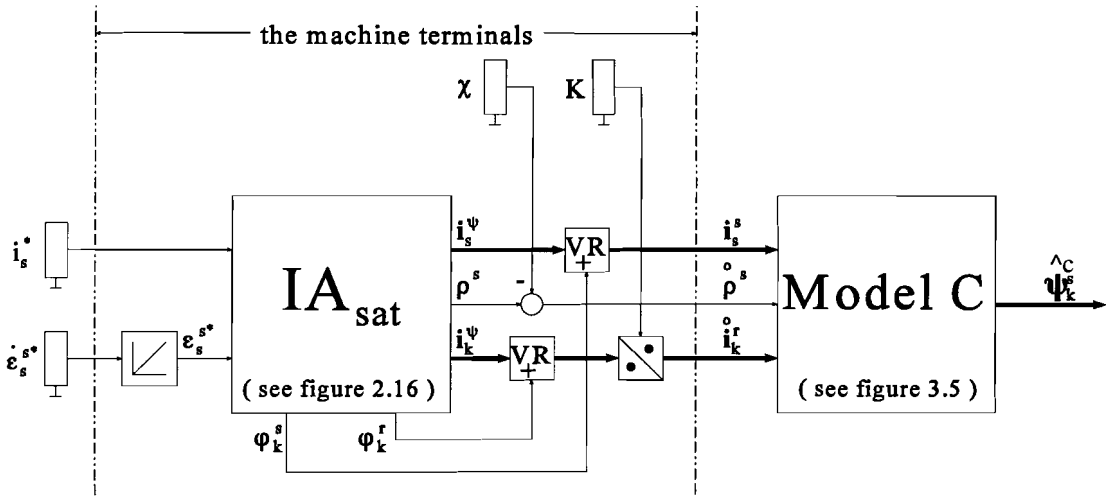

Figure 4.7: Block diagram during the simulation of the parameter identification techniques.

4.3.1 Simulation of the identification of the winding ratio factor K.

As explained in section 3.3.1 we supply first the stator and then the rotor with a specific current. Simulating this identification technique requires a total new machine structure (block diagram); therefore we abandon the simulation of the winding ratio factor K.

4.3.2 Simulation of the identification of the real rotor angle.

First we have to execute the "coarse" identification. During this identification the slip-ring induction machine will be applied as a synchronous machine: the rotor will externally be supplied with a DC current instead of shorted. This implies, that we have to change the machine structure. Figure 4.8 presents the machine structure for the synchronous machine affected with saturation (a short derivation of this structure is shown in appendix D.1). This structure represents a model of a synchronous machine with a damper winding. However, in our case we use the damper winding as the excitation winding; this implies the absence of the damper winding in practice. By enlarging the rotor resistance r_k, we can decrease the effect of the damper winding in our structure. However the value of r_k is limited, because a too large r_k will make the machine structure unstable. Furthermore, the effect of the damper winding is not available during steady state and consequently this will not harm the "coarse" identification.

Most confusing of this synchronous machine structure is the availability of two types of rotor currents (namely the damper winding current and the excitation current), while in practice we only measure one current. In figure 4.8 i_r represents this current. Now we have to connect model C to the machine structure. Figure 4.7 again shows an overview of the simulation, in which IA_{sat} has to be replaced by figure 4.8 and $\mathbf{i}_r^{\psi}$ will replace $\mathbf{i}_k^{\psi}$ as mentioned before.

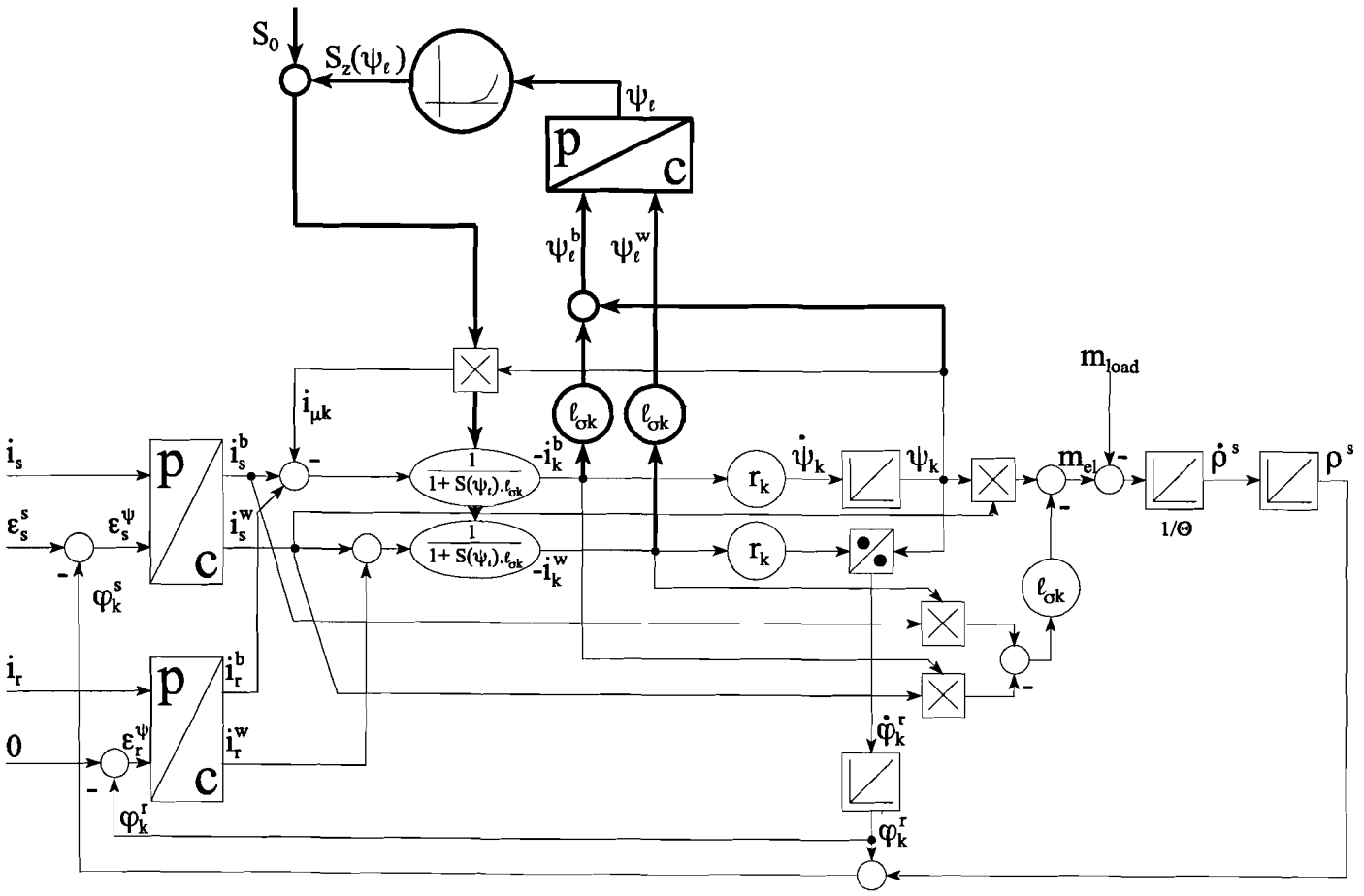

Figure 4.8: The machine structure of the current-fed synchronous machine affected with saturation.

Creating an ideal no-load situation is not difficult during simulation; m_{load} has to equal zero. At no-load both stator and rotor current are used for the magnetisation of the iron, and since $i_{\mu f N} \leq 0.3$ pu (see equation 3.44) we will supply both stator and rotor with approximately 0.15 pu. By changing $\hat{\chi}^c$ we can ensure that $\hat{i}_k^{s^c}$ is oriented parallel to i_s^s. When the second coordinate of the rotor current ($\hat{i}_k^{w^c}$) with respect to the **estimated** rotor flux axis equals zero, the "coarse" identification is finished (see figure 4.9).

As a result of the "coarse" identification we find:

$$\hat{\chi}^c = 2.0432 \tag{4.8}$$

Next we have to execute the "fine" identification. Instead of the identified parameter $\hat{\chi}^c$ of equation 4.8 we start this identification with:

$$\hat{\chi}_1^c = 2.1 \tag{4.9}$$

which implies a deviation of 0.1 rad (= 5.7 °) with respect to the real value. In figure 4.7 the overview of the block diagram used during the simulation of this identification technique is shown. First we will positively load the machine (motor operation) and by enlarging the $\hat{z}$-factor we can ensure perpendicularity between the **estimated** rotor flux and the rotor current; this is fulfilled when the first coordinate ($\hat{i}_k^{b^c}$) with respect to the **estimated** rotor flux axis equals zero (see also figure 4.9). Instead of enlarging the $\hat{z}$-factor we will enlarge the $\hat{K}^c$-factor in model C (see figure 3.5), the relation between these two factors is the winding ratio factor K:

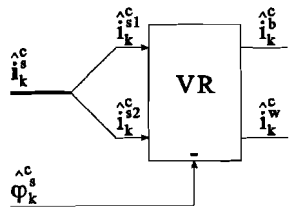

Figure 4.9: The estimated field oriented rotor current coordinates.

$$\hat{K}^c = \hat{z}.K \tag{4.10}$$

After the perpendicularity requirement is fulfilled, we store the estimated field oriented coordinates of the stator current (see figure 4.10) and the $\hat{z}_m$-factor (indexes m and g stand for motor and generator operation, respectively).

Now we have to load the machine with a negative load (generator operation), which, in addition, is symmetrical with respect to the **estimated** rotor flux axis. This is done by observing the field oriented coordinates, presented in figure 4.10.

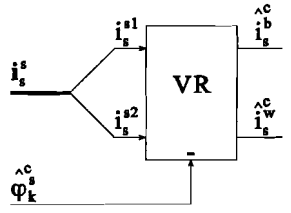

Figure 4.10: The estimated field oriented stator current coordinates.

When the first coordinate $\hat{i}_{sg}^{b^c}$ equals the value of the (same) coordinate $\hat{i}_{sm}^{b^c}$ during the motor operation, a symmetrical operating point with respect to the **estimated** rotor flux axis has been created (the magnitude of the stator current is not changed).

Next we change again the $\hat{K}_c$-factor until perpendicularity is reached. The $\hat{z}_g$-factor, which in fact is responsible for the perpendicularity is stored. With the help of formula 3.74 we can correct the $\hat{\chi}_c$-parameter with δ. At this moment we will repeat the fine identification with the **new** corrected $\hat{\chi}_c$-parameter. Appendix E.1 presents the necessary calculations step by step. After two iterations we identified the deviation in the rotor angle:

$$\hat{\chi}_c = 2.000002045 \qquad \textbf{(4.11)}$$

4.3.3 Simulation of the identification of the inductances.

During this identification we will be assisted by the U/I-model. In the machine structure of the saturated induction machine (see figure 2.16) the stator current vector with respect to the real rotor flux axis is available and it can easily be transformed to the stator coordinates with the help of φ_k^s. However, the stator voltage is not available in the machine structure. Therefore, we have to construct the stator voltage from quantities, which are available in the machine structure. The derivation of this stator voltage calculator is presented in appendix D.2. When this stator voltage calculator and the U/I-model are added to figure 4.7, an overview of this simulation remains (see figure 4.11).

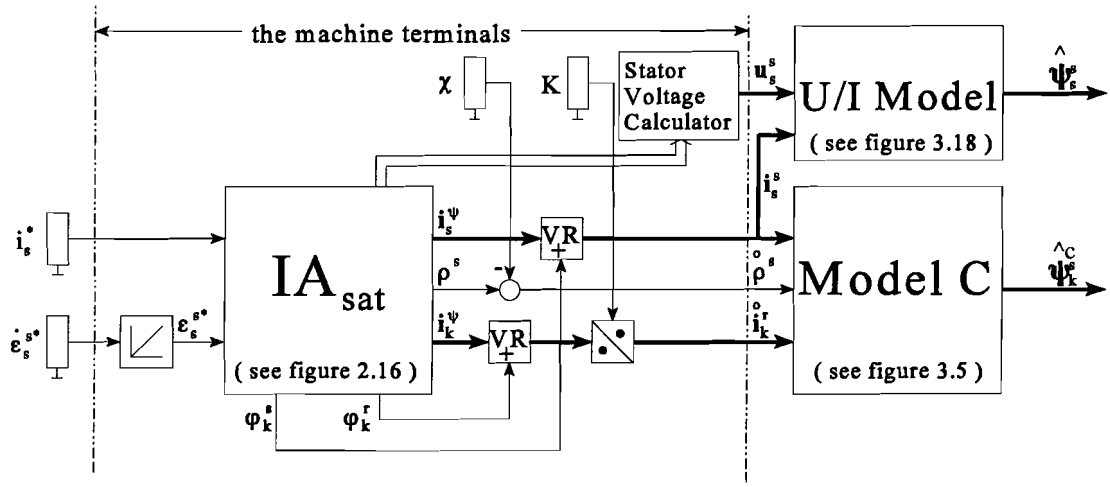

Figure 4.11: Block diagram during the simulation of the identification of the inductances.

As mentioned in section 3.3.3 we have to load the machine, before we can perform the necessary measurements. Next we enlarge the $\hat{z}_c$-factor (analogous to previous subsection we will change the $\hat{K}_c$-factor instead of the $\hat{z}$-factor and equation 4.10 again presents the relation between these two factors) until perpendicularity is reached between the rotor flux and the current. At this moment we identify the **real** rotor flux-axis (**only**

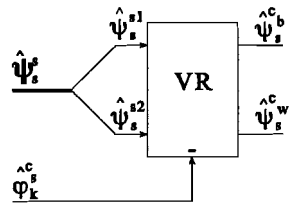

Figure 4.12: The estimated field oriented stator flux coordinates.

for this operating point). The **estimated** field oriented coordinates of the stator current and the stator flux and the $\hat{z}$-factor are stored (see figures 4.10 and 4.12). With the help of the formulae, presented at the end of section 3.3 (equations 3.94 - 3.99) we are able to calculate the inductances and the magnitude of the air-gap flux for this operating point. Appendix E.2 presents the necessary calculations. We executed this identification procedure in two operating points: linear (index $_{lin}$) and saturated (index $_{sat}$). As results of the calculations in appendix E.2 we finally get:

$$\begin{aligned} \hat{\ell}_{\sigma k,lin} &= 0.0985 \\ \hat{\ell}_{\sigma s,lin} &= 0.1310 \\ S_{lin} &= 0.2760 \\ \psi_{\ell,lin} &= 0.5212 \end{aligned} \qquad \textbf{(4.12)}$$

and

$$\begin{aligned} \hat{\ell}_{\sigma k,sat} &= 0.0989 \\ \hat{\ell}_{\sigma s,sat} &= 0.1310 \\ S_{sat} &= 0.3965 \\ \psi_{\ell,sat} &= 1.0750 \end{aligned} \qquad \textbf{(4.13)}$$

In our machine structure the leakage inductances are not affected with saturation, so $\ell_{\sigma,lin} = \ell_{\sigma,sat}$. For clearness we will show the **real** parameters of the simulation during the two operating points:

$$\begin{aligned} \hat{\ell}_{\sigma k} &= 0.1000 \\ \hat{\ell}_{\sigma s} &= 0.1310 \\ S_{lin} &= 0.2752 \\ \psi_{\ell,lin} &= 0.5213 \\ S_{sat} &= 0.3963 \\ \psi_{\ell,sat} &= 1.0750 \end{aligned} \qquad \textbf{(4.14)}$$

4.4 The parameter identification techniques applied in practice.

The results of the simulations were satisfying, so now we can start applying the identification techniques in practice. The machine will be supplied with the help of a so-called "*hysteresis Current Regulated Pulse Width Modulation*" control (hysteresis CR-PWM): the current in each phase is limited within a band. Since the star-point of the stator is not used, the course of the current in one phase depends not only on its own switching-state of the inverter, but also on the states of the other two phases. Further the width of the hysteresis band is limited due to the not infinitely fast switching of the IGBTs (dead-time). The smaller the band, the faster the IGBTs have to switch. When we would make the hysteresis band too small, this would result in an error: the hysteresis controller orders the IGBT to switch off, but this is not possible due to the dead-time of the IGBT. Further, a high DC-link voltage at low speed will result in a too fast current increase (the current depends on a first order lag defined by the stator resistance and leakage inductance) and an error in the current will eventually occur (see figures 4.13a and b). Veltman[34] recommends to apply a DC-link voltage of twice the induced voltage: the increase and decrease of the current approximately occur in the same time-interval. Figure 4.14 shows the experimental result of hysteresis control, wherein we can notice that the star-point is not connected (see the different slopes of the current).

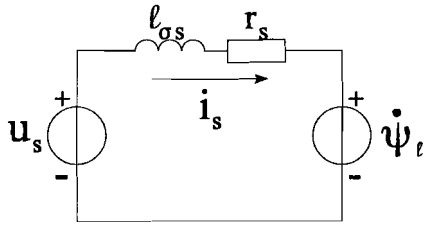

Figure 4.13a: A simplified stator circuit for one phase.

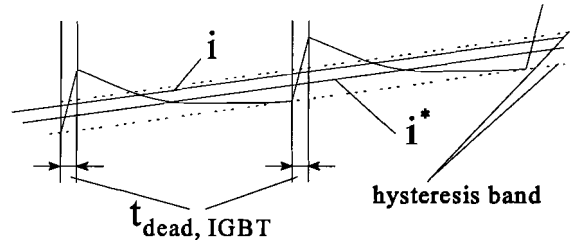

Figure 4.13b: The error in the current due to a high DC-link voltage at low speed.

During the simulation we supplied the machine structure with a stator current and frequency and this type of control proved to be quite convenient. However in practice the machine acts like a "*wild mustang*": measuring in the neighbourhood of the pull-out torque is almost impossible, because the smallest disturbance will make the machine unstable. Therefore, we suggest to "*saddle the wild mustang*". We will do that by letting the DC-machine function as a speed control, instead of only a load-machine. The DC-machine is obviously the master and the induction machine its slave. The stator frequency of the induction machine is dictated by the addition of the rotor

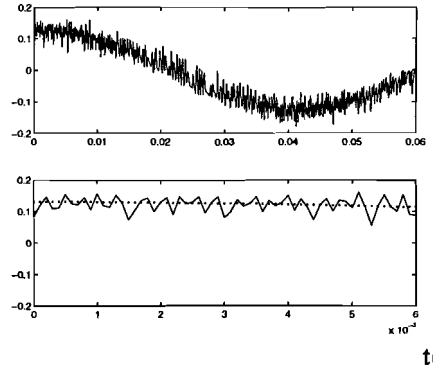

Figure 4.14: Hysteresis current control.

frequency (determined by the speed control) and an adjustable slip frequency depending on the load torque. The control of the induction machine is now very pleasant and in this way we can even pass the pull-out torque. Figure 4.15 shows the block diagram of this control method.

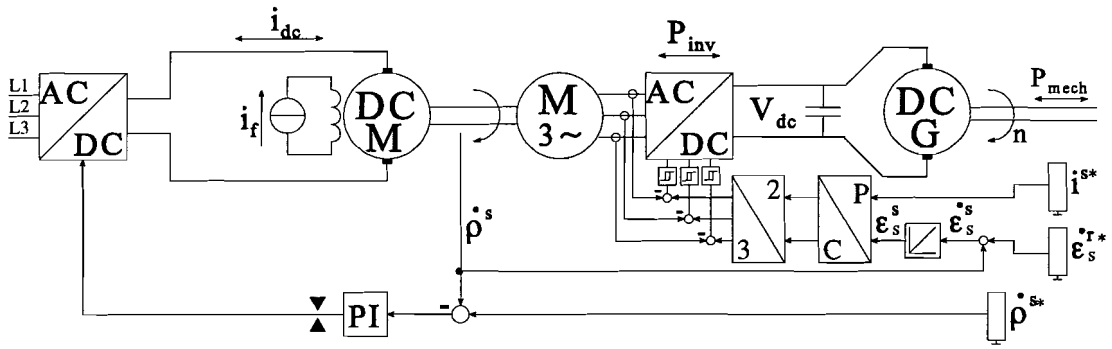

Figure 4.15: Overview of the setup in practice.

First we will adjust the PI-control of the DC-machine. This control is implemented on the DSP-system. The output of the PI-controller is limited between the rated control input values of the used power electronic device. This power device is manufactured by Siemens and it is called "*Simoreg*". With the help of these input values we can also control the torque of the DC-machine. We experimentally adjusted the control by observing the actual speed and the output of the PI-control. Increasing the P-action of the controller results in a faster response and the integrator finally eliminates the static error. Figure 4.16 shows the step response of the speed-control from standstill to 0.25 pu. On the straight line the PI-controller is limited and due to the large inertia of the total system the start-up will take a while.

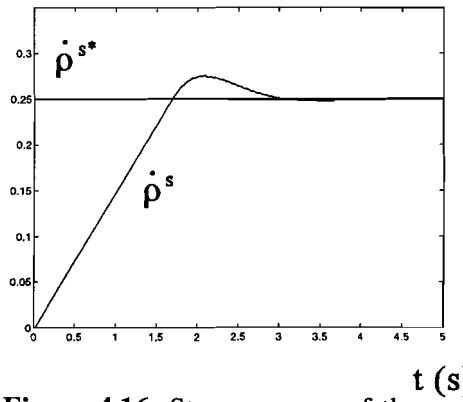

Figure 4.16: Step response of the speed control.

4.4.1 The identification of the winding ratio factor.

For this identification we need a controllable DC-current source. As mentioned in section 3.3.1 this identification technique gives only a result when the relation between magnetizing current and the magnetic field is non-linear. In other words, we have to supply the machine with a current much larger than the rated magnetizing current. In our case (see appendix C.1 for machine data) we approximately need a DC-current source in the range from 10 to 50 Ampères. Unfortunately, a current source, that is capable to operate in this range, is not available in our laboratory. Consequently, we have to construct

a current source ourselves. First we searched for a common controllable voltage source, which was capable to handle large DC-currents. Two sources were available:

- A DC-voltage source with the help of a phase angle controlled rectifier ("*Simoreg*").
- The armature voltage of a DC-generator driven with a constant speed; the armature voltage is adjustable by changing the magnetic field of the generator ("*Ward-Leonard*").

The settling time of the first source is very favourable in comparison with the second source, because changing the magnetic field of the generator takes time. However, the DC-generator will give a more smooth voltage, while the ripple in the voltage of the first source is relative large due to the switching of the SCRs. Adding a smoothing inductance will improve the shape of the voltage, but it will increase the time constant and thus it will deteriorate the settling time. We decided to apply the DC-generator, especially for the smooth voltage. The slower time response was not a serious problem, since the measurements are made during steady state. Further the DC-generator is very easy accessible, because we do not use the inverter during this identification and therefore the DC-generator supplying the DC-link is available (see also figure 4.15 and appendix C.1).

A low power voltage-controlled DC source takes care for the supply of the generator's field winding. This voltage-controlled source is on its turn connected to the DSP-system. The generator's main current is measured and also connected to the DSP-system. This control is implemented in the DSP-system in the same way as the speed control: it consists of a PI-controller with limiter. To adapt the voltage we added extra resistance to the main and the control circuit of the generator; this consequently improves the settling time of the control (the time constants become smaller: τ=L/R). For clearness the control is shown in figure 4.17. Again the PI-controller is experimentally adjusted and figure 4.18 shows a step response.

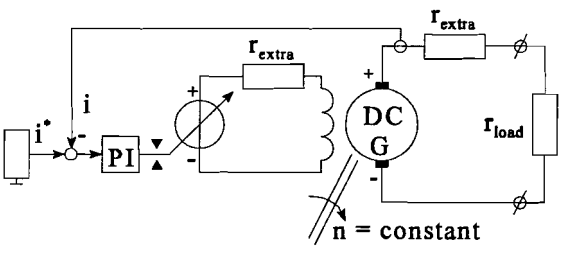

Figure 4.17: The controllable DC-current source.

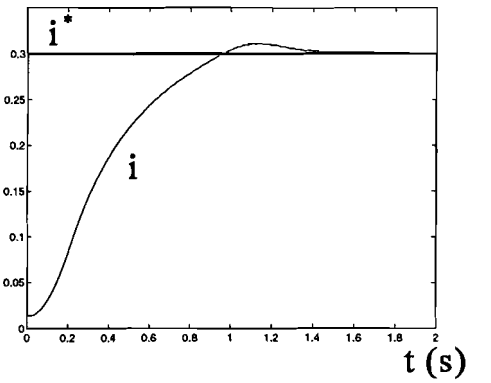

Figure 4.18: Step response of the current control.

From this moment on we are able to execute the identification method. First we supply the stator (see figure 4.19 for the connection) and observe the air-gap flux from the rotor terminals. As mentioned in section 3.3.1 we estimate the air-gap flux with the help of the U/I-model just from voltage, since the

currents in the involved windings equal zero. We measure the line voltages instead of the phase voltages, because there is no star-point in the rotor circuit available. With the help of analog electronics we transformed these voltages to phase voltages (see appendix F for the necessary transformations).

The speed control takes care for a rotor speed of approximately 0.25 pu and at this moment we observe the air-gap flux. We made different measurements starting from the linear region into the saturated one.

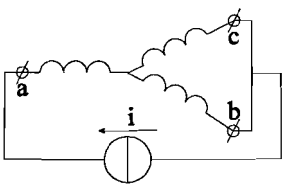

Figure 4.19: The method of the stator or rotor DC-supply.

After that we supply the rotor and observe the air-gap flux from the stator terminals (see also figure 3.11). As shown in section 3.3.1 an identification in the linear region is not possible. However, in practice the border between linearity and saturation is not so sharp as considered in our theory. This implies that an identification during linearity would be possible, but it is not recommended because the point of intersection (see figure 3.10d) is not well-defined. The exact measurements are presented in appendix E.3 and figure 4.20 shows the graphical representation of the identification of the winding ratio factor K from the linear region to saturated one. We can see that the subsequent identifications of this factor more and more converge during saturation. From this figure we obtain the final identified value of the winding ratio factor:

$$\hat{K}_c = 0.735 \tag{4.15}$$

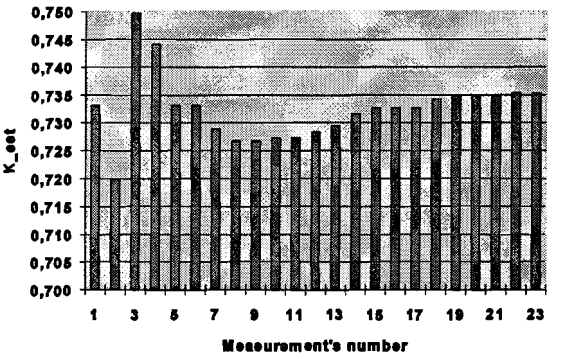

Figure 4.20: K-identification from linearity to saturation.

4.4.2 The identification of the real rotor angle.

First we have to execute the "coarse" identification method. The slip-ring induction machine will be applied as a synchronous machine and therefore the rotor will be supplied with a DC-current instead of being short-circuited. This current is provided with the DC-link voltage of the inverter and a resistance in series to limit the current. In figure 4.21 the overview of this identification is shown and figure 4.19 shows the connection of the rotor windings.

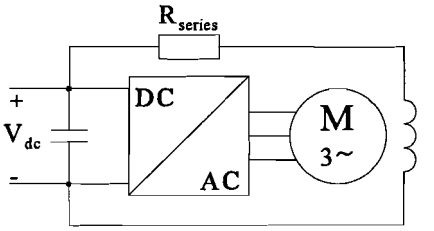

Figure 4.21: The slip-ring induction machine applied as a synchronous machine.

The best result is obtained when i_k and i_s are approximately the same. With the newly identified $\hat{K}^c$, this means:

$$i_s = \hat{K}^c . i_k^o \tag{4.16}$$

We supply the rotor with a current of 0.20 pu; according to equations 4.15 and 4.16 this approximately means a stator current of 0.15 pu. Next we have to create an ideal no-load situation; the DC-machine compensates for the losses due to friction. Model C is again connected to the slip-ring induction machine and by adapting the compensation for the rotor error angle $\hat{\chi}^c$ we will take care for parallelism (see section 4.3.2 and figure 4.9):

$$\hat{\chi}^c_{coarse} = 3.7215 \tag{4.17}$$

After that we need to execute the "fine" identification method. We refer to figure 4.15 for the overview of the setup, wherein the rotor is externally shorted. Measurements of the stator and rotor current are carried out with the same type of meters. Further model C is appropriately connected to the machine. The command value of the DC-speed control is set to 0.25 pu. Next the reference value of the stator current is set to a specific value and the inverter is switched on: the induction machine is unloaded at this moment. However by changing the slip frequency $\dot{\varepsilon}_s^*$ we are able to load the induction machine (it is even possible to pass the pull-out torque). Model C presents now its **estimated** field-oriented coordinates of the stator and rotor current. During steady state these coordinates have to be stable. Unfortunately, this is not the case in our situation due to an imbalance in the rotor circuit (the filtered coordinates move with the very low slip-frequency). The method of eliminating this unbalance by adding some resistance in the rotor circuit appeared to be impossible, because the resistance of the slip-rings depends on different quantities: current, pressure and speed (see figure 4.22). Our theory is independent of the rotor resistance,

however the chance that the variations in the resistance of the slip-rings in all three phases occur simultaneously is little. Therefore we added extra resistance in the rotor circuit. A resistance of approximately 2.6 times the real rotor resistance (130 mΩ) proved to be adequate. So in this way we reduce the relative error instead of the absolute error. At this moment we are able to execute the same procedure as described in section 4.3.2. Appendix E.4 shows the necessary measurements and calculations yielding:

$$\chi_{fine}^{\hat{}c} = 3.6792 \qquad (4.18)$$

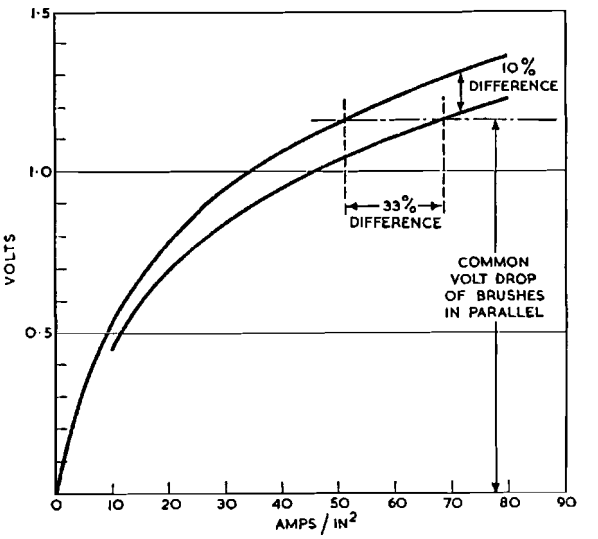

Figure 4.22: The variation in resistance due to current and pressure of the brushes on the rings (source: Morganite[22]).

4.4.3 The identification of the inductances.

We can use the same experimental setup as during the "fine" identification in the previous section. Again we have to change the $\hat{K}_c$-value until perpendicularity between the rotor flux and current is available. At this moment we will identify the **real** rotor flux-axis. In other words, the field oriented coordinates of stator current are available. Furthermore we need assistance of the U/I-model for this identification and this model is fed by the line voltages (see appendix F for the necessary transformations). These voltages are filtered with the same low-pass filters (anti-aliasing) as the current filters ($f_{cut\text{-}off}$ = 5 kHz). Because the stator voltages are directly the results of the states of the CR-PWM inverter (see section 4.4), they contain steep slopes, which will trouble the integration action of the U/I-model (see figure 3.18). An extra low-pass filter (LPF) is used to smooth the input of the integrator: stator voltage subtracted with the ohmic voltage drop. However, this filter will introduce a relatively large phase-error in comparison with the filters of the currents due to its very low cut-off frequency. Therefore we apply a low-pass filter with a compensation for the phase error. With the help of analog electronics a circuit is constructed, which transforms the filtered three-phase voltages and currents to the two-phase system. The stator ohmic voltage drop is subtracted from the stator voltage: the derivative of stator flux remains. The phase error of this derivative of the stator flux vector is corrected by rotating this vector back with an appropriate angle. This angle depends on the frequency of the stator flux and consequently on the frequency of the stator current. This filter only functions during steady state, but since our identification method makes use of steady-state measurements this is not a problem (see figure 4.23). The stator resistance is estimated at frequency zero: the derivative of stator flux equals zero. Consequently the ohmic voltage drop has to equal the stator voltage.

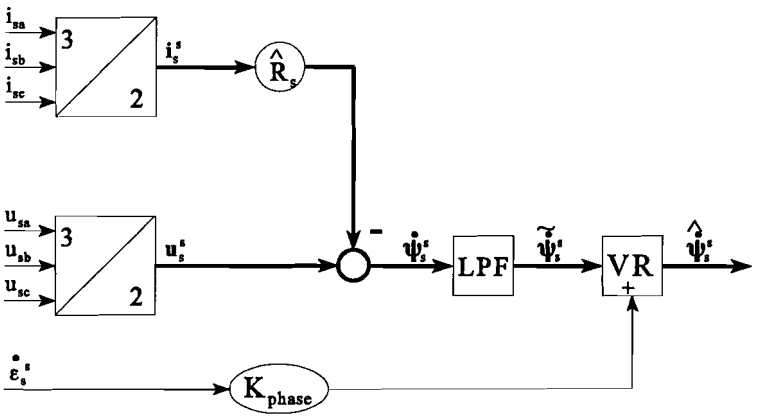

Figure 4.23: The low-pass filter with a phase compensation for the U/I-model.

So, besides the field-oriented coordinates of the stator current the field-oriented coordinates of the stator flux are available at this moment. With the formulae 3.94 to 3.96 we can estimate the inductances. However this identification failed for every working point (it resulted in a negative stator leakage inductance). The estimation of the stator leakage inductance will become negative in case the estimation of the rotor leakage inductance is too large, since $\hat{\ell}_{\sigma s}$ directly depends on $\hat{\ell}_{\sigma k}$ (see equation 3.86). In other words we have to enlarge the $\hat{Z}$-factor (and thus $\hat{\ell}_{\sigma k}$, see equation 3.47) extremely before perpendicularity is reached. The iron losses, due to hysteresis and eddy currents are responsible for this too large perpendicularity factor: the **real** air-gap flux axis has a phase delay with respect to the "*apparent*" magnetizing current vector, which is constructed from the stator and rotor current (see also equation 3.2). Therefore we have to adapt our theory and also to reconsider the validity of the parameter identification techniques.

4.5 The theory of model C, extended with iron losses.

Due to an alternating magnetic field, losses will occur in the machine iron. We can divide these losses into two types:

- losses due to hysteresis;
- losses due to eddy currents.

Weiss[4] proposed a theory, which considers a real ferromagnetic material (two types: hard (permanent magnets), eg. alloys from the AlNiCo-group and soft (non-permanent magnets), eg. iron-silicon alloys) as a lot of small regions, also called Weiss-domains. These domains (magnetic dipoles) are orientated by an external magnetic field. When this H-field is reduced to zero, some domains will keep their

[4]Pierre-Ernest Weiss (1865-1940): A French scientist, who described the magnetic phenomena in ferromagnetic materials with the help of quantum theory (source: STW[29]).

orientation, which in fact is the explanation of remanent magnetism. The eddy current losses originate, since the magnetic field induces a current in the machine iron. However, by increasing the resistance of the iron perpendicular to the magnetic flux the losses will be reduced. Therefore machine and transformer iron usually consists of laminated, electrical insulated plates of the iron-silicon alloy.

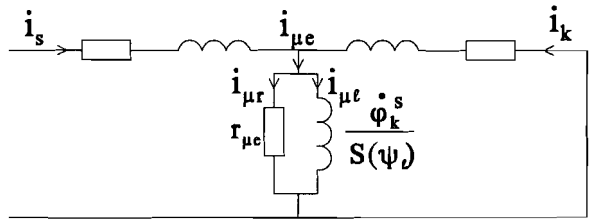

Figure 4.24: The machine model extended with iron losses.

In machine theory these losses are considered as resistive (see figure 4.24). So equation 3.2 is no longer valid: the "*apparent*" magnetizing current $\mathbf{i}_{\mu e}$ consists of the addition of the **real** magnetizing current $\mathbf{i}_{\mu \ell}$ and the current $\mathbf{i}_{\mu r}$, which is responsible for the iron losses:

$$\mathbf{i}_{\mu e}^s = \mathbf{i}_s^s + \mathbf{i}_k^s \tag{4.19}$$

and

$$\mathbf{i}_{\mu \ell}^s = \mathbf{i}_{\mu e}^s - \mathbf{i}_{\mu r}^s \tag{4.20}$$

Equations 3.3 and 3.4 remain unaltered:

$$\boldsymbol{\psi}_\ell^s = \frac{1}{S(\psi_\ell)} \cdot \mathbf{i}_{\mu \ell}^s \tag{4.21}$$

and

$$\boldsymbol{\psi}_k^s = \boldsymbol{\psi}_\ell^s + \ell_{\sigma k} \cdot \mathbf{i}_k^s \tag{4.22}$$

Again figure 3.2 plays an important role in model C and is still valid in the case of iron losses. Consequently equations 3.5 and 3.6 remain also unchanged:

$$\boldsymbol{\psi}_k^s = \frac{1}{S(\psi_\ell)} \cdot \mathbf{i}_{\mu k}^s \tag{4.23}$$

and

$$\mathbf{i}_{\mu k}^s = \mathbf{i}_{\mu \ell}^s + S(\psi_\ell) \cdot \ell_{\sigma k} \cdot \mathbf{i}_k^s \tag{4.24}$$

The construction of the rotor current vector $\hat{\mathbf{i}}_k^{s_c}$ and the origin of the $S(\psi_\ell)$-function are also still valid (see figures 3.3 and 3.4). In figure 4.25 the vector diagram of model C with the compensation for the iron losses is shown. The ohmic current $\mathbf{i}_{\mu r}$ creates together with the **real** magnetizing current $\mathbf{i}_{\mu\ell}$ the "*apparent*" magnetizing current $\mathbf{i}_{\mu e}$. The current $\mathbf{i}_{\mu r}$ leads the **real** magnetizing current $\mathbf{i}_{\mu\ell}$ by a phase angle of 90 ° (the direction of the stator current is considered counterclockwise, also in the other situations). The angle η between $\mathbf{i}_{\mu\ell}$ and $\mathbf{i}_{\mu e}$ is determined with:

$$\eta = \arctan\frac{i_{\mu r}}{i_{\mu\ell}} \tag{4.25}$$

However, we can estimate this angle also with the ratio between the impedances (see figure 4.24):

$$\eta = \arctan\frac{\dot{\varphi}_k^s}{S(\psi_\ell).r_{\mu e}} \tag{4.26}$$

, wherein $\dot{\varphi}_k^s$ is the angular velocity of the flux. The resistance $r_{\mu e}$ can be considered as a parallel circuit of four resistors, representing:

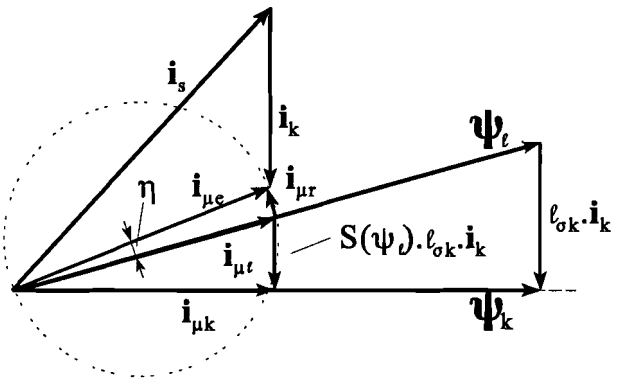

Figure 4.25: Vector diagram of model C, extended with iron losses.

- losses in stator iron due to hysteresis effect ($r_{st,\,hys}$);
- losses in stator iron due to eddy currents ($r_{st,\,ed}$);
- losses in rotor iron due to hysteresis effect ($r_{ro,\,hys}$);
- losses in rotor iron due to eddy currents ($r_{ro,\,ed}$).

So with this consideration we can write equation 4.26 as follows:

$$\eta = \arctan\left(\frac{\dot{\varphi}_k^s}{S(\psi_\ell)}.\left(\frac{1}{r_{st,hys}}+\frac{1}{r_{st,ed}}+\frac{1}{r_{ro,hys}}+\frac{1}{r_{ro,ed}}\right)\right) \tag{4.27}$$

However, the angle η will be small:

$$\eta < 6° \tag{4.28}$$

and therefore we can approximate equation 4.27 with:

$$\eta \approx \frac{\dot{\varphi}_k^s}{S(\psi_\ell)}.\left(\frac{1}{r_{st,hys}}+\frac{1}{r_{st,ed}}+\frac{1}{r_{ro,hys}}+\frac{1}{r_{ro,ed}}\right) \tag{4.29}$$

Model C will especially be used at low frequencies, therefore we can neglect the influences of eddy currents. Eddy currents depend on the square of the frequency of the applied magnetic field. Further the iron losses in the rotor can normally be neglected (the frequency of the H-field is almost zero in case of a machine with steep characteristics), but since we added extra resistance to the rotor circuit it is not

allowed anymore to ignore these losses. Hysteresis losses can also not be considered as constant: they vary linearly with the frequency of the applied H-field. The angle η depends also on the frequency and the main inductance: both differ in different operating points. It is obvious, that it will not be easy to estimate this angle. Unfortunately this means, that we are not able to identify the leakage and main inductances. However, in next section we will present an accurate approximation of model C, which estimates the flux position only during steady state.

4.6 An adaption of model C, only valid for steady state.

The previous section proved that our assumption, concerning the neglect of the iron losses seemed to be incorrect. Identifying the parameters of the new model (extended with iron losses) is almost impossible. However, we can derive a variant of model C which is only valid for steady state. In steady state the rotor flux is perpendicular to the rotor current. On condition that the parameter $\hat{\chi}_c$ has accurately been identified we will identify the **real** rotor flux-axis when perpendicularity is reached. Perpendicularity will be provided with the help of a controller.

With the help of equation 4.19 we can estimate the "*apparent*" magnetizing current vector $\mathbf{i}_{\mu e}$ in case the identification of the winding ratio factor K is reliable. In figure 4.26 the vector diagram of the steady-state model is shown. The "*nod*" in the rotor current (see figure 4.25) is neglected. Since the angle η is very small, the "fictitious" magnetizing current vector $i_{\mu k}$ of figure 4.26 will be a good approximation of the **real** "fictitious" magnetizing current vector $i_{\mu k}$ (see figure 4.25). The rotor flux position can be calculated with the reciprocal value of the main inductance, see equation 4.23. However we are not able yet to identify the magnetisation curve. Further the air-gap flux is not available, which in fact is the input parameter of the $S(\psi_\ell)$-function. Instead of the air-gap flux we can use the air-gap magnetizing current $i_{\mu\ell}$ as input parameter, which depends on the angle η and $i_{\mu e}$:

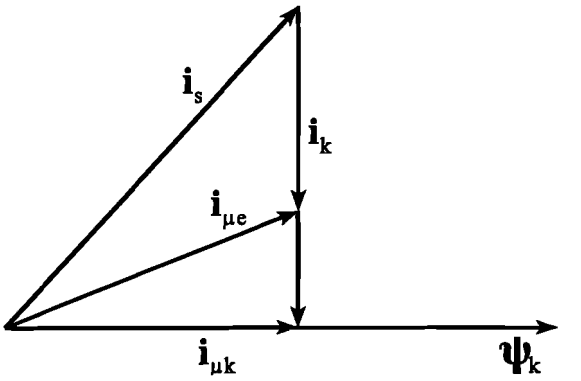

Figure 4.26: Vector diagram of model C, only valid for steady state.

$$i_{\mu\ell} = i_{\mu e}.\cos\eta \qquad \textbf{(4.30)}$$

and due to the smallness of the angle η (see equation 4.28) we can approximate this equation with:

$$i_{\mu\ell} \approx i_{\mu e} \qquad \textbf{(4.31)}$$

Next we have to derive an identification procedure for the magnetisation curve. Normally spoken this identification will simultaneously be executed with the K-identification. When we supply again the rotor with a direct current and the rotor is rotating at a certain speed a voltage will be induced in the stator's windings. With the U/I-model we can again measure the stator flux from the stator terminals; because we are measuring with an open stator (i.e. no stator current) this flux equals the **real** air-gap flux (see

equation 3.32). Further the total rotor current will be used for the magnetisation (only in the stator's iron losses will occur, because the magnetic field in the rotor is static; and due to the relatively low frequency of 0.25 pu this error is negligible). Further this identification considers only the magnitudes of the vectors, and the magnitudes are almost not affected by iron losses. However, one parameter has been ignored till now: the winding ratio factor, which is estimated in section 4.4.1. The rotor current has to be corrected with the winding ratio factor. From the measured rotor current we can calculate the rotor current seen from the stator terminals and thus the magnetizing current with:

$$i_k = K.\overset{o}{i}_k = i_{\mu\ell} \tag{4.32}$$

Appendix E.5 shows the measurements of the magnetisation curve and also the S-values, which can be calculated with:

$$S = \frac{i_{\mu l}}{\psi_\ell} \tag{4.33}$$

Now we will consider the S-values as function of the magnetizing current $i_{\mu\ell}$ and with the help of our interpolation program (see section 4.2) we approximate this function with (see figure 4.27):

$$\begin{aligned} S(i_{\mu\ell}) = S_0 &+ 6.94*(i_{\mu\ell} - i_{\mu\ell\,sat})^2 - 31.59*(i_{\mu\ell} - i_{\mu\ell\,sat})^3 \\ &+ 71.52*(i_{\mu\ell} - i_{\mu\ell\,sat})^4 - 78.88*(i_{\mu\ell} - i_{\mu\ell\,sat})^5 + 33.71*(i_{\mu\ell} - i_{\mu\ell\,sat})^6 \end{aligned} \tag{4.34}$$

with

$$S_0 = 0.1740 \text{ pu} \tag{4.35}$$

and

$$i_{\mu\ell\,sat} = 0.0974 \text{ pu} \tag{4.36}$$

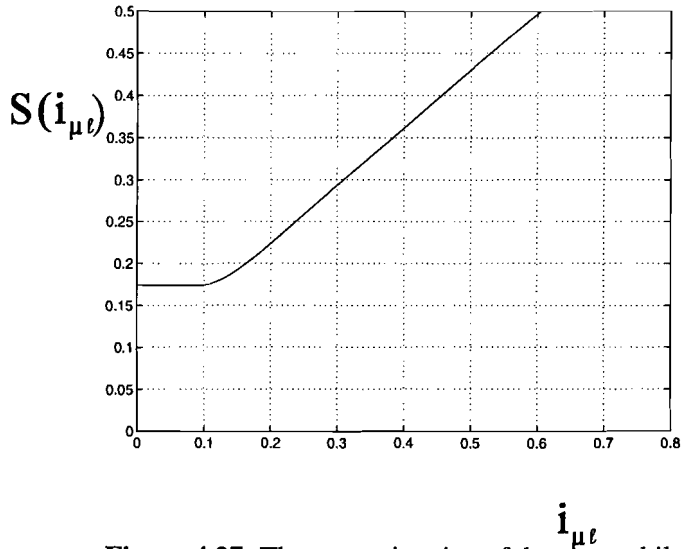

Figure 4.27: The approximation of the meanwhile identified $S(i_{\mu\ell})$-function.

This steady-state model will estimate the **real** flux position with a high accuracy in spite of the made approximations. This model is shown in figure 4.28. The construction of the rotor current in the stator coordinate-system is not included in this figure. Perpendicularity is automatically achieved with just an integration action (a proportional action is not needed, since this action is already available in the model (see figure 4.28)). During the derivation of this model we assumed, that the identifications of χ and K are reliable. However, we have to reconsider the strength of the identification techniques in case of iron losses. This consideration will be treated in the next section.

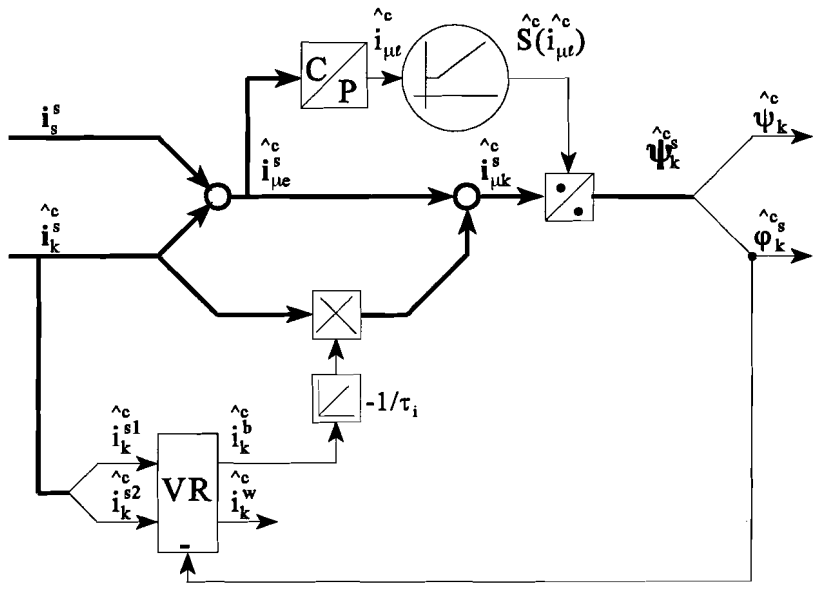

Figure 4.28: A variant of model C, only valid for steady state.

4.7 Reconsideration of the identification techniques of χ and K in case of iron losses.

As mentioned in the section above: the phase delay due to iron losses disturbs our theory. Because the identification of the winding ratio factor K only considers the magnitudes (see also the identification of the magnetisation curve in previous section), the identification will almost not be influenced by the iron losses.

The identification of the compensation angle χ will nevertheless be influenced by the phase delay due to the iron losses. Therefore we have to reconsider first the "coarse"-identification. During the coarse identification the induction machine is applied as a synchronous machine.

First we have to reconsider the magnetizing equation 3.45. Analogous to the considerations in the previous sections: the addition of the stator and the rotor current creates not the **real** magnetizing current: So equation 3.45 is no longer valid. During ideal no-load the rotor and stator current are both used for the magnetisation of the iron **and** for the iron losses. The rotor flux will have the direction of the air-gap flux in a no-loaded synchronous machine. Consequently the rotor current will have also the same direction, since this current depends on the direction of both fluxes (see also equation 3.4). Figures 4.29a and b show the vector diagrams of a no-loaded synchronous machine with the stator current direction counterclockwise and clockwise, respectively. These diagrams show, that instead of the real χ we estimate the $\hat{\chi}_+$ or $\hat{\chi}_-$, respectively. However, executing both directions will provide the opportunity to identify the real χ:

$$\chi = \frac{\hat{\chi}_+ - \hat{\chi}_-}{2} \tag{4.37}$$

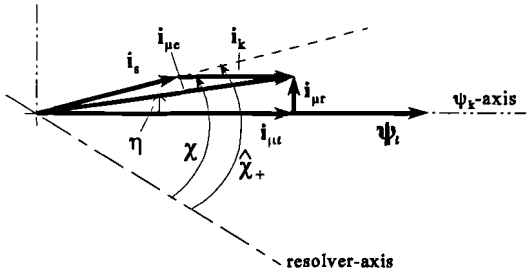

Figure 4.29a: Vector diagram of the no-loaded synchronous machine; direction of stator current is counterclockwise.

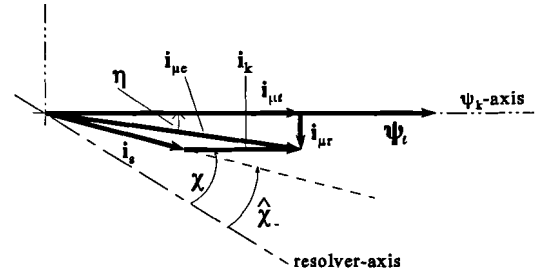

Figure 4.29b: Vector diagram of the no-loaded synchronous machine; direction of stator current is clockwise.

On condition that the magnitudes of the stator and rotor current are available we can estimate the angle of the iron losses η:

$$\eta = \frac{i_s.\sin(\hat{\chi}_+ - \chi)}{i_s.\cos(\hat{\chi}_+ - \chi) + i_k} \tag{4.38}$$

However, this angle represents only the phase delay caused by the iron losses in the stator, since the magnetic field in the rotor of a synchronous machine is static. Further this angle is only valid for the applied stator frequency. We made three measurements for different frequencies (the DC-machine provided an ideal no-load):

$$\left.\begin{aligned} \dot{\varepsilon}_s^s &= 0.05\,\text{pu} \\ i_s &= 0.36\,\text{pu} \\ i_r &= 0.36\,\text{pu} \\ \hat{\chi}_+ &= -2.5679\,\text{rad} \\ \hat{\chi}_- &= -2.7060\,\text{rad} \end{aligned}\right\} \begin{aligned} \hat{\chi} &= -2.6370\,\text{rad} \\ \hat{\eta} &= 0.03456\,\text{rad} = 1.98° \end{aligned} \tag{4.39}$$

$$\left.\begin{array}{l} \dot{\varepsilon}_s^s = 0.10\,\text{pu} \\ i_s = 0.36\,\text{pu} \\ i_r = 0.36\,\text{pu} \\ \hat{\chi}_+ = -2.5464\,\text{rad} \\ \hat{\chi}_- = -2.7336\,\text{rad} \end{array}\right\} \begin{array}{l} \hat{\chi} = -2.64\,\text{rad} \\ \hat{\eta} = 0.0468\,\text{rad} = 2.68° \end{array} \qquad \textbf{(4.40)}$$

$$\left.\begin{array}{l} \dot{\varepsilon}_s^s = 0.15\,\text{pu} \\ i_s = 0.36\,\text{pu} \\ i_r = 0.36\,\text{pu} \\ \hat{\chi}_+ = -2.5342\,\text{rad} \\ \hat{\chi}_- = -2.7581\,\text{rad} \end{array}\right\} \begin{array}{l} \hat{\chi} = -2.6462\,\text{rad} \\ \hat{\eta} = 0.0561\,\text{rad} = 3.21° \end{array} \qquad \textbf{(4.41)}$$

Our theory, concerning the iron losses has been proved by the experimental results: the angle η increases with the frequency. The final result of the "coarse"-identification yields:

$$\chi_{coarse} = -2.64\,\text{rad} \qquad \textbf{(4.42)}$$

The next identification applies the induction machine in two symmetrical states: motor and generator operation. The vector diagrams of these two states are shown in figures 4.25(motor operation) and 4.30(generator operation).

These diagrams show obviously, that the symmetry is lost. This means that the "fine"-identification technique, presented in section 3.3.2 is **no longer** valid in the case of iron losses. The reason for introducing this "fine"-identification is the uncertainty of creating an ideal no-load situation.

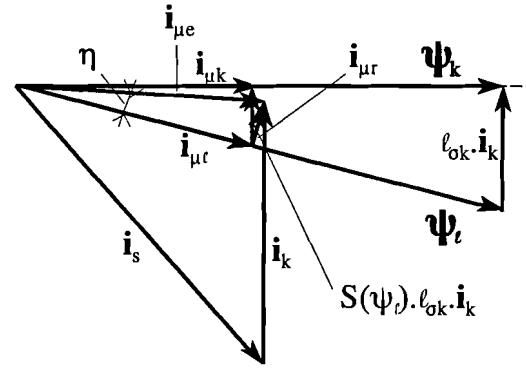

Figure 4.30: Vector diagram of model C, extended with iron losses: generator operation.

However, there is also another method for identifying the real angle χ. It concerns a measurements at standstill with an open rotor. We supply first two stator windings with an alternating current. The rotor winding voltage (corresponding with the stator windings) is measured. This voltage depends on the position of the rotor. Maximal coupling is reached when the angle between the rotor windings and their corresponding stator windings is zero. However, the most accurate result will be obtained by turning the rotor until no voltage will be induced in the rotor windings: the angle between the corresponding windings is now equal to 90 degrees (see figure 4.31). This method estimates the physical position of the rotor windings with a high accuracy. However, in our model we are only interested in the electrical position of the three windings together. We carried out three measurements and since the pole-number of the machine is equal to 1 the physical position is equal to the electrical position:

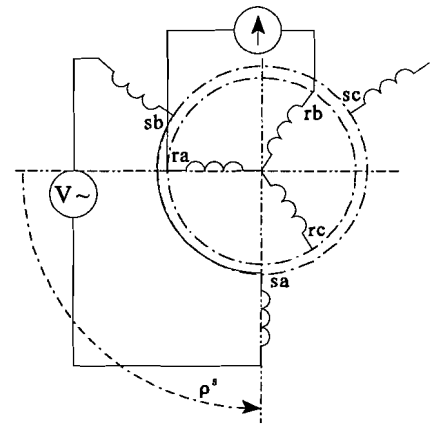

Figure 4.31: The estimation of the position of the rotor windings with respect to the stator windings.

$$\left.\begin{array}{lll} V_{sab}\,;V_{rab}=0 & \longrightarrow & \rho^{s}=4.198\,\text{rad} \\ V_{sbc}\,;V_{rbc}=0 & \longrightarrow & \rho^{s}=4.195\,\text{rad} \\ V_{sac}\,;V_{rac}=0 & \longrightarrow & \rho^{s}=4.202\,\text{rad} \end{array}\right\} \rho^{s}_{av}=4.198\,\text{rad} \qquad (4.43)$$

The compensation for the rotor angle χ can be found with:

$$\chi = \frac{\pi}{2} - \rho^{s}_{av} = -2.627 \qquad (4.44)$$

We see that our assumption, that it is almost impossible for creating a **real** ideal no-load situation, proves to be correct.

At this moment we identified every parameter which is necessary for the steady-state model. Unfortunately the identification of the leakage inductances failed, since the position of the air-gap flux vector is not known due to the iron losses. A possibility to identify the inductances in every operating-point is the application of diameter windings within the air gap of the machine. With the help of these windings we can directly measure the air-gap flux and with our steady-state model C and the U/I-model we will estimate the rotor flux, the rotor current and the stator flux. With the help of the following equations we can directly estimate the leakage inductances:

$$\boldsymbol{\psi}^{s}_{k} = \boldsymbol{\psi}^{s}_{\ell} + \ell_{\sigma k}.\mathbf{i}^{s}_{k} \qquad (4.45)$$

and

$$\boldsymbol{\psi}^{s}_{s} = \boldsymbol{\psi}^{s}_{\ell} + \ell_{\sigma s}.\mathbf{i}^{s}_{s} \qquad (4.46)$$

CHAPTER 5

CONCLUSIONS AND RECOMMENDATIONS

5.1 The machine structure affected with saturation.

A great advantage of this structure is the similarity between the linear and the saturated structure. This is especially convenient for better understanding of the machine behaviour, also during saturation. In comparison with the linear structure only the saturable function $S_z(\psi_r)$ has to be identified. In case of a slip-ring induction machine this function can easily be obtained during no-load, see also chapter 4. However, in case of a squirrel cage induction machine one has to **estimate** this function during no-load. With the help of equation 3.32 one is able to estimate the air-gap flux from the stator flux, on the condition that the stator leakage inductance is known. The stator flux is the result of the integration of the stator voltage subtracted with the ohmic voltage drop and during no-load the stator current is equal to the magnetizing current.

In spite of the choice for the rotor flux coordinate system the structure is still very comprehensible (a choice for the air-gap flux coordinate system yields maybe a more compact structure, since we had to construct the air-gap flux magnitude for the $S_z(\psi_r)$-function). Further the rotor flux is more stable, because the stator flux is directly dependent of the inverter voltage and the air-gap flux indirectly according to equation 3.32.

The saturation effects in a linear and non-linear Field Oriented Control are clearly presented in 3D-graphics. Such a presentation enables us to show different courses in a very compact way. In case of a linear Field Oriented Control deviations in the torque and the flux level will occur. The non-linear Field Oriented Control, on the other hand, takes care for good control.

5.2 Model C, a new model for flux locating in a slip-ring induction machine.

This model will be used as reference model for further research on the invention within the section "*Electromechanics and Power Electronics*", see Blaschke[6]. The demands made on this reference model are considerable: a high performance in the whole frequency range in the linear region as well as in the saturated one. However, a reference model does not necessarily need to be applicable to an industrial environment, since it is usually used for purely scientific applications. We exploited this opportunity by deriving a reference model (model C), which is only applicable to a slip-ring induction machine. With this exploitation a new measurable quantity is available: the rotor current.

Preliminary experimental results showed, that iron losses can not be ignored. At the end of chapter 4 we suggest to apply a variant of model C. This model (see figure 4.28) functions only during steady state, but its performance is outstanding in the whole frequency range (also during saturation), and for the application in a purely scientific research this will satisfy.

5.3 Recommendations.

An asymmetry in the rotor disturbed the necessary measurements for the execution of the identification techniques. Since the resistance of the slip rings is most dominant in the rotor circuit and can not be considered as time-independent, we decreased the asymmetry by adding extra resistance in the rotor circuit. Because of this the machine has a less steep torque characteristic and this complicates the identification of the angle η of the iron losses (see section 4.5). The machine used in the experimental results will hopefully be replaced with a more symmetrical one.

Further we recommend to apply the model, presented in figure 4.28, as reference model. In this model perpendicularity between the rotor current and the rotor flux-axis is automatically controlled. As a result of this, the model is nearly frequency-independent.

REFERENCES

Asselt[1] R. van Asselt, R.B.J. Pijlgroms, W.V. Smeets, G. van der Zee, H. Zoete
WISKUNDE 3
-Analyse en numerieke wiskunde.
Culemborg: Educaboek B.V., 1991.

Blaschke[2] F. Blaschke
DAS PRINZIP DER FELDORIENTIERUNG, DIE GRUNDLAGE FÜR DIE TRANSVEKTOR-REGELUNG VON DREHFELDMASCHINEN.
Siemens-Zeitschrift, vol. 45, no. 10, p. 757-760, 1971.

Blaschke[3] F. Blaschke
DAS VERFAHREN DER FELDORIENTIERUNG ZUR REGLUNG DER DREHFELDMASCHINE.
Ph.D. thesis, Technische Universität Braunschweig, 1973.

Blaschke[4] F. Blaschke, A.J.A. Vandenput
REGELTECHNIEKEN VOOR DRAAIVELDMACHINES.
Eindhoven University of Technology, EUT Report 96-E296, 1996.

Blaschke[5] F. Blaschke, A.J.A. Vandenput, J. van der Burgt
FELDORIENTIERUNG DER GEBERLOSEN DREHFELDMASCHINE.
ETZ, 1995, no. 21, p. 14-23.

Blaschke[6] F. Blaschke, J. van der Burgt, A.J.A. Vandenput
SENSORLESS DIRECT FIELD ORIENTATION AT ZERO FLUX FREQUENCY.
In: *Conf. Rec. IEEE Industry Applications Society Annual Meeting*, San Diego, 1996, p. 189 - 196.

Blaschke[7] F. Blaschke
DIE FELDORIENTIERUNG DER GESÄTTIGTEN ASYNCHRONMASCHINE.
Eindhoven University of Technology, Technical Report no. EMV 96-24, 1996.

Blaschke[8] F. Blaschke
M_c - EIN NEUES MODELL ZUR FLUSSERFASSUNG BEI SCHLEIFRINGLAUFERMASCHINEN.
Eindhoven University of Technology, Technical Report no. EMV 96-25, 1996

Blaschke[9] F. Blaschke
EIN VERBESSERTES PARAMETER-ERMITTLUNGS-VERFAHREN FÜR DAS MODELL M_c.
Eindhoven University of Technology, Technical Report no. EMV 96-26, 1996.

Bosga[10] S.G. Bosga
ASYMMETRICAL SUPPLY OF INDUCTION MACHINES
-Remedial Operating Strategies in case of Converter Faults.
Ph.D. thesis, Eindhoven University of Technology, 1997.

Brown[11] J.E. Brown, K.P. Kovacs, P. Vas
A METHOD OF INCLUDING THE EFFECTS OF MAIN FLUX PATH SATURATION IN THE GENERALIZED EQUATIONS OF A.C. MACHINES.
IEEE Trans. on Pow. App. and Syst., vol. PAS-102, no. 1, p. 96 - 103, January 1983.

Burgt[12] J.J.A. van der Burgt
THE VOLTAGE/CURRENT MODEL IN FIELD-ORIENTED AC DRIVES AT VERY LOW FLUX FREQUENCIES.
Ph.D. thesis, Eindhoven University of Technology, 1996.

Healey[13] R.C. Healey, S. Williamson, A.C. Smith
IMPROVED ROTOR MODELS FOR VECTOR CONTROLLERS.
In: *Conf. Rec. IEEE Industry Applications Society Annual Meeting*, Denver, 1994, p. 575-584.

Holtz[14] J. Holtz
STATE OF THE ART OF CONTROLLED AC DRIVES WITHOUT SPEED SENSOR.
In: *Proc. of the Int. Conf. on Power Electr. and Drive Systems*, Singapore, Vol. 1, 1995, p. 1 - 6.

Kanmachi[15] T. Kanmachi, I. Takahashi
SENSOR-LESS SPEED CONTROL OF AN INDUCTION MACHINE WITH NO INFLUENCE OF SECONDARY RESISTANCE VARIATION.
In: *Conf. Rec. IEEE Industry Applications Society Annual Meeting*, Toronto, 1993, p. 408 - 413.

Keyhani[16] A. Keyhani, H. Tsai
IGSPICE SIMULATION OF INDUCTION MACHINES WITH SATURABLE INDUCTANCES.
IEEE Trans. on En. Conv., vol. 4, no. 1, p. 118 - 125, March 1989.

Kreyszig[17] E. Kreyszig
ADVANCED ENGINEERING MATHEMATICS
Canada: John Wiley & Sons Inc., 1993.

Levi[18] E. Levi
A UNIFIED APPROACH IN D-Q AXIS MODELS OF INDUCTION MACHINES.
IEEE Trans. on En. Conv., vol. 10, no. 3, p. 455 - 461, September 1995.

Lipo[19] T.A. Lipo, A. Consoli
MODELING AND SIMULATION OF INDUCTION MOTORS WITH SATURABLE LEAKAGE REACTANCES.
IEEE Trans. on Ind. Appl., vol. 20, no. 1, p. 180 - 189, Jan./Feb. 1984.

Lorenz[20] R.D. Lorenz, D.W. Novotny
SATURATION EFFECTS IN FIELD-ORIENTED INDUCTION MACHINES.
IEEE Trans. on Ind. Appl., vol. 26, no. 2, p. 283 - 289, Mar./Apr. 1990.

Lorenz[21] R.D. Lorenz
FUTURE TRENDS IN POWER ELECTRONIC CONTROL OF DRIVES: ROBUST, ZERO SPEED SENSORLESS CONTROL AND NEW STANDARD APPROACHES FOR FIELD ORIENTATION.
In: *Conf. Rec. IPEC* , Yokohama, 1995, p. 23 - 28.

Morganite[22] -
CARBON BRUSHES AND ELECTRICAL MACHINES.
Morganite Carbon Limited, 1961.

Schauder[23] C. Schauder
ADAPTIVE SPEED IDENTIFICATION FOR VECTOR CONTROL OF INDUCTION MOTORS WITHOUT ROTATIONAL TRANSDUCERS.
IEEE Trans. on Ind. Appl., vol. 28, no. 5, p. 1054 - 1061, Sept./Oct. 1992.

Schierling[24] H. Schierling
SELF COMMISSIONING - A NOVEL FEATURE OF INVERTER-FED MOTOR DRIVES.
In: *IEE Conf. Rec., Power Electronics and variable Speed Drives*, London, 1988, p. 287 - 290.

Schroedl[25] M. Schroedl, D. Hennerbichler, T.M. Wolbank
INDUCTION MOTOR DRIVE FOR ELECTRIC VEHICLES WITHOUT SPEED- AND POSITION SENSORS.
In: *Proc. of the Eur. Conf. on Power Electronics and Applications (EPE),* Brighton, 1993, vol. 5, p. 271 - 275.

Schroedl[26] M. Schroedl
SENSORLESS CONTROL OF AC MACHINES AT LOW SPEED AND STANDSTILL BASED ON THE "INFORM" METHOD.
In: *Conf. Rec. IEEE Industry Applications Society Annual Meeting*, San Diego, 1996, p. 270 - 277.

Smith[27] A.C. Smith, R.C. Healey, S. Williamson
A TRANSIENT INDUCTION MOTOR MODEL INCLUDING SATURATION AND DEEP BAR EFFECT.
IEEE Trans. on En. Conv., vol. 11, no. 1, p. 8 - 15, March 1996.

Stanley[28] H.C. Stanley
AN ANALYSIS OF THE INDUCTION MACHINE.
AIEE Trans., Vol. 57, p. 751 - 757, 1938.

STW[29] -
MULTIMEDIA ENCYCLOPEDIA CD-ROM
The Software Toolworks

Sumner[30] M. Sumner, G.M. Asher
THE EXPERIMENTAL INVESTIGATION OF MULTI-PARAMETER IDENTIFICATION METHODS FOR CAGE INDUCTION MACHINES.
In: *Proc. of the Eur. Conf. Om Power Electronics and Applications (EPE),* Firenze, 1991, vol. 4, p. 389-394.

Sung-Il Yong[31] Sung-Il Yong, Yong-Woo Choi, Seung-Ki Sul
SENSORLESS VECTOR CONTROL OF INDUCTION MACHINE USING HIGH FREQUENCY CURRENT INJECTION.
In: *Conf. Rec. IEEE Industry Applications Society Annual Meeting*, Denver, 1994, p. 503 - 508.

Vas[32] P. Vas
GENERALIZED ANALYSIS OF SATURATED AC MACHINES.
Archiv für Elektrotechnik, 1981, p. 57 - 62.

Vas[33] P. Vas, M. Alaküla, J.E. Brown, K.E. Hallenius
FIELD-ORIENTED CONTROL OF SATURATED A.C.-MACHINES
In: *IEE Conf. Rec., Power Electronics and variable Speed Drives*, London, 1988, p. 283 - 286.

Veltman[34] A. Veltman
THE FISH METHOD
-Interaction between AC-machines and switching power converters.
Ph.D. thesis, Delft University of Technology, 1994.

APPENDIX A

DESCRIPTION OF THE MULTI DSP-SYSTEM

The DSP-system consists of two digital signal processors connected parallel to each other. These processors are able to compute very fast. The processors are manufactured by Texas Instruments and offer even the opportunity to simulate in real-time. The advantage of a simulation in real-time above a normal software simulation is the opportunity to approach the reality: adapting parameters during simulation will give comparable results like in practice. Further, once we have to use the DSP-system in practice, the time spent with the DSP-system during the simulation pays itself back.

For a detailed hardware description we refer to Bosga[8], but for clearness we give an overview of the system:

- The DSP-system consists of two Texas Instruments TMS320C40 processors: 32 bit floating point, with a clock frequency of 40 MHz.

- 16 A/D and 16 D/A converters respectively provide 16 analog inputs and 16 analog outputs. The essential "anti-aliasing" filters are available: current and voltage are measured with a cut-off frequency of 5 kHz.

- A control panel has been connected to the analog inputs and allows to change parameters in real-time. The analog outputs are connected to oscilloscopes and voltmeters for monitoring and they are used as reference values for the hysteresis Current Regulated PWM-inverter. Digital multiplexing increases the control and monitoring possibilities.

- The signals of the resolver are converted into a digital number with the help of some programmable digital electronics. This number is digitally read in the DSP-system.

APPENDIX B

PARAMETERS USED DURING THE SIMULATION

B.1 Introduction to the pu-system.

Variable speed drives consist of several devices: control unit (DSP-system or analog electronics), monitoring equipment (e.g. oscilloscopes, voltmeters etc.), measurement equipment , power electronics and last but not least an electrical machine. These devices are characterized with limited output or input levels. Therefore a pu-system (per-unit) is often used in controlled drive systems. The actual value is divided by a reference value; this implies, that the variables become dimensionless and they are normally limited between -1 and +1 (in the case the reference values equal the rated values).

Four reference values have to be chosen and they determine the total pu-system:

$$[u_{ref}] = \sqrt{2}.[u_{sa}]_{rated,rms} \quad \textbf{(B.1)}$$

$$[i_{ref}] = \frac{3}{2}\sqrt{2}.[i_{sa}]_{rated,rms} \quad \textbf{(B.2)}$$

$$[\omega_{ref}] = [\omega_s]_{rated} \quad \textbf{(B.3)}$$

$$[\theta_{ref}] = 1 \text{ rad} \quad \textbf{(B.4)}$$

The factor 3/2 in equation B.2 takes care for power invariance: the power in the two-phase system has to equal that of the three-phase system. Appendix C presents the rated values of the used slip-ring induction machine.

The following equations are a result of the above introduced reference values:

$$[r_{ref}] = \frac{[u_{ref}]}{[i_{ref}]} \quad \textbf{(B.5)}$$

$$[t_{ref}] = \frac{[\theta_{ref}]}{[\omega_{ref}]} \quad \textbf{(B.6)}$$

$$[\psi_{ref}] = \frac{[u_{ref}]}{[\omega_{ref}]} \tag{B.7}$$

$$[\ell_{ref}] = \frac{[u_{ref}]}{[\omega_{ref}].[i_{ref}]} \tag{B.8}$$

$$[m_{ref}] = \frac{[u_{ref}].[i_{ref}]}{[\omega_{ref}]} \tag{B.9}$$

$$[\Theta_{ref}] = \frac{[u_{ref}].[i_{ref}]}{[\omega_{ref}]^3} \tag{B.10}$$

For more detailed information we refer to Blaschke[4].

B.2 The applied parameters during the simulation.

The parameters applied during the simulation are obtained from previous measurements. They were experimentally identified on the machine and the application of Field Oriented Control proved the correctness of the parameters. The saturation function of $S(\psi_\ell)$ has been obtained by a previous measurement with open rotor.

r_s	$= 2.74 \cdot 10^{-3}$	pu
r_k	$= 1.00 \cdot 10^{-2}$	pu
$\ell_{\sigma s}$	$= 1.31 \cdot 10^{-1}$	pu
$\ell_{\sigma k}$	$= 1.00 \cdot 10^{-1}$	pu
Θ	$= 2.79 \cdot 10^{3}$	pu
S_0	$= 2.75 \cdot 10^{-1}$	pu
$\psi_{\ell sat}$	$= 7.45 \cdot 10^{-1}$	pu

Table B.1a: The used parameters during the simulation in the sections 4.2 and 4.3.

ψ_ℓ (pu)	$\psi_\ell - \psi_{\ell sat}$ (pu)	$S_z(\psi_\ell)$ (x 10^{-3} pu)
0.745	0.000	0
0.89	0.145	5.7
0.98	0.235	41.2
1	0.255	54.8
1.018	0.273	68.8
1.063	0.318	101.1
1.109	0.364	175.7
1.145	0.400	248.8
1.16	0.415	293.8

Table B.1b: The used magnetisation curve in the simulation of the sections 4.2 and 4.3.

With the help of an interpolation program we approximate the $S_z(\psi_\ell)$ with:

$$S_z(\psi_\ell) = 0.4786*(\psi_\ell - \psi_{\ell sat})^2 + 3.6769*(\psi_\ell - \psi_{\ell sat})^4 + 19.689*(\psi_\ell - \psi_{\ell sat})^6 \tag{B.11}$$

APPENDIX C

DATA OF THE EXPERIMENTAL SETUP

C.1 The induction machine fed by a CR-PWM voltage source inverter.

The setup of the CR-PWM VSI-fed induction machine consists of a slip-ring induction machine, which is mechanically connected to a DC-machine. This DC-machine can be used as a positive or negative load. As mentioned in section 4.4 we only use the DC-machine as speed-control (except during the coarse identification); the induction machine itself is then controlled by the slip frequency, which is added to the frequency of the speed control. In this way we can easily pass the pull-out torque of the induction machine without any problem. The control of the induction machine consists of a multi DSP-system (see Appendix A). Further, the drive is equipped with the essential measuring and monitoring devices. The DC-link voltage of the inverter is provided by a so-called "*Ward-Leonard*[1]" circuit, which enables the inverter to absorb power during braking and generator operation. The electromechanical data of the slip-ring induction machine and the DC-machine are presented in table C.1.

Type number	ASEA MAC 20
Rated power	30 kW
Cosφ	0.93
Rated speed	2930 rpm
Voltage Y Current Y	380 V 55 A
Voltage Δ Current Δ	220 V 95 A

Table C.1a: The name-plate data of the induction machine.

Type number	SMIT Slikkerveer DC generator G 34/26
Rated power	27 kW
Rated speed	1500 rpm
Armature voltage	440 V
Field voltage Field current	220 V 3.2 A

Table C.1b: The name-plate data of the DC-machine.

[1]A "*Ward-Leonard*" circuit normally consists of an AC-machine directly connected to the mains, which is mechanically connected to a DC-generator. The DC-output voltage has a small ripple and can be controlled with the field current. This current is only used for magnetisation and thus we can control the DC-link voltage with a relatively small power. The DC-source is not only able to deliver energy, but also to absorb energy.

C.2 The reference values.

With the help of the name-plate data of table C.1 we are able to calculate the reference values in accordance with equations B.1 to B.4. Other references can easily be obtained with the help of equations B.5 to B.10.

$$[u_{ref}] = \sqrt{2}.220 = 311.1 \text{ V} \quad \textbf{(C.1)}$$

$$[i_{ref}] = \frac{3}{2}\sqrt{2}.55 = 116.7 \text{ A} \quad \textbf{(C.2)}$$

$$[\omega_{ref}] = 2\pi.50 = 314.2 \text{ rad/s} \quad \textbf{(C.3)}$$

$$[\theta_{ref}] = 1 \text{ rad} \quad \textbf{(C.4)}$$

APPENDIX D

MACHINE STRUCTURES USED IN SECTION 4.3

D.1 A short derivation of the machine structure of the synchronous machine affected with saturation.

We will start from the equations, presented in Blaschke[4] and chapter 2:

$$\mathbf{0} = r_k.\mathbf{i}_k^r + \dot{\boldsymbol{\psi}}_k^r \tag{D.1}$$

$$\boldsymbol{\psi}_k^{\psi} = \boldsymbol{\psi}_\ell^{\psi} + \ell_{\sigma k}.\mathbf{i}_k^{\psi} \tag{D.2}$$

$$\mathbf{i}_{\mu\ell}^{\psi} = S(\psi_\ell).\boldsymbol{\psi}_\ell^{\psi} \tag{D.3}$$

$$\mathbf{i}_{\mu\ell}^{\psi} = \mathbf{i}_s^{\psi} + \mathbf{i}_k^{\psi} + \mathbf{i}_r^{\psi} \tag{D.4}$$

$$m_{el} = [R(\pi/2).\boldsymbol{\psi}_l^{\psi}]^T.\mathbf{i}_s^{\psi} \tag{D.5}$$

$$\dot{\rho}^s = \tfrac{1}{\Theta}.\int (m_{el} - m_{load}).dt \tag{D.6}$$

$$\rho^s = \int \dot{\rho}^s.dt \tag{D.7}$$

First we have to transform stator and rotor current into their field oriented coordinates, which is shown in figures D.1a and D.1b, respectively.

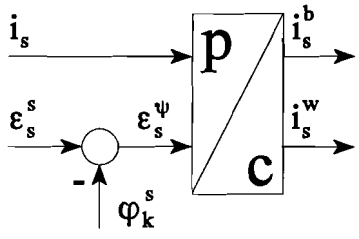

Figure D.1a: The transformation of the stator current into the field oriented coordinates.

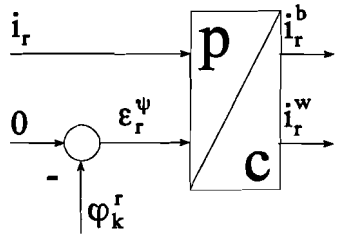

Figure D.1b: The transformation of the rotor current into the field oriented coordinates.

With the help of equation D.4 we can construct the air-gap magnetizing current (see figure D.2a)

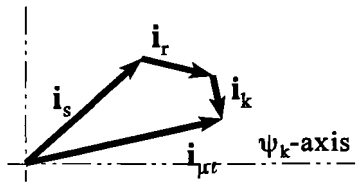

Figure D.2a: The construction of the air-gap magnetizing current.

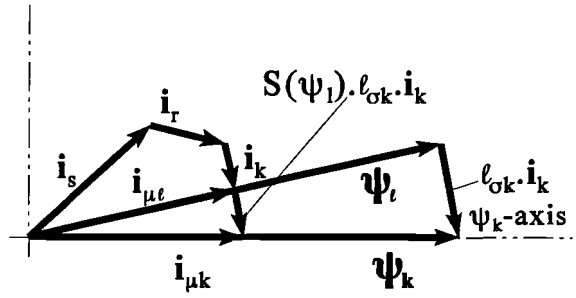

Figure D.2b: The introduction of the "fictitious" magnetizing current vector $\mathbf{i}_{\mu k}$.

Again we will introduce the "fictitious" current vector $\mathbf{i}_{\mu k}$:

$$\mathbf{i}_{\mu k} = S(\psi_\ell).\boldsymbol{\psi}_k \tag{D.8}$$

This vector is oriented parallel with the rotor flux vector. Equation D.2 shows the relation between the air-gap flux and the rotor flux and together with equation D.3 we can construct figure D.2b. This figure presents not only the relation between the fluxes, but also the relation of their related magnetizing currents. From this figure we can obtain the following equation:

$$\mathbf{i}_{\mu k}^{\psi} = \mathbf{i}_s^{\psi} + \mathbf{i}_r^{\psi} + (1 + S(\psi_\ell).\ell_{\sigma k}).\mathbf{i}_k^{\psi} \tag{D.9}$$

This equation can be rewritten into two coordinate equations:

$$\begin{aligned} i_{\mu k} &= i_s^b + i_r^b + (1 + S(\psi_\ell).\ell_{\sigma k}).i_k^b \\ 0 &= i_s^w + i_r^w + (1 + S(\psi_\ell).\ell_{\sigma k}).i_k^w \end{aligned} \tag{D.10}$$

Further we need to transform equation D.1 into the field oriented reference frame:

$$\mathbf{0} = r_k.\mathbf{i}_k^{\psi} + \dot{\boldsymbol{\psi}}_k^{\psi} + \dot{\varphi}_k^r.R(\pi/2).\boldsymbol{\psi}_k^{\psi} \tag{D.11}$$

With the help of equations D.8, D.9 and D.11 we can make a substructure, which is presented in figure D.3.

The construction of the air-gap flux remains unaltered. However, we have to examine the origin of the electromagnetic torque m_{el}. Equation D.5 describes the origin of this torque:

$$m_{el} = [R(\pi/2).\boldsymbol{\psi}_\ell^{\psi}]^T.\mathbf{i}_s^{\psi} \tag{D.12}$$

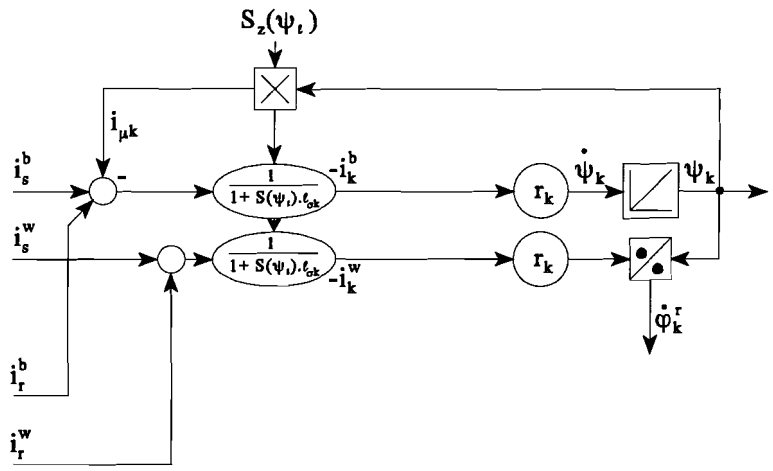

Figure D.3: The origin of the rotor flux from stator and rotor current.

When we substitute equation D.2, we get:

$$m_{el} = [R(\pi/2).(\boldsymbol{\psi}_k^{\psi} - \ell_{\sigma k}.\mathbf{i}_k^{\psi}]^T.\mathbf{i}_s^{\psi} \tag{D.13}$$

and with the help of the coordinates of the used vectors:

$$\boldsymbol{\psi}_k^{\psi} = \begin{bmatrix} \psi_k \\ 0 \end{bmatrix} \tag{D.14}$$

$$\mathbf{i}_s^{\psi} = \begin{bmatrix} i_s^b \\ i_s^w \end{bmatrix} \tag{D.15}$$

$$\mathbf{i}_k^{\psi} = \begin{bmatrix} i_k^b \\ i_k^w \end{bmatrix} \tag{D.16}$$

We finally get:

$$m_{el} = \psi_k.i_s^w - \ell_{\sigma k}.(i_k^b.i_s^w - i_k^w.i_s^b) \tag{D.17}$$

With the help of the derived equations, we are able to construct the machine structure of the synchronous machine affected with saturation, which is presented in figure 4.8.

D.2 The derivation of the stator voltage calculator.

During the identification of the inductances we need the assistance of the U/I-model. The U/I-model calculates the stator flux from voltage and current. In a real machine the stator voltage is available, however in the machine structure (see figure 2.16) of the current-fed induction machine this is not the case. Therefore we have to calculate the stator voltage from quantities, which are available in the machine structure.

We start with the stator equation:

$$\mathbf{u}_s^s = r_s.\mathbf{i}_s^s + \dot{\boldsymbol{\psi}}_s^s \tag{D.18}$$

Next we have to construct the stator flux:

$$\boldsymbol{\psi}_s^s = \boldsymbol{\psi}_k^s + \ell_{\sigma s}.\mathbf{i}_s^s - \ell_{\sigma k}.\mathbf{i}_k^s \tag{D.19}$$

Substitution gives:

$$\mathbf{u}_s^s = r_s.\mathbf{i}_s^s + \ell_{\sigma s}.\dot{\mathbf{i}}_s^s - \ell_{\sigma k}.\dot{\mathbf{i}}_k^s + \dot{\boldsymbol{\psi}}_k^s \tag{D.20}$$

Transformation of the derivative terms to the rotor flux coordinate system yields:

$$\dot{\boldsymbol{\psi}}_k^s = R(\varphi_k^s).R(\pi/2).\dot{\varphi}_k^s.\boldsymbol{\psi}_k^\psi + R(\varphi_k^s).\dot{\boldsymbol{\psi}}_k^\psi \tag{D.21}$$

$$\dot{\mathbf{i}}_k^s = R(\varphi_k^s).R(\pi/2).\dot{\varphi}_k^s.\mathbf{i}_k^\psi + R(\varphi_k^s).\dot{\mathbf{i}}_k^\psi \tag{D.22}$$

$$\dot{\mathbf{i}}_s^s = R(\varphi_k^s).R(\pi/2).\dot{\varphi}_k^s.\mathbf{i}_s^\psi + R(\varphi_k^s).\dot{\mathbf{i}}_s^\psi \tag{D.23}$$

Finally, we are able to write the stator voltage in quantities, which are directly available in the machine structure:

$$\mathbf{u}_s^\psi = r_s.\mathbf{i}_s^\psi + \ell_{\sigma s}.(R(\pi/2).\dot{\varphi}_k^s.\mathbf{i}_s^\psi + \dot{\mathbf{i}}_s^\psi) - \ell_{\sigma k}.(R(\pi/2).\dot{\varphi}_k^s.\mathbf{i}_k^\psi + \dot{\mathbf{i}}_k^\psi) + R(\pi/2).\dot{\varphi}_k^s.\boldsymbol{\psi}_k^\psi + \dot{\boldsymbol{\psi}}_k^\psi \tag{D.24}$$

Next we have to transform the stator voltage to the coordinate system associated with the stator-axis:

$$\mathbf{u}_s^s = R(\varphi_k^s).\mathbf{u}_s^\psi \tag{D.25}$$

APPENDIX E

CALCULATIONS OF THE IDENTIFICATION TECHNIQUES

E.1 Calculations of the identification techniques in section 4.3.2 (simulation).

As mentioned in section 4.3.2 we start with an estimation of an error in the real rotor angle of:

$$\hat{\chi}^{c}_{0} = 2.1 \qquad \textbf{(E.1)}$$

The experimental results after perpendicularity between the rotor current and the rotor flux in motor and generator operation (indicated with index m and index g, respectively) yield:

$$\begin{aligned} \hat{K}_{m1} &= 0.7613 \\ \hat{K}_{g1} &= 0.9392 \\ \hat{m}_{1} &= 0.7659 \end{aligned} \qquad \textbf{(E.2)}$$

With the help of equation 3.74 we are able to approximate the error in our first estimation:

$$\hat{\delta}_{1} = 0.09609 \qquad \textbf{(E.3)}$$

and this will result in a new corrected error in the real rotor angle:

$$\hat{\chi}^{c}_{1} = 2.00391 \qquad \textbf{(E.4)}$$

The subsequent experimental results after perpendicularity in motor and generator operation bring:

$$\begin{aligned} \hat{K}_{m2} &= 0.8529 \\ \hat{K}_{g2} &= 0.8625 \\ \hat{m}_{2} &= 0.6940 \end{aligned} \qquad \textbf{(E.5)}$$

With the help of equation 3.74 we are able to approximate the error in our first estimation:

$$\hat{\delta}_{2} = 0.0039095 \qquad \textbf{(E.6)}$$

and this will result in a new corrected error in the real rotor angle:

$$\hat{\chi}^{c}_{2} = 2.000002045 \qquad \textbf{(E.7)}$$

We notice that we find a good identification after two iterations.

E.2 Calculations of the identification techniques in section 4.3.3 (simulation).

First we execute an identification in the linear region and after ensuring perpendicularity we get:

$$\begin{aligned} \hat{i}^{b}_{s,lin} &= 0.1438 \\ \hat{i}^{w}_{s,lin} &= 0.1392 \\ \hat{\psi}^{b}_{s,lin} &= 0.5399 \\ \hat{\psi}^{w}_{s,lin} &= 0.0316 \\ \hat{K}_{,lin} &= 0.8560 \end{aligned} \qquad \textbf{(E.8)}$$

and with the help of the formulae 3.94 to 3.99 we finally get:

$$\begin{aligned} \ell_{\sigma s,lin} &= 0.1309 \\ \ell_{\sigma k,lin} &= 0.0986 \\ S_{,lin} &= 0.2760 \\ \psi_{\ell,lin} &= 0.5212 \end{aligned} \qquad \textbf{(E.9)}$$

Next we execute an identification in the saturated region:

$$\begin{aligned} \hat{i}^{b}_{s,sat} &= 0.4260 \\ \hat{i}^{w}_{s,sat} &= 0.2894 \\ \hat{\psi}^{b}_{s,sat} &= 1.1304 \\ \hat{\psi}^{w}_{s,sat} &= 0.0655 \\ \hat{K}_{,sat} &= 0.8560 \end{aligned} \qquad \textbf{(E.10)}$$

and again with the help of the formulae 3.94 to 3.99 we finally get:

$$\begin{aligned} \ell_{\sigma s,sat} &= 0.1310 \\ \ell_{\sigma k,sat} &= 0.0989 \\ S_{,sat} &= 0.3965 \\ \psi_{\ell,sat} &= 1.0750 \end{aligned} \qquad \textbf{(E.11)}$$

E.3 Calculations of the identification techniques in section 4.4.1 (practice).

The measurements of the K-identification are presented in table E.1. An overview of this identification method is shown in figure 3.11.

i_s (pu)	$\overset{o}{\psi}_{r1}$ (pu)	$\overset{o}{i}_k$ (pu)	K
0.113	0.458	0.154	0.733
0.129	0.504	0.179	0.720
0.144	0.557	0.192	0.750
0.16	0.589	0.215	0.744
0.176	0.615	0.240	0.733
0.192	0.639	0.262	0.733
0.207	0.66	0.284	0.729
0.223	0.679	0.307	0.727
0.239	0.696	0.329	0.727
0.254	0.711	0.349	0.727
0.27	0.725	0.371	0.727
0.286	0.738	0.393	0.728
0.302	0.751	0.414	0.729
0.317	0.762	0.433	0.732
0.333	0.772	0.454	0.733
0.349	0.782	0.476	0.733
0.365	0.792	0.498	0.733
0.38	0.801	0.518	0.734
0.396	0.809	0.539	0.735
0.412	0.817	0.561	0.735
0.428	0.825	0.582	0.735
0.443	0.832	0.603	0.735
0.459	0.839	0.624	0.735

Table E.1: The measurements of the K-identification from linearity to saturation.

E.4 Calculations of the identification techniques in section 4.4.2 (practice).

As mentioned in section 4.4.2 we start with an estimation of an error in the real rotor angle of:

$$\hat{\chi}_0^c = 3.7215 \quad \textbf{(E.12)}$$

The experimental results after perpendicularity between the rotor current and the rotor flux in motor and generator operation (indicated with index m and index g, respectively) yield:

$$\begin{aligned} \hat{K}_{m1} &= 0.8114 \\ \hat{K}_{g1} &= 0.8836 \\ \hat{m}_1 &= 0.9413 \end{aligned} \quad \textbf{(E.13)}$$

With the help of equation 3.74 we are able to approximate the error in our first estimation:

$$\hat{\delta}_1 = 0.04364408938 \quad \textbf{(E.14)}$$

and this will result in a new corrected error in the real rotor angle:

$$\hat{\chi}_1^c = 3.677855911 \quad \textbf{(E.15)}$$

The subsequent experimental results after perpendicularity in motor and generator operation give:

$$\begin{aligned} \hat{K}_{m2} &= 0.8551 \\ \hat{K}_{g2} &= 0.8531 \\ \hat{m}_2 &= 0.9143 \end{aligned} \quad \textbf{(E.16)}$$

With the help of equation 3.74 we are able to approximate the error in our first estimation:

$$\hat{\delta}_2 = 0.00110012913 \quad \textbf{(E.17)}$$

and this will result in a new corrected error in the real rotor angle:

$$\hat{\chi}_2^c = 3.676755782 \quad \textbf{(E.18)}$$

The next step gives:

$$\left.\begin{aligned} \hat{K}_{m3} &= 0.8574 \\ \hat{K}_{g3} &= 0.8528 \\ \hat{m}_3 &= 0.8966 \end{aligned}\right\} \delta_3 = -0.00239498693 \rightarrow \chi_3 = 3.679150769 \quad \textbf{(E.19)}$$

and the final step:

$$\left.\begin{aligned} \hat{K}_{m4} &= 0.8551 \\ \hat{K}_{g4} &= 0.8550 \\ \hat{m}_4 &= 0.8772 \end{aligned}\right\} \delta_4 = -0.00005010608 \rightarrow \chi_4 = 3.679200875 \quad \textbf{(E.20)}$$

E.5 Calculations of the identification techniques in section 4.4.3 (practice).

As mentioned during section 4.4.3 we can directly measure the magnetizing function when the winding ratio factor is available. This factor is already identified in section 4.4.1, so now we are able to measure this function. The measurements are presented in table E.2.

$\overset{\circ}{i}_k$ (A)	$i_{\mu\ell}$ (pu)	ψ_ℓ (pu)	$S(\psi_\ell)$ (pu)
2.5087	0.0237	0.1350	0.1756
5.1126	0.0483	0.2846	0.1697
10.0240	0.0947	0.5426	0.1745
12.2998	0.1162	0.6448	0.1802
14.9143	0.1409	0.7414	0.1900
16.8408	0.1591	0.8002	0.1988
19.2648	0.1820	0.8579	0.2121
21.5405	0.2035	0.9003	0.2260
24.0810	0.2275	0.9396	0.2421
26.4308	0.2497	0.9703	0.2573
29.3417	0.2772	1.0013	0.2768
31.1200	0.2940	1.0193	0.2884
33.5651	0.3171	1.0404	0.3048
36.0420	0.3405	1.0600	0.3212
38.9529	0.3680	1.0816	0.3402
40.5830	0.3834	1.0938	0.3505
43.5680	0.4116	1.1126	0.3699
45.4521	0.4294	1.1242	0.3820
47.6962	0.4506	1.1371	0.3963
50.9669	0.4815	1.1540	0.4172
53.1157	0.5018	1.1646	0.4309
58.4717	0.5524	1.1897	0.4643
62.4305	0.5898	1.2053	0.4893
67.9453	0.6419	1.2251	0.5240
72.6133	0.6860	1.2406	0.5530
77.0802	0.7282	1.2540	0.5807
82.6268	0.7806	1.2694	0.6149
86.2469	0.8148	1.2794	0.6369

Table E.2: The measurements of the magnetizing function.

APPENDIX F

NECESSARY TRANSFORMATIONS IN PRACTICE.

F.1 Transformations between the different systems.

Our theory is based on the two-phase system, while the slip-ring induction machine uses three phases. Therefore, we need to transform the output and input signals. The transformation from the two-phase system to the three phase system (see Blaschke[2] for the derivation):

$$\begin{bmatrix} i_{sa} \\ i_{sb} \\ i_{sc} \end{bmatrix} = \begin{bmatrix} \frac{2}{3} & 0 \\ -\frac{1}{3} & \frac{1}{\sqrt{3}} \\ -\frac{1}{3} & -\frac{1}{\sqrt{3}} \end{bmatrix} \cdot \begin{bmatrix} i_s^{s1} \\ i_s^{s2} \end{bmatrix} \tag{F.1}$$

When measuring we will need the following transformations:

$$\begin{bmatrix} i_s^{s1} \\ i_s^{s2} \end{bmatrix} = \begin{bmatrix} 1 & -\frac{1}{2} & -\frac{1}{2} \\ 0 & \sqrt{\frac{3}{2}} & -\sqrt{\frac{3}{2}} \end{bmatrix} \cdot \begin{bmatrix} i_{sa} \\ i_{sb} \\ i_{sc} \end{bmatrix} \tag{F.2}$$

for the transformation of the current and

$$\begin{bmatrix} u_s^{s1} \\ u_s^{s2} \end{bmatrix} = \begin{bmatrix} \frac{2}{3} & -\frac{1}{3} & -\frac{1}{3} \\ 0 & \frac{1}{\sqrt{3}} & -\frac{1}{\sqrt{3}} \end{bmatrix} \cdot \begin{bmatrix} u_{sa} \\ u_{sb} \\ u_{sc} \end{bmatrix} \tag{F.3}$$

for the transformation of the voltage.

F.2 Transformations between the line and phase voltages.

As explained in section 4.4.1 we will need the transformation between the line and phase voltages:

$$\begin{bmatrix} u_{sa} \\ u_{sb} \end{bmatrix} = \begin{bmatrix} \frac{2}{3} & -\frac{1}{3} \\ -\frac{1}{3} & \frac{2}{3} \end{bmatrix} \cdot \begin{bmatrix} u_{sac} \\ u_{sbc} \end{bmatrix} \tag{F.4}$$